Performance of Carbon Nanotubes as Supports of Nickel-Iron
Catalysts for Carbon Dioxide Methanation

Miss Phanatchakorn Mala

จุฬาลงกรณ์มหาวิทยาลัย
CHULALONGKORN UNIVERSITY

A Thesis Submitted in Partial Fulfillment of the Requirements
for the Degree of Master of Engineering in Chemical Engineering
Department of Chemical Engineering
FACULTY OF ENGINEERING
Chulalongkorn University
Academic Year 2020

สมรรถนะของท่อนาโนคาร์บอนสำหรับเป็นตัวรองรับตัวเร่งปฏิกิริยานิกเกิล-เหล็กสำหรับปฏิกิริยามีเทนเนชันของคาร์บอนไดออกไซด์

น.ส.พนัชกร มาละ

Thesis Title	Performance of Carbon Nanotubes as Supports of Nickel-Iron Catalysts for Carbon Dioxide Methanation
By	Miss Phanatchakorn Mala
Field of Study	Chemical Engineering
Thesis Advisor	Associate Professor TAWATCHAI CHARINPANITKUL, D.Eng.
Thesis Co Advisor	Sakhon Ratchahat, D.Eng.

Accepted by the FACULTY OF ENGINEERING, Chulalongkorn University in Partial Fulfillment of the Requirement for the Master of Engineering

.... Dean of the FACULTY OF ENGINEERING

(Professor SUPOT TEACHAVORASINSKUN, D.Eng.)

THESIS COMMITTEE

.... Chairman

(VARUN TAEPAISITPHONGSE, Ph.D.)

.... Thesis Advisor

(Associate Professor TAWATCHAI CHARINPANITKUL, D.Eng.)

.... Thesis Co-Advisor

(Sakhon Ratchahat, D.Eng.)

.... Examiner

(Professor PAISAN KITTISUPAKORN, Ph.D.)

.... External Examiner

(Associate Professor Thongthai Witoon, Ph.D.)

พนัชกร มาละ : สมรรถนะของท่อนาโนคาร์บอนสำหรับเป็นตัวรองรับตัวเร่งปฏิกิริยา นิกเกิล-เหล็กสำหรับปฏิกิริยามีเทนเนชันของคาร์บอนไดออกไซด์. (Performance of Carbon Nanotubes as Supports of Nickel-Iron Catalysts for Carbon Dioxide Methanation) อ.ที่ปรึกษาหลัก : รศ. ดร.ธวัชชัย ชรินพาณิชกุล, อ.ที่ปรึกษาร่วม : ดร.สาคร ราชหาด

ในปัจจุบันปัญหาภาวะโลกร้อนมีสาเหตุมาจากการเพิ่มขึ้นของปริมาณแก๊สคาร์บอนไดออกไซด์ในชั้นบรรยากาศ ดังนั้นจึงได้มีงานวิจัยมากมายพยายามที่จะลดปริมาณของแก๊สคาร์บอนไดออกไซด์ โดยการพัฒนาตัวเร่งปฏิกิริยาที่สามารถ เปลี่ยนแก๊สคาร์บอนไดออกไซด์ไปเป็นแก๊สมีเทนได้อย่างมีประสิทธิภาพ งานวิจัยนี้จึงได้ศึกษาประสิทธิภาพของตัวเร่งปฏิกิริยา นิกเกิลและเหล็ก เนื่องจากตัวเร่งปฏิกิริยานิกเกิลซึ่งแต่เดิมนิยมใช้ในปฏิกิริยานี้ มีค่าความสามารถในการเกิดปฏิกิริยาไม่สูงมาก นัก และยังเสื่อมสภาพได้ง่าย นอกจากนั้นท่อนาโนคาร์บอนเป็นหนึ่งในวัสดุระดับนาโนที่มีคุณสมบัติที่น่าสนใจหลากหลาย ประการ เช่น มีคุณสมบัติการนำไฟฟ้า คุณสมบัติทางกล และคุณสมบัติการนำความร้อนที่ดี ในงานวิจัยนี้ใช้น้ำมันยูคาลิปตัส เป็นสารตั้งต้นในการผลิตท่อนาโนคาร์บอน โดยท่อนาโนคาร์บอนถูกสังเคราะห์ผ่านวิธีการไพโรไรซิสร่วมของน้ำมันยูคาลิปตัส และตัวเร่งปฏิกิริยาเฟอร์โรซีน จากการทดลองพบว่าท่อนาโนคาร์บอนที่ได้จากการสังเคราะห์ที่อุณหภูมิ 900 °C และ อัตราส่วนโดยโมลของน้ำมันยูคาลิปตัสต่อเฟอร์โรซีน 3:1 เป็นท่อนาโนคาร์บอนที่มีคุณภาพและสเถียรภาพทางความร้อนสูง ที่สุด จากนั้นท่อนาโนคาร์บอนที่ถูกสังเคราะห์ขึ้นจากสภาวะดังกล่าว จะถูกนำไปใช้เป็นตัวรองรับของตัวเร่งปฏิกิริยานิกเกิลและ เหล็ก เพื่อใช้ในปฏิกิริยามีเทนเนชันของคาร์บอนไดออกไซด์ ที่อุณหภูมิ 325 องศาเซลเซียส อัตราส่วนระหว่าง CO_2: H_2: He อยู่ที่ 1:4:5 โดยโมล จากการทดลองทำให้ทราบว่า ที่อัตราส่วนโดยน้ำหนักของนิกเกิลกับเหล็กที่ 70:30 จะให้ร้อยละ การเปลี่ยนของแก๊สคาร์บอนไดออกไซด์สูงที่สุด เนื่องมาจากตัวเร่งปฏิกิริยาที่สภาวะดังกล่าวมีความสามารถในการรีดิวซ์สูงซึ่ง เป็นผลมาจากการเติมเหล็กลงไปบนตัวเร่งปฏิกิริยาในปริมาณที่เหมาะสม

สาขาวิชา	วิศวกรรมเคมี	ลายมือชื่อนิสิต	....
ปีการศึกษา	2563	ลายมือชื่อ อ.ที่ปรึกษาหลัก	....
		ลายมือชื่อ อ.ที่ปรึกษาร่วม	....

6270171521 : MAJOR CHEMICAL ENGINEERING

KEYWOR
D:
Carbon nanotube, Eucalyptus oil, CO2 methanation, Nickel-Iron catalyst

Phanatchakorn Mala : Performance of Carbon Nanotubes as Supports of Nickel-Iron Catalysts for Carbon Dioxide Methanation. Advisor: Assoc. Prof. TAWATCHAI CHARINPANITKUL, D.Eng. Co-advisor: Sakhon Ratchahat, D.Eng.

Nowadays, an increase in CO_2 emission is one of the main reasons of global warming. Many studies have tried to solve the problem by developing catalysts to efficiently convert CO_2 into CH_4. Herein, bimetallic Ni-Fe catalyst was studied to improve the catalyst activity of Ni-based catalyst which has low activity and is easily deactivated. Carbon nanotubes (CNTs) have been identified as one of the most promising nanomaterials with unique electrical, thermal, and mechanical properties. In this thesis, CNTs was synthesized from eucalyptus oil as a renewable carbon source and then employed as catalyst support material in methanation. Variations of synthesis conditions indicated the optimal pyrolysis temperature (T_{pyro}) of 900 °C and molar ratio of eucalyptus oil and ferrocene ($m_{oil/fer}$) of 3:1 to obtain highest content of CNTs and highest thermal stability. The synthesized CNTs were impregnated with nickel and iron with different weight ratios to be catalyst for CO_2 methanation. The 30wt% Ni-Fe/CNT with weight ratio Ni:Fe of 70:30 could provide the highest CO_2 conversion and methane yield at reaction temperature of 325 °C and molar ratio CO_2:H_2:He of 1:4:5 due to its highest reducibility and synergistic effect of Ni and inherited Fe presence in synthesized CNTs.

จุฬาลงกรณ์มหาวิทยาลัย

CHULALONGKORN UNIVERSITY

Field of Study:	Chemical Engineering	Student's Signature	
		....	
Academic Year:	2020	Advisor's Signature	
		....	
		Co-advisor's Signature	
		....	

ACKNOWLEDGEMENTS

TABLE OF CONTENTS

Page

จุฬาลงกรณ์มหาวิทยาลัย

CHULALONGKORN UNIVERSITY

LIST OF TABLES

Page

จุฬาลงกรณ์มหาวิทยาลัย

CHULALONGKORN UNIVERSITY

LIST OF FIGURES

Page

จุฬาลงกรณ์มหาวิทยาลัย

CHULALONGKORN UNIVERSITY

CHAPTER 1

INTRODUCTION

1.1 Background and motivation

Nowadays, global warming is one of the serious problems caused by human activities and fossil fuel burning [1]. One of the major causes of global warming is an increase in one of the greenhouse gases or carbon dioxide (CO_2) in the atmosphere. From various technical methods to reduce the concentration of CO_2, the conversion of CO_2 into methane (CH_4), also known as CO_2 methanation, is a promising application because it is not only reducing the concentration of CO_2 but also producing CH_4 which is a high energy resource [2].

Generally, CO_2 methanation is the highly exothermic reaction conducted in a fixed-bed reactor [3]. This type of reactor still has some problems remaining such as the hotspot formation on the catalyst which can lead to catalyst deactivation resulting in the decline in CO_2 conversion [4]. Therefore, catalyst selection, especially in the use of material with high thermal conductivity and high thermal stability, is also important to achieve high catalyst performance for exothermic reaction [5].

Typically, a catalyst for CO_2 methanation is a metal on support materials [6]. The most popular active metal is nickel (Ni) due to its high selectivity and low cost. However, Ni-based catalyst does not provide high catalyst activity [7]. To increase the performance of catalyst, the catalyst is doped with another metal with higher catalyst activity such as iron (Fe) in the expectation of the synergistic effect [8, 9]. For the support material, carbon nanotubes (CNTs) are interesting due to their high thermal conductivity and high thermal stability [10] which may help decrease the hotspot formation. Moreover, the tubular structure of CNTs could also enhance the dispersion of active metals on their surface [11].

CNTs can be synthesized from various petroleum-based carbon sources such as alcohols [12] or hydrocarbons [13] which may lead to depletion of natural resources. Therefore, eucalyptus oil, a renewable carbon source obtaining from leaves of

eucalyptus trees, becomes an attractive feedstock for the synthesis of CNTs. This natural oil or bio-based material can probably promote the bioeconomy related to the use of biorenewable resources to meet the United Nations' Sustainable Development Goals (SDGs). Moreover, the high oxygen content in eucalyptus oil could help improve the quality of CNTs due to the oxidation of amorphous carbon [14]. However, the studies in the use of eucalyptus oil for the synthesis of CNTs as a support catalyst in CO_2 methanation have not been reported. CNTs can be prepared via various techniques such as chemical vapor deposition (CVD), laser ablation, and arc discharge [15]. In this study CVD or co-pyrolysis with a metal catalyst was selected because it could provide well-aligned CNTs and low investment cost.

This research aimed to use eucalyptus oil as a carbon precursor for the synthesis of CNTs as a catalyst support for CO_2 methanation. CNTs were synthesized by co-pyrolysis with ferrocene. Then, Ni and Fe would be impregnated on CNTs by impregnation method using ethanol as solvent. Finally, bimetallic Ni-Fe/CNT catalyst would be examined under the controlled conditions to reach high CO_2 conversion and high CH_4 selectivity.

CNT support and Ni-Fe/CNT catalyst would be characterized by various techniques, for example, Field-emission scanning electron microscopy (FESEM), Thermogravimetric analysis (TGA), Raman spectroscopy, N_2 adsorption/desorption analysis, X-ray diffraction (XRD), and Temperature-programmed reduction in H_2 (H_2-TPR). The performance of Ni-Fe/CNT catalyst would be analyzed from CO_2 conversion, CH_4 selectivity, and CH_4 yield.

1.2 Research objectives

This research aimed to synthesize CNTs by co-pyrolysis of eucalyptus oil and ferrocene and to apply CNTs as support material for nickel-iron catalyst in CO_2 methanation. Performances of Ni-Fe/CNT catalysts prepared under different conditions were investigated.

1.3 Scope of this research work

The scope of this research was to synthesize CNTs from eucalyptus oil and use it as supports of Ni-Fe catalysts for CO_2 methanation. This thesis consisted of 3 parts, which were the synthesis of CNTs by co-pyrolysis with ferrocene, catalyst preparation by impregnation of bimetallic Ni and Fe, and performance test for CO_2 methanation with details as followed.

1.3.1   Synthesis of CNTs by co-pyrolysis with ferrocene

CNTs would be synthesized from eucalyptus oil at various temperature (800, 850 and 900 ℃) and molar ratio of eucalyptus oil to ferrocene (1:1, 2:1, and 3:1) under nitrogen atmosphere. The characterization of CNTs would use FESEM to observe the morphology of CNTs, TGA to observe the thermal stability, N_2 adsorption/desorption to observe the surface area, and Raman spectroscopy to observe the crystallinity of CNTs.

1.3.2   Impregnation of bimetallic Ni-Fe onto CNT support

Ni and Fe would be impregnated on CNTs with 30wt% of total metal loading at various Ni to Fe weight ratio (0:1, 1:3, 1:1, 3:1, and 1:0). The characterization of Ni-Fe/CNT would use XRD to observe the crystallinity and H_2-TPR to observe the reducibility.

1.3.3   Performance of bimetallic Ni-Fe/CNTs catalyst in CO_2 methanation

The methanation reaction would be conducted to test the activity of the bimetallic Ni-Fe/CNT catalyst. The gas-phase products would be analyzed by gas chromatography techniques to calculate CO_2 conversion and CH_4 selectivity.

CHAPTER 2
LITERATURE REVIEW

To reduce the concentration of CO_2 in the atmosphere, methanation is one of the interesting routes to convert CO_2 into CH_4. Therefore, some basic knowledges of CO_2 methanation and heterogeneous catalyst were described in this chapter.

2.1 Carbon dioxide methanation

CO_2 methanation, CO_2 hydrogenation to CH_4, the reduction of CO_2 to CH_4, or Sabatier reaction are some of the names used to refer to the reaction to convert CO_2 into CH_4. The reactant is a syngas which is the combination of CO_2 and H_2. The products are synthetic natural gas or CH_4 and H_2O. This reaction is an exothermic reaction. The stoichiometry is shown in **Eq. 1** [16]. Each CO_2 molecule needs to require eight electrons to reduce itself into CH_4. Generally, catalysts are necessary in this reaction because they provide the active sites for CO_2 and H_2 to absorb and react with each other. Therefore, a good catalyst should promote the sufficient rate and selectivity to CH_4 formation [3].

$$CO_2(g) + 4H_2(g) \leftrightharpoons CH_4(g) + 2H_2O(g) \quad \Delta H_R^0 = -164 \text{ kJ (mol CH}_4)^{-1} \qquad \text{Equation 1}$$

In general, there are 2 categories of reaction pathways of CO_2 methanation indicated by dissociative and associative schemes [17]. For a dissociative scheme, the CO_2 dissociates to form carbonyl (CO) and oxygen atom. Then, CO is hydrogenated to finally form CH_4. Dissociative scheme could be referred to the mechanism of CO_2 with CO intermediate. On the other hand, in an associate scheme, CO_2 adsorbs associatively onto catalyst surface and reacts with adsorbed hydrogen to from CH_4. Associative scheme could be referred to the mechanism of CO_2 without CO intermediate.

Sang et al. [18] proposed the CO_2 methanation pathway with the presence of CO as an intermediate as shown in **Figure 1**. Step 1 to 4 represent C formation and step 5 to 6 represent C hydrogenation and H_2O formation, respectively. The reaction mechanism starts with the adsorption of CO_2 onto the surface of metal catalyst. Then,

CO_2 dissociates to CO and O on active sites. Next, CO dissociates to C atom and O atom which the dissociation of CO is the rate-determining step due to its highest activation energy [17]. Finally, H is adsorbed to form CH_4 gas as a product.

$$H_2 + 2^* \rightarrow 2H^*$$

$$CO_2 + ^* \rightarrow CO_2^*$$

$$CO_2^* + ^* \rightarrow CO^* + O^*$$

$$CO^* + ^* \rightarrow C^* + O^*$$

$$C^* \xrightarrow{+H^*} CH^* \xrightarrow{+H^*} CH_2^* \xrightarrow{+H^*} CH_3^* \xrightarrow{+H^*} CH_4 + ^*$$

$$O^* \xrightarrow{+H^*} OH^* \xrightarrow{+H^*} H_2O^* \rightarrow H_2O + ^*$$

* = active site
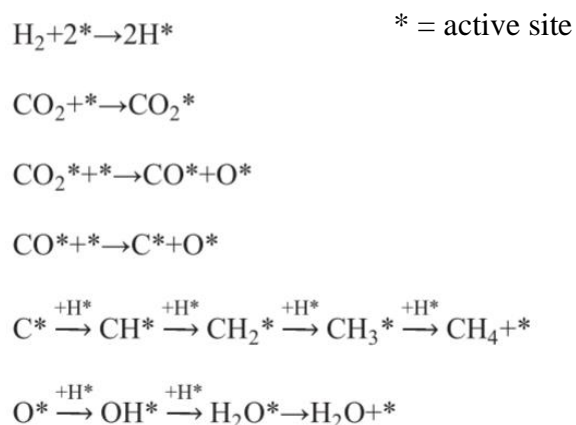
Figure 1 Mechanism of CO_2 methanation with CO intermediate [18]

On the contrary, Medsforth [19] proposed the mechanism of CO_2 methanation without CO intermediate. Thus, the intermediate in this reaction pathway is defined as $C(OH)_2$ which is shown in **Figure 2**. CO_2 reacts with H_2 to form $C(OH)_2$ on metal catalyst surface which is the rate-limiting step.

$$H_2 + 2^* \rightarrow 2H^*$$

$$CO_2 + ^* \rightarrow CO_2^*$$

$$CO_2^* + 2H^* \rightarrow C(OH)_2^* + 2^*$$

$$C(OH)_2^* + H^* \rightarrow CH_2O^* + OH^*$$

$$CH_2O^* + H^* \rightarrow CH_2^* + OH^*$$

$$CH_2^* \xrightarrow{+H^*} CH_3^* \xrightarrow{+H^*} CH_4 + ^*$$

$$OH^* + H^* \rightarrow H_2O^* \rightarrow H_2O + ^*$$

* = active site
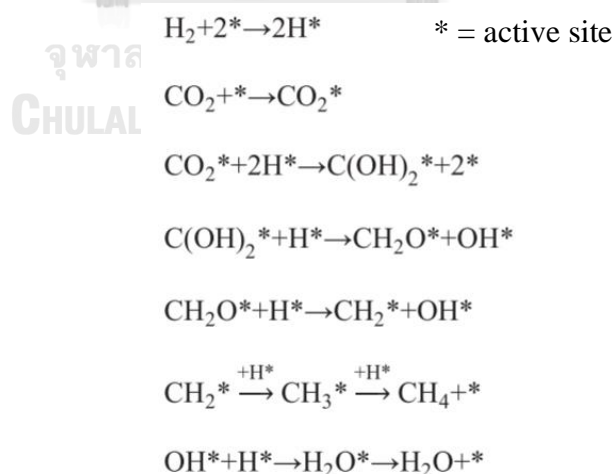
Figure 2 Mechanism of CO_2 methanation without CO intermediate [19]

In addition, Ren et al. [20] studied the mechanism of CO_2 methanation using Density-functional theory (DFT) calculation. The results revealed that the formation of CO as an intermediate was the optimal condition due to the lowest energy barrier.

Typically, the CO_2 methanation is conducted under atmospheric pressure and the operating temperature above 250 °C to enhance the kinetic rate. However, an increase in temperature greater than 500 °C results in the limitation of exothermic reaction [3, 21]. Equilibrium conversion of CO_2 methanation is shown in **Figure 3**. Due to the nature of highly exothermic reaction of CO_2 methanation, an increase in reaction temperature decreases CO_2 conversion [21].
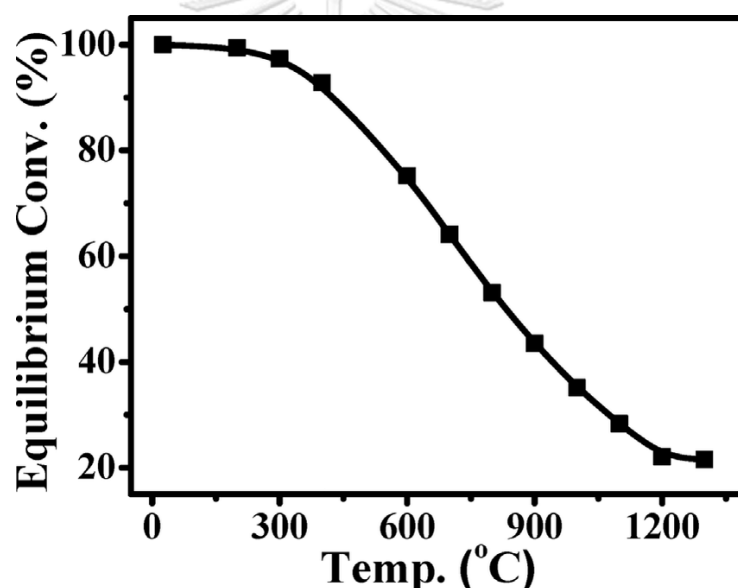
Figure 3 Equilibrium conversion in CO_2 methanation [21]

2.2 Heterogeneous catalysts in carbon dioxide methanation

Conversion of CO_2 is an exothermic reaction where CO_2 reacts with H_2 to form CH_4 and H_2O. Heterogeneous catalysts consisted of active metal and support material play an important role in a gas-phase methanation reaction [3].

.

2.2.1   Active metal

Active metal in CO_2 methanation is usually the transition metal as shown in **Figure 4**.

Figure 4 Active metal for CO_2 methanation (grey color) [3]

From Mills and Steffgen [8], the potential active metals for CO_2 methanation consist of Ruthenium (Ru), Iron (Fe), Nickel (Ni), Cobalt (Co), and Molybdenum (Mo) which the order of catalyst activity is Ru > Fe > Ni > Co > Mo and the order of CH_4 selectivity is Ni > Co > Fe > Ru > Mo. Ru provides a highest catalyst activity but low CH_4 selectivity. Fe provides high catalyst activity but low CH_4 selectivity. Ni provides the highest selectivity, moderate activity, and low cost. Co shows insignificant difference in catalyst activity with Ni, but the price is more expensive than Ni [3]. Finally, Mo has a lowest activity and selectivity. For this reason, Ni has been used widely in the lab-scale and commercial applications [4, 7, 22, 23]. Even though Ni has the potential to be the active metal from high selectivity and low cost, however, Ni-based catalysts still have some problems in the sintering or the agglomeration of Ni particle which makes the catalyst deactivate easily. Everson et al. [24] reported that the sintering of Ni particle on Aluminum oxide (Al_2O_3) support occurred at 723-973 K in CO_2 methanation. To improve the catalyst activity, a Ni-Fe system has been developed in many studies. Sehested et al. [25] found that the Ni-Fe alloy had provided higher CO_2 conversion when compared with pure Ni in CO and CO_2 methanation. The highest CO_2 conversion would be obtained when weight ratio of Ni to Fe was more than one [25].

2.2.2   Support material

Support material is one of the important factors that affect the activity and selectivity of the catalyst.   The popular support material is a metal oxide, i.e., alumina (Al_2O_3) [26], silica (SiO_2) [27], ceria (CeO_2) [28], and titania (TiO_2) [29]. Nevertheless, recent researches have studied the other support materials such as activated carbon (AC) [30] and CNTs [31].   CNTs are used in the CO_2 methanation due to its moderate surface area, high thermal conductivity, and high metal dispersion on CNTs [32].

2.3 Carbon nanotubes

CNTs are cylindrical molecules in a nanoscale coming from rolled-up of graphene sheets [33]. It can be divided into 2 types depending on their structure: single-walled carbon nanotube (SWCNT) and multi-walled carbon nanotube (MWCNT). SWCNT consists of a rolled-up graphene sheet. MWCNT consists of several rolled-up graphene sheets in the concentric cylindrical form [34].   Generally, SWCNT has an inner diameter between 0.617-3 nanometers. MWCNT has an inner diameter between 30-50 nm with the tube length of 10-100 micrometers [35, 36]. SWCNT and MWCNT structures were shown in **Figure 5** and CNT properties were shown in **Table 1**.
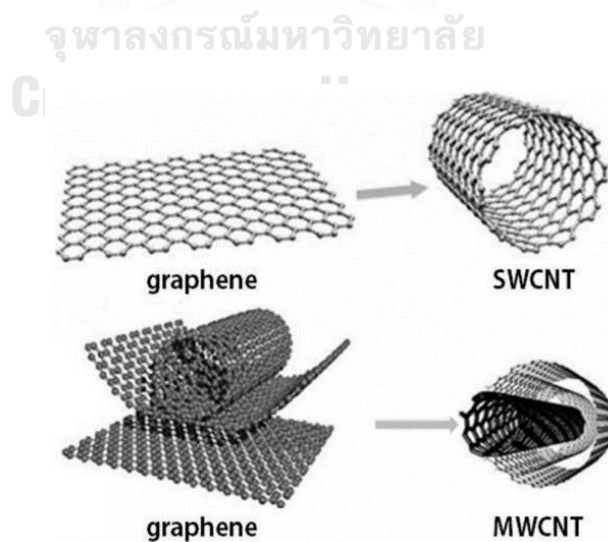
Figure 5 SWCNT and MWCNT structures [37]

Table 1 Properties of CNTs [10]

Properties	SWCNT	MWCNT
Specific Gravity	0.8	1.8
Elastic Modulus (TPa)	1	0.3 - 1
Strength (GPa)	50 - 500	10 - 60
Resistivity ($\mu\Omega$ cm)	5 - 50	5 - 50
Thermal conductivity ($Wm^{-1}K^{-1}$)	3000	3000
Thermal stability (°C in air)	>700	>700
Surface area (m^2/g)	400 - 900	200 - 400

2.3.1 Synthesis of carbon nanotubes via chemical vapor deposition

Chemical vapor deposition (CVD) is a popular method for large-scale production and controlling growth direction of CNTs [38] when compared with the other methods, i.e., arc discharge [39] and laser ablation [40]. A carrier gas (nitrogen, argon, or helium) flows into reactor at atmospheric pressure. Then, temperature of the reactor is raised from room temperature to designated reaction temperature (700 – 900 °C). A carbon source such as hydrocarbon, alcohol, or oil and a metallocene catalyst such as ferrocene ($C_{10}H_{10}Fe$) can be decomposed when temperature of the reactor is raised to the decomposition temperature allowing the reactant to diffuse and self-assemble into CNT structure inside the reactor [41]. Characterization of CNTs obtained via CVD technique reveals that the dominant product is MWCNT rather than SWCNT [42]. The schematic diagram of CVD reactor was shown in **Figure 6**.
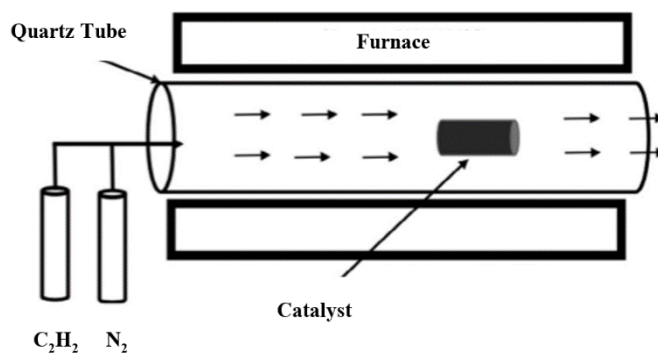
Figure 6 Schematic diagram of CVD reactor [42]

2.3.2 Mechanism of CNT growth

Vapor-solid-solid model (VSS) as shown in **Figure 7** is the widely accepted CNT growth model proposed by Persson et al. [43] which was adapted from the vapor-liquid-solid model (VLS) which was proposed by Wagner and Ellis [44]. This model can be explained in 4 steps. First step is the decomposition of carbon sources or hydrocarbon gas followed by the precipitation of decomposed gas onto catalyst surface. Next, hydrocarbon gases decompose into carbon atom on catalyst surface and diffuse into the catalyst. After that, CNTs are nucleated at the edge of catalyst with 2 main growth models: tip growth and base growth. For tip growth model, CNTs lifts the catalyst from the substrate due to the weak interaction between catalyst and substrate. Therefore, CNTs grow below the catalyst. On the other hand, base growth model represents the growth of CNTs above catalyst due to the strong interaction of catalyst and substrate. CNTs will stop growing if the metal catalysts have a gradual structural change [45].
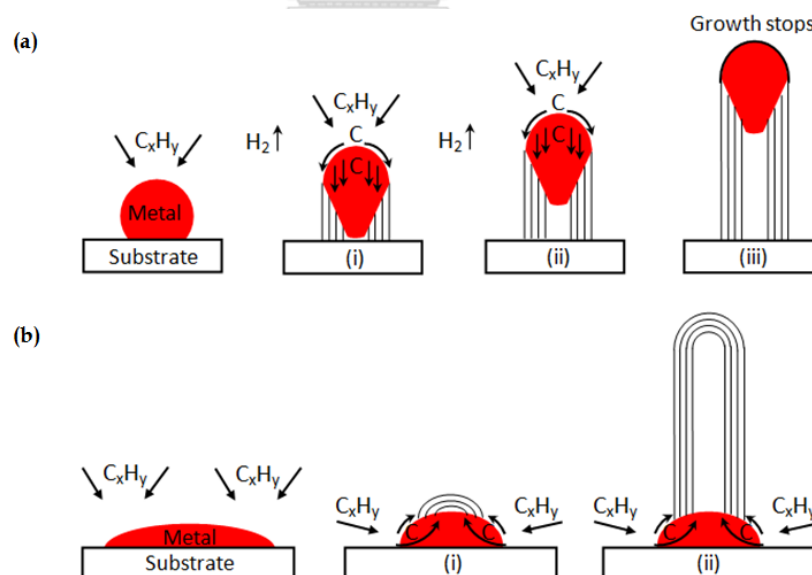
Figure 7 Growth mechanism of CNTs (a) tip growth (b) base growth [43]

2.4 Literature review

    2.4.1 Use of eucalyptus oil as carbon precursor

    CNTs could be synthesized by CVD method. Use of eucalyptus oil as a carbon precursor was reported by Ghosh et al. [14]. They synthesized CNTs by CVD method using a quart tube reactor with inner diameter of 2.5 cm and length of 50 cm. N_2 was used as a carrier gas with the flowrate of 100 standard cubic centimeters per minute (cm^3/min). Eucalyptus oil which consisted of eucalyptol ($C_{10}H_{18}O$) as a main component was used as a carbon precursor. Fe/Co impregnated on silica-zeolite support material was used as a catalyst. In their experiment, ceramic boat which was filled with 0.1 g catalyst was placed in the middle of the reactor. The reactor was heated to synthesis temperature of 850 °C. After the synthesis temperature was achieved, eucalyptus oil was fed into the quartz tube reactor with a flowrate of 0.1 cm^3/min. The synthesis time was kept at 25 min. The morphology of CNTs was observed by Transmission Electron Microscope (TEM) as shown in **Figure 8**. From observation, the carbon products had less amount of amorphous carbon because the presence of oxygen in eucalyptol molecules. Oxygen could help to oxidize amorphous carbon into CO_2 or CO. In their study, SWCNTs were obtained with outer diameter of 0.79 to 1.71 nm.
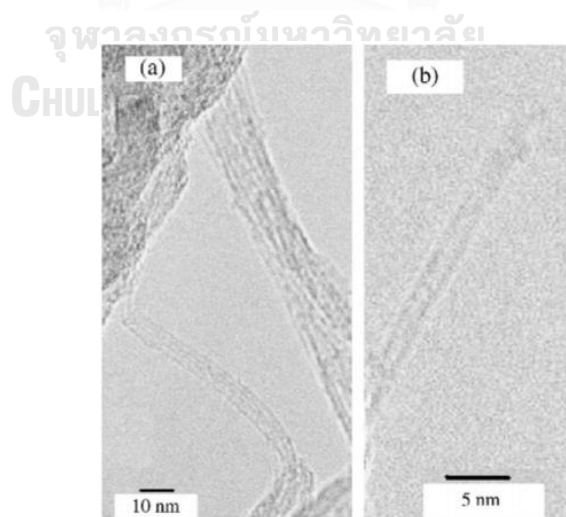
Figure 8 TEM images of CNTs synthesized from eucalyptus oil (a) SWCNT bundles (b) SWCNT [14]

The low amount of amorphous carbon in carbon product was confirmed by the result from Raman spectroscopy technique. Raman spectra from Raman spectroscope (JASCO, NRS-1500W) with green laser was shown in **Figure 9**. The peak at 1335 cm^{-1} was attributed to the vibration of non-sp^2 bonded carbon atom which was called D-band. Generally, D-band was applied to identify amorphous carbon. The peak at 1587 cm^{-1} was attributed to the vibration of sp^2 bonded carbon atom which was called G-band. Generally, G-band was applied to identify CNTs. Low intensity of D-peak could be attributed to the low amount of amorphous carbon while high intensity of G-peak obtained could be attributed to the presence of CNTs. The ratio of D-peak to G-peak (I_D/I_G) was 0.3 [14]. Generally, the intensity of D-band to G-band (I_D/I_G) was used to inform the crystallinity of carbon product. The higher crystallinity of carbon product was obtained at lower I_D/I_G.
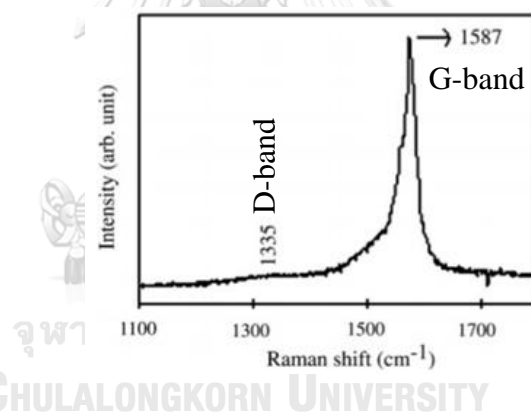
Figure 9 Raman spectra of CNTs synthesized from eucalyptus oil [14]

2.4.2 Effect of molar ratio of precursor to catalyst on properties of CNTs

Molar ratio of precursor to catalyst is one of the crucial parameters which affects the properties of CNTs. There were some studies on the effect of molar ratio of precursor to catalyst on properties of CNTs as followed.

Mongkolsamai et al. [41] synthesized CNTs by CVD method using a quart tube reactor with inner diameter of 4.2 cm and length of 60 cm. N$_2$ was used as a carrier gas with the flowrate of 2000 cm^3/min. Ethanol (C$_2$H$_5$OH) was used as a carbon precursor.

Ferrocene ($C_{10}H_{10}Fe$) was used as a catalyst. In their experiment, ceramic boat which was filled with ferrocene was placed in the middle of reactor. The reactor was heated to synthesis temperature of 900 °C. After the synthesis temperature was achieved, ethanol was sprayed from ultrasonic nebulizer with flowrate of 2000 cm^3/min into the quartz tube reactor. Molar ratio of ethanol to ferrocene was varied from 80:1 to 58:1 and 48:1 (calculated from weight ratio of ethanol to ferrocene of 95:5, 93:7, and 91:9). The synthesis time was hold at 45 min [41].

Thonganantakul et al. [46] synthesized CNTs by CVD method using a quart tube reactor. N_2 was used as a carrier gas with the flowrate of 100 cm^3/min. Kerosene which was the mixture of hydrocarbon containing 10-16 carbon atoms was used as a carbon precursor. Ferrocene was used as a catalyst. In their experiment, ceramic boat which contained ferrocene was placed in the middle of the reactor. The reactor was heated to synthesis temperature of 900 °C. After the synthesis temperature was achieved, kerosene was fed into the quartz tube reactor via nozzle with flow rate of 3 cm^3/min. The molar ratio of kerosene to ferrocene was varied from 1:1 to 2.2:1 and 3.3:1 (calculated from weight ratio of kerosene to ferrocene of 1:1, 2:1, and 3:1). Molecular weight of kerosene was assumed at 170 g/mol [47]. The synthesis time was hold at 53 min.

2.4.2.1   Yields of CNT products

From Mongkolsamai et al. [41], yields by weight of CNTs were calculated from weight of CNTs divided by the summation of weight of ferrocene and weight of ethanol. When molar ratio of ethanol to ferrocene increased from 48:1 to 58:1 and 80:1, CNT yields decreased from 9.21% to 6.68% and 4.12%. This result revealed that an increase in molar ratio of ethanol to ferrocene decreased CNT yields. With high proportion of ethanol, a high amount of carbon atoms decomposed from ethanol covered the entire surface of Fe particles, while some remaining carbon atoms could not dissolve into Fe to form CNTs.

From Thonganantakul et al. [46], yields by weight of CNTs were calculated from weight of CNTs divided by the summation of weight of kerosene and weight of ferrocene. When molar ratio of kerosene to ferrocene increased from 1:1 to 2.2:1 and

3.3:1, CNT yields decreased from 56.0% to 41.1% and 25.7%. Their results revealed that an increase in molar ratio of kerosene to ferrocene decreased CNT yields. At high molar ratio of kerosene to ferrocene, the amount of Fe particles was not sufficient for self-assembly of CNTs [46].

2.4.2.2 Morphology of CNTs

From Thonganantakul et al. [46], FESEM was used to observe the morphology of CNTs as shown in **Figure 10**. In this figure, F_K:F_P represented the weight ratio of kerosene to ferrocene which was varied from 1:1 to 2:1 and 3:1. From calculation, molar ratio of kerosene to ferrocene in their experiment was varied from 1:1 to 2.2:1 and 3.3:1, respectively. It was found that CNTs which was synthesized at molar ratio of kerosene to ferrocene of 1:1 presented the lowest CNT diameter with an average diameter of CNTs less than 100 nm. From observation, an increase in molar ratio of kerosene to ferrocene increased average diameters of CNTs.
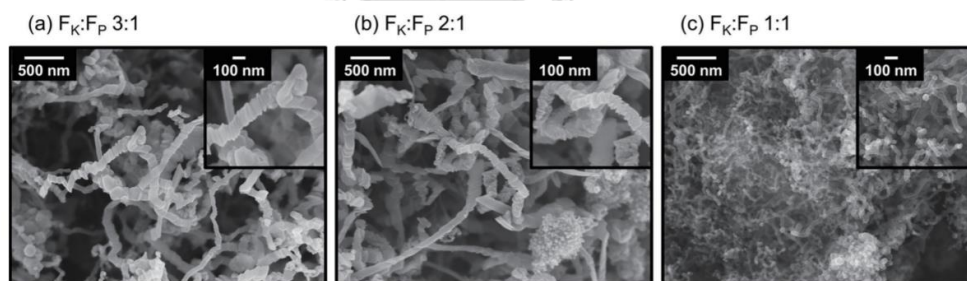
Figure 10 FESEM images of CNTs which was synthesized at 900 °C with various F_K:F_P (a) 3:1 (b) 2:1 (c) 1:1 [46]

2.4.2.3 Crystallinity of CNTs

From Mongkolsamai et al. [41], Raman spectroscopy technique was used to characterize crystallinity of CNTs. The ratio of D-band to G-band (I_D/I_G) was used to identify the crystallinity of carbon product. From their experiment, an increase in molar ratio of ethanol to ferrocene from 48:1 to 58:1 and 80:1 provided I_D/I_G of 0.47, 0.56, and 0.39, respectively, meaning an increase in molar ratio of ethanol to ferrocene from

48:1 to 80:1 decreased the ratio of I_D/I_G from 0.47 to 0.39 resulting in an increase in the crystallinity of CNTs.

2.4.3 Effect of synthesis temperature on properties of CNTs

Synthesis temperature is one of the significant parameters which also affects the properties of CNTs. There were many studies reported on the effect of synthesis temperature on properties of CNTs as followed.

Rabbani et al. [48] synthesized CNTs by CVD method using an injection vertical chemical vapor deposition reactor (IVCVD) with outer diameter 25.4 cm and length 183 cm. P-xylene (C_8H_{10}) was used as a carbon precursor and ferrocene ($C_{10}H_{10}Fe$) was used as a catalyst. Argon (Ar) was used as a carrier gas with flowrate of 1,000 cm^3/min. A 1 wt% of ferrocene in p-xylene was prepared in 50 mL syringe. The reactor was heated to designated temperature by electrical furnace under Ar atmosphere. Then, the solution was sprayed into a vertical reactor by ultrasonic atomizer nozzle with flowrate 1.02 cm^3/min. The synthesis temperature was varied from 750 °C to 950 °C. Synthesis time was fixed at 30 min.

Ming et al. [49] synthesized CNTs by CVD method using reactor equipped with alumina tube connecting with N_2 and CH_4 gases. CH_4 was used as carbon precursor. N_2 was used as a carrier gas with flowrate of 400 cm^3/min. Ni/MgO doped on copper ($Cu_{Ni/MgO}$) was used as a catalyst which weight ratio of Ni:MgO was 80:20 and weight ratio of Ni/MgO in the catalyst was 8 wt%. A 0.5 g of $Cu_{Ni/MgO}$ was placed in the middle of the reactor. The reactor was heated to temperature which was varied from 720 °C to 870 °C with heating rate 5 °C/min. Synthesis time was fixed at 60 min.

Li et al. [50] synthesized CNTs by CVD method using quartz tube reactor. Ethylene (C_2H_2) was used as carbon precursor. N_2 was used as a carrier gas. Fe doped on Silicon dioxide (SiO_2) was used as catalyst. A 0.1 g of catalyst was placed in the middle of the reactor. The reactor was flushed with N_2 with flowrate of 100 cm^3/min for 20 min. The reactor was heated to synthesis temperature which was varied from 600 °C to 1050 °C with heating rate 5 °C/min. At that temperature, C_2H_2, NH_3, and N_2 with flowrates of 10, 40, and 100 cm^3/min, respectively, were fed to the reactor for 2 h.

Lee et al. [51] synthesized CNTs via CVD method using quartz CVD reactor. C_2H_2 was used as a carbon source. Fe deposited on SiO_2 was used as a catalyst which the size of catalyst substrate was 20 mm×30mm. Catalyst was placed in the middle of the reactor. Then, catalyst was treated with NH_3 with flow rate 100 cm^3/min for 20 min to form the catalytic particles in nanometer size. Temperature for catalyst treatment was used in the range of 750 °C to 950 °C. After that, Ar was used as a carrier gas with flowrate 1000 cm^3/min and C_2H_2 was fed into the reactor with flow rate 30 cm^3/min. The synthesis temperature were varied from 750 °C, 850 °C, and 950 °C for 10 min for the CNT growth.

2.4.3.1 Yields of CNT products

From Rabbani et al. [48], yields by weight of CNTs as shown in **Figure 11** were calculated from weight of CNTs divided by weight of p-xylene. Their results revealed that an increase in synthesis temperature from 750 °C to 850 °C increased CNT yields from 2.3% to 7.0%. Non-tube-shaped structure were found at 750 °C, whereas aligned CNTs were found at 850 °C. However, an increase in synthesis temperature from 850 °C to 950 °C decreased CNT yields from 7.0% to 5.8% due to the agglomeration of Fe particles resulting in an increase in diameter of CNTs.
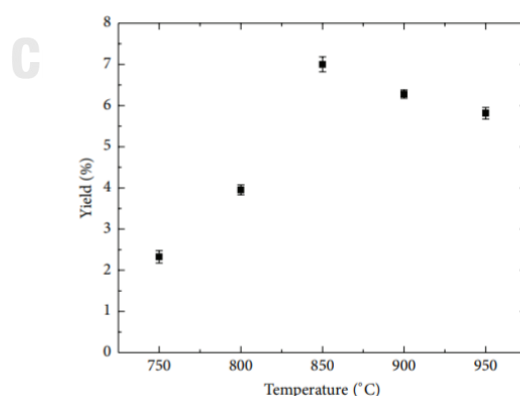
Figure 11 Yields of CNTs at varied temperature synthesized from P-xylene and ferrocene [48]

From Ming et al. [49], yields by weight of CNTs as shown in **Figure 12** were calculated from weight of catalyst after reaction minus by weight of catalyst before

reaction and divided by weight of catalyst before reaction. Their results found that an increase in synthesis temperature from 720 °C to 820 °C raised CNT yield from 210% to 278% due to the higher decomposition of carbon precursor. However, an increase in synthesis temperature from 820 °C to 870 °C decreased CNT yield from 278% to 240% due to the sintering of metal particles resulting in the bigger diameter of CNTs. In addition, their research indicated that at low synthesis temperature, decomposition of carbon precursor was dominated. At high synthesis temperature, the coalescence of metal particles was dominated.
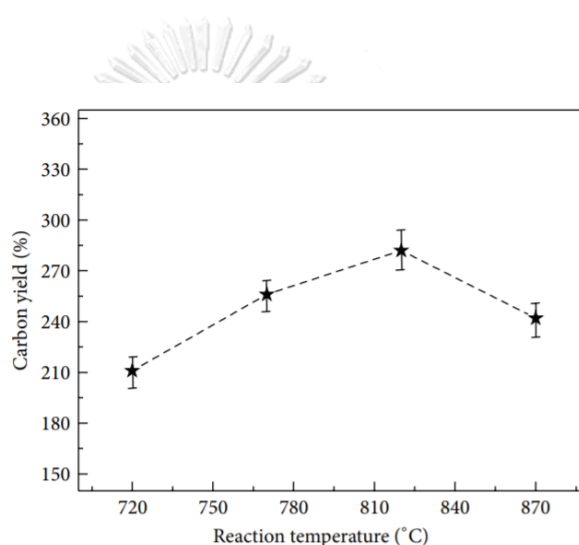
Figure 12 Yields of CNTs at varied temperature synthesized from CH_4 and $Cu_{Ni/MgO}$
[49]

From Li et al. [50], yields by weight of CNTs as shown in **Figure 13** were calculated from weight of catalyst after reaction minus by weight of catalyst before reaction and divided by weight of catalyst before reaction. Their results found that an increase in synthesis temperature from 600 °C to 900 °C raised CNT yield from 10% to 700% due to the higher decomposition rate of carbon precursor and the higher dissolving rate, and diffusing rate of carbon atoms. However, an increase in synthesis temperature from 900 °C to 1050 °C decreased CNT yield from 700% to 250% due to the agglomeration of metal particles. Moreover, when synthesis temperature was higher

than 900 °C, carbon and iron would react with each other to form iron carbide resulting in losing of surface area of catalyst [50].
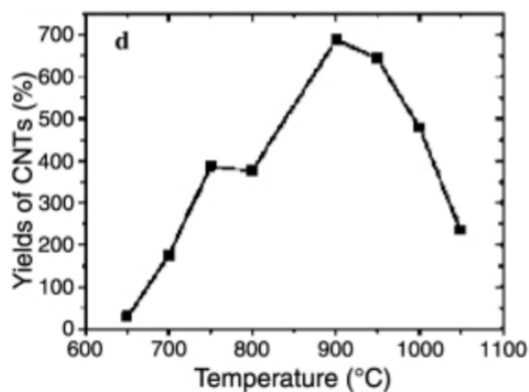
Figure 13 Yields of CNTs at varied temperature synthesized from C_2H_2 and Fe doped SiO_2 [50]

2.4.3.2   Morphology of CNTs

From Rabbani et al. [48], morphology of CNTs were characterized by FESEM. **Figure 14** indicated that there were unreacted particles occurred in CNTs which was synthesized at 750 °C. There were no unreacted particles found at synthesis temperature 850 °C while aligned CNTs was were observed. At synthesis temperature of 950 °C, CNTs were found as random tubes.
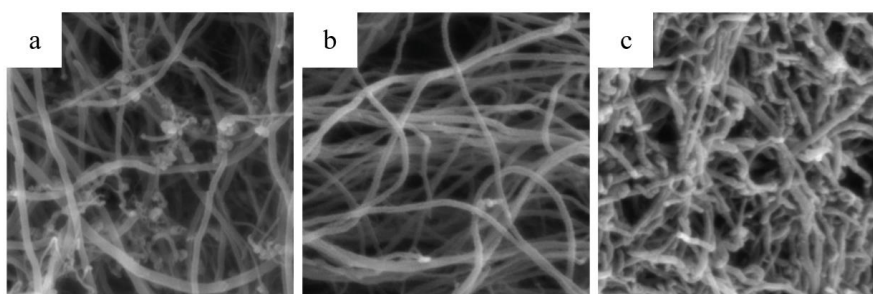
Figure 14 Morphology of CNTs at various synthesis temperature (a) 750 °C (b) 850 °C (c) 950 °C [48]

From Ming et al. [49], morphology of CNTs were characterized by a FESEM (JEOL, JSM-6300, Japan). The accelerating voltage was set at 20 kV. The magnification was set at 200000x. **Figure 15** indicated that the diameters of CNTs were 34 nm, 39 nm, 47 nm, and 52 nm when the synthesis temperature was 720 °C, 770 °C, 820 °C, and 870 °C, respectively. An increase in CNT diameters was obtained due to an agglomeration of metal particles.
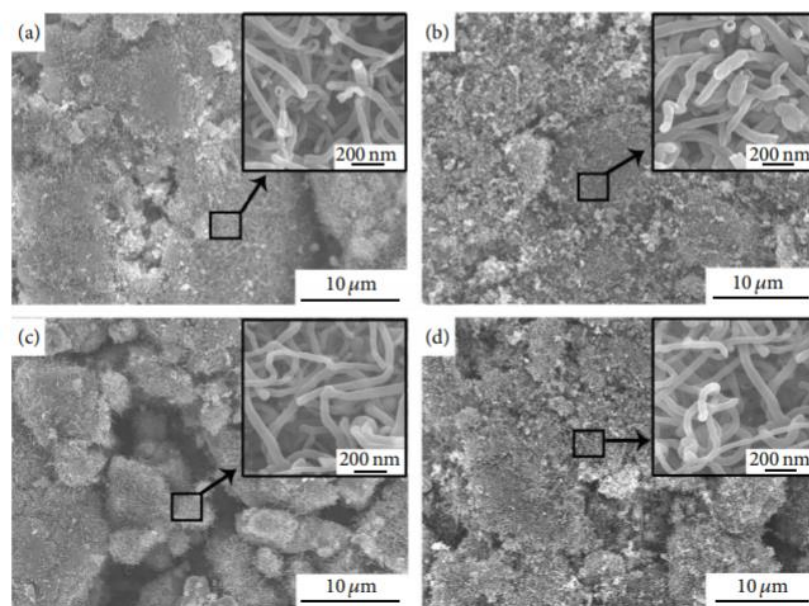
Figure 15 Morphology of CNTs at various synthesis temperature (a) 720 °C
(b) 770 °C (c) 820 °C (d) 870 °C [49]

From Li et al. [50], the morphology of CNTs were shown in **Figure 16(a)-(c)**. From the observation in transmission electron microscopy (TEM) images, CNTs had a bamboo-like morphology. When synthesis temperature raised from 650 °C to 1050 °C, an outer diameter of CNTs increased due to the increment in the number of CNT walls or graphene layers. In addition, an increment in synthesis temperature also raised an inner diameter of CNTs due to the agglomeration of Fe which was doped on SiO_2 as a catalyst. An increase in inner and outer diameter of CNTs were shown in **Figure 16(d)-(f)**. When the temperature increased from 650 °C to 800 °C and 1050 °C, the diameter

of CNTs increased from 13 to 23 and 65 nm with the graphene layer increased from 12 to 24 and 50 layers, respectively [50].
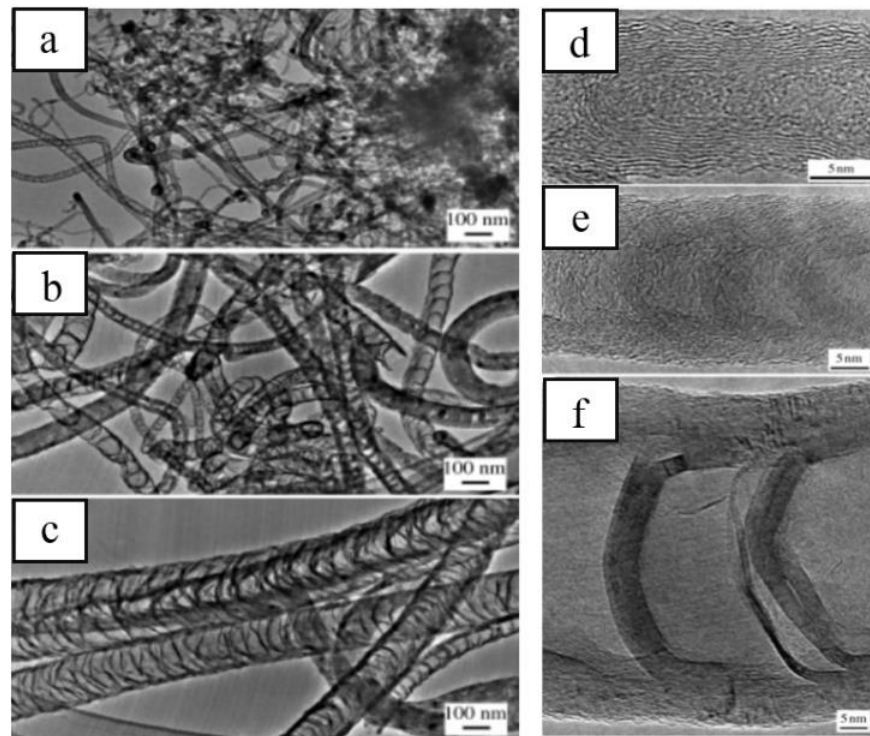
Figure 16(a)-(c) Low-magnification Transmission Electron Microscopy (TEM) images and (**d)-(f)** High-magnification TEM images of CNTs at 760 Torr with temperature of (a) and (d) 650 °C, (b) and (e) 800 °C, (c) and (f) 1050 °C [50]

From Lee et al. [51], morphology of CNTs were characterized by a FESEM (Hitachi, S-800). The accelerating voltage was set at 30 kV. **Figure 17(a)** indicated that there were some unreacted particles occurred on the surface of CNTs which was synthesized at 750 °C. Unreacted particles did not occurred on the surface of CNTs which were synthesized at 850 °C and 950 °C as shown in **Figure 17(b)-(c)**. Diameters of CNTs were 30±5 nm, 60±10 nm, and 130±20 nm when the synthesis temperature was 750 °C, 850 °C, and 950 °C, respectively. An increase in CNT diameters were due to an agglomeration of Fe particles on SiO_2 surface. Size of Fe particles were 40±10 nm, 90±20 nm, and 150±40 nm when the synthesis temperatures were 750 °C, 850 °C, and 950 °C, respectively.
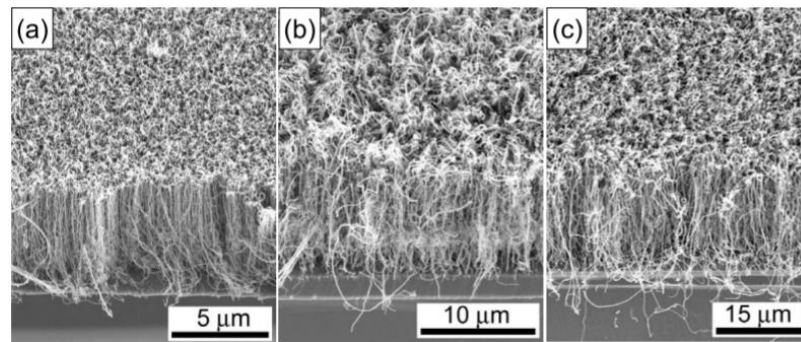
Figure 17 FESEM images of CNTs at various synthesis temperature (a) 750 °C
(b) 850 °C (c) 950 °C [51]

2.4.3.3   Thermal stability of CNTs

From Lee et al. [51], thermal stability of CNTs was characterized by a thermogravimetric analyzer. TGA was used at heating rate of 10 °C/min in air. TGA curves of CNTs at various synthesized temperature varied from 750 °C to 850 °C and 950 °C were showed in **Figure 18**. This evidence revealed that weights of CNTs sample were lost over the range of 300-600 °C, 450-650 °C, and 500-670 °C when synthesis temperature increased from 750 °C to 850 °C and 950 °C, respectively. It could indicate that CNTs had more thermal stability when the synthesis temperature increased.
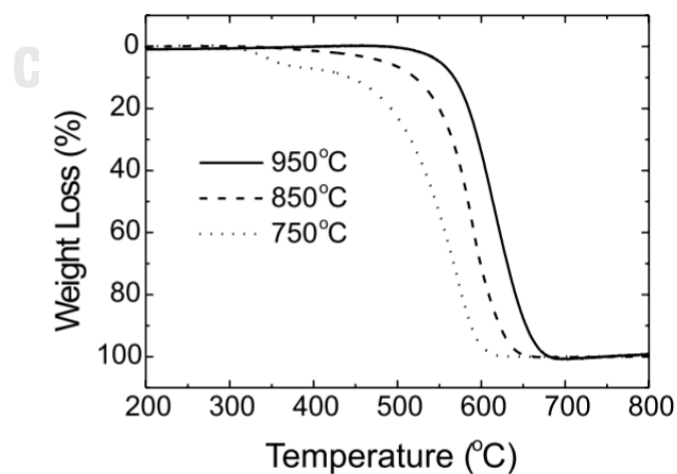
Figure 18 TGA curves of CNTs at various synthesized temperature [51]

2.4.3.4 Crystallinity of CNTs

From Ming et al. [49], Raman spectroscopy technique was used to characterize crystallinity of CNTs. Raman spectroscope (Bruker RFS-27, Germany) was used with laser at wavelength 1064 nm. From **Figure 19**, the peak in region of 1250-1450 cm^{-1} was attributed to D-band which represented the presence of amorphous carbon. The peak in region of 1587-1598 cm^{-1} was attributed to G-band which represented the presence of CNT structure. The ratio of D-band to G-band (I_D/I_G) was used to identify the crystallinity of carbon product. From their experiment, an increase in synthesis temperature decreased I_D/I_G. Therefore, a decrease in I_D/I_G could be attributed to an increase in CNT structure in carbon product.
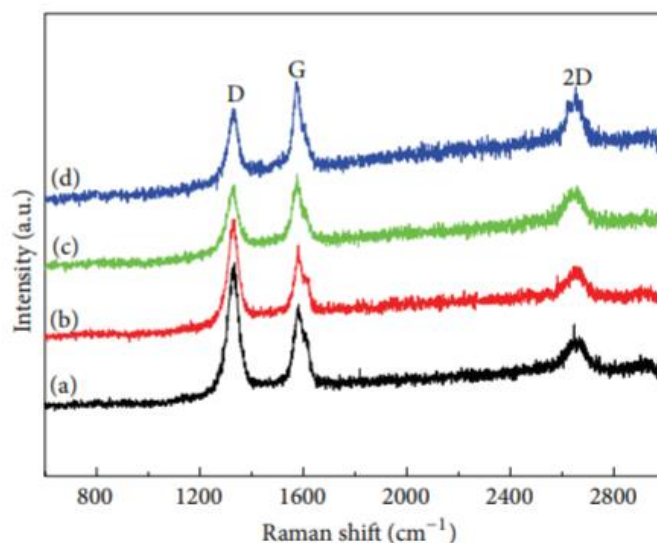
Figure 19 Raman spectra of CNTs at various synthesis temperature (a) 720 °C
(b) 770 °C (c) 820 °C (d) 870 °C [49]

From Lee et al. [51], Raman spectroscopy technique was used to characterize crystallinity of CNTs. Raman spectroscope was used with laser at wavelength 632.8 nm. From **Figure 20**, the peak at 1334 cm^{-1} was attributed to D-band which represented the presence of amorphous carbon. The peak at 1582.7 cm^{-1} was attributed to G-band which represented the presence of CNT structure. From their experiment, an increase in synthesis temperature from 750 to 950 °C decreased I_D/I_G from 1.2 to 0.8. Therefore,

a decrease in I_D/I_G could be attributed to an increase in CNT structure in carbon product. The Raman spectra results were consistent with FESEM images and TGA curves which mentioned that an increase in synthesis temperature increased the amount of CNT structure in carbon product, crystallinity, and thermal stability of CNTs [51].
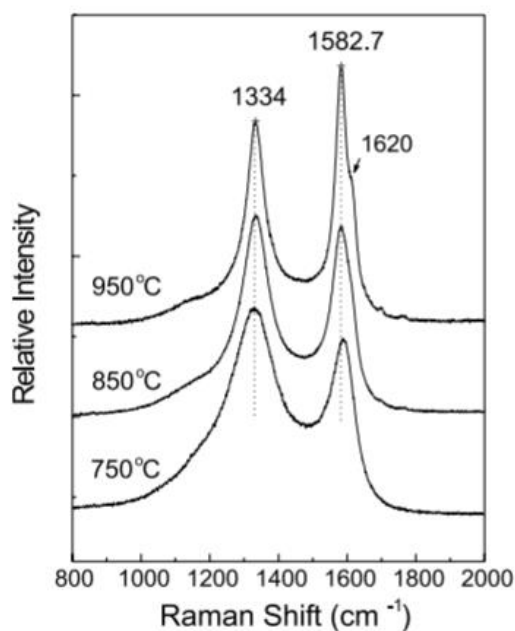
Figure 20 Raman spectra of CNTs at various synthesis temperature [51]

2.4.4 Use of CNTs as a catalyst support in CO_2 methanation

CNTs can be used as a support material for the catalyst in CO_2 methanation. Ni metal was selected in this work to be the active metal due to the advantages of Ni as described in section 2.2.1. Use of CNTs support material for Ni-based catalyst was studied by Feng et al. [32]. Effect of support materials were studied in their work. Ni/CNTs and Ni/Al_2O_3 catalysts were synthesized by impregnation method. CNTs were mixed with a solution of Ni(NO_3)$_2$ and DI water with 12 wt% Ni loading. Then, solution was stirred 2 h and was evaporated at 70 °C in water bath. After that, catalyst was dried at 100 °C for 12 h and was calcined in N_2 at 350 °C for 4 h. For Ni/Al_2O_3 catalyst was prepared by the same steps. CO_2 methanation was conducted by loading 0.1 g of catalyst into the reactor. Their reaction was performed at 350 °C for 400 min with the

molar ratio of $H_2:CO_2$ was 4:1. The experimental data was collected at every 40 min. Yield of CH_4 was analyzed by gas chromatograph (GC-1690 model) equipped with thermal conductivity detector (TCD) [32].

CH4 yields with various catalyst were shown in **Figure 21**. This figure indicated that Ni/CNTs reached higher CH_4 yield when compared with Ni/Al_2O_3 because Ni/CNTs had the high surface area and good reducibility as observed from BET surface area and H_2-TPR results which would be described later.
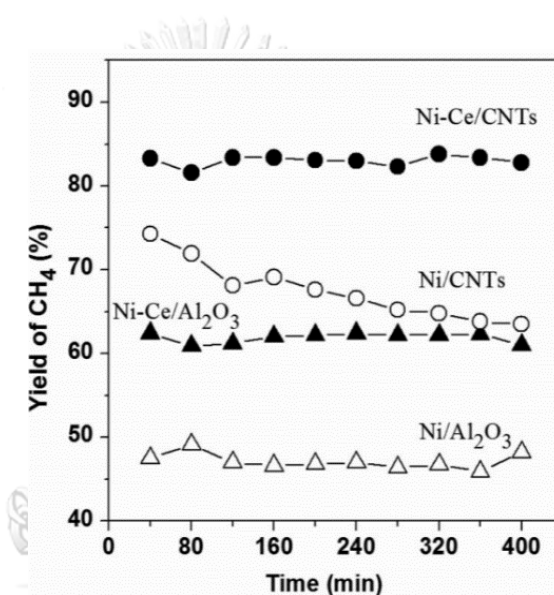
Figure 21 CH4 yield with various catalysts [32]

N2 adsorption/desorption (Quatachrome Nova 1000e) was measured at 77 K. Catalysts were degassed at 300 °C for 3 h. The results of BET surface area of catalysts were shown in **Table 2.** From **Table 2**, surface area of Ni/CNTs and Ni/Al_2O_3 were 172.8 m^2/g and 152.7 m^2/g, respectively. Their results indicated that Ni/CNT catalyst had the higher BET surface area than Ni/Al_2O_3.

Table 2 BET surface areas of different catalysts [32]

Sample	Surface area (m^2/g)
Ni/CNTs	172.8
Ni-Ce/CNTs	167.5
Ni/Al$_2$O$_3$	152.7
Ni-Ce/Al$_2$O$_3$	142.5

The reducibility of catalyst was characterized by H_2-TPR technique. A 0.05 g of catalyst was loaded in the equipment with the temperature was increased from 50 °C to 850 °C with heating rate of 5 °C/min under 5 wt% H_2 in N_2 with flowrate of 30 mL/min. The reducibility of catalyst was interpreted by the position of peak at low temperature and H_2 consumption which could be estimated from peak area of H_2-TPR. Higher reducibility of catalyst was obtained when first peak could be observed at lower temperature and catalyst had higher peak area. **Figure 22** showed the H_2-TPR profiles of various catalysts. Ni/CNTs had the peak at 330 °C and 480 °C, respectively, while Ni/Al$_2$O$_3$ had the peak at 420 °C and 530 °C, respectively. It could be concluded that Ni/CNTs could be reduced easier compared with Ni/Al$_2$O$_3$ because first peak could be observed at the lower temperature and it had high intensity of peak at low temperature and high peak area. The results from BET surface area and H_2-TPR supported the result from the plot of the effect of time on CH$_4$ yield as shown in **Figure 21**. Ni/CNTs reached the high CH$_4$ yield because it had the high surface area and good reducibility [32].
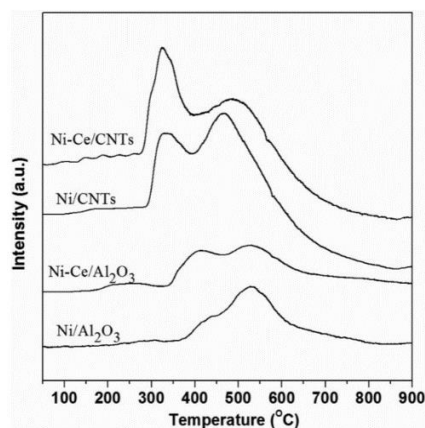
Figure 22 H_2-TPR profiles of various catalysts [32]

Wierzbicki et al. [52] studied wt% of Fe on Ni-Fe catalysts derived from co-precipitation method. CO_2 methanation was performed as a catalytic performance test. Catalyst was placed in a fixed-bed reactor with the molar ratio of $CO_2/H_2/Ar$ at 3/12/5 with total flow of 100 cm^3/min. The reaction temperature was varied from 250 to 450 °C. Their research revealed that an increase in wt% Fe decreased CO_2 conversion because the reverse water-gas shift reaction occurred at high Fe content. Ni-Fe with 20 wt% Ni and 1.5 wt % Fe provided the highest CO_2 conversion as shown in **Figure 23** due to its highest reducibility. The reducibility of Ni-Fe catalysts were shown in **Figure 24** which were characterized by H_2-TPR technique. The results revealed that 20 wt% Ni and 1.5 wt% Fe catalyst had the highest reducibility because it had the lowest first-reducing temperature.
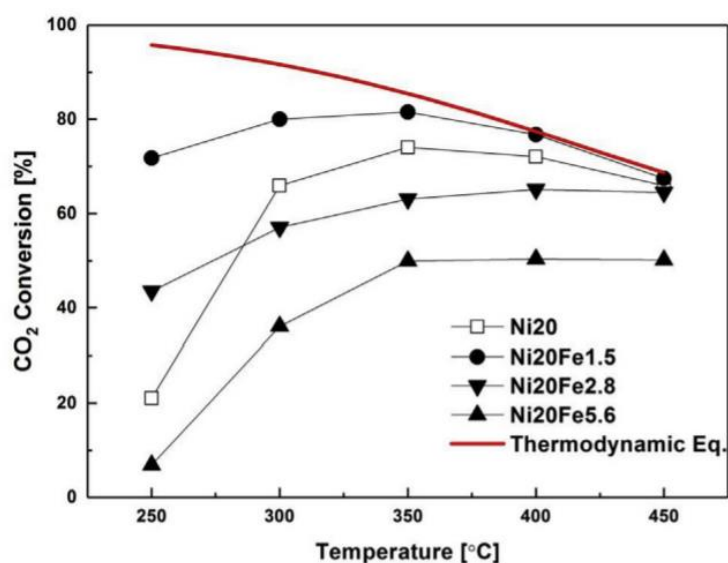
Figure 23 CO_2 conversion of Ni-Fe catalyst at various Fe contents [52]
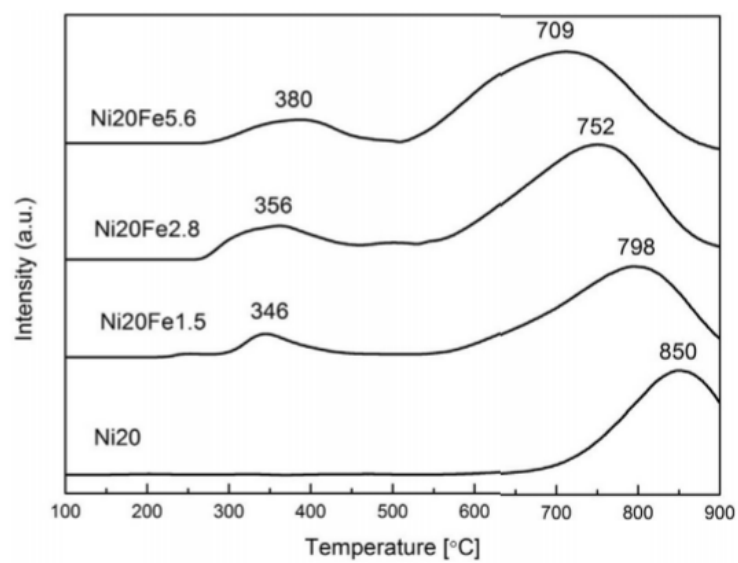
Figure 24 H_2-TPR of Ni-Fe catalyst at various Fe contents [52]

CHAPTER 3
RESEARCH METHODOLOGY

In this research, the experiment were divided into 3 parts. The first part was the synthesis of CNTs at various molar ratio of carbon precursor and ferrocene and different pyrolysis temperatures. The second part was the preparation of bimetallic Ni-Fe/CNT catalyst at various weight ratio Ni to Fe catalyst using CNTs as a support material. The last part was catalyst performance test in methanation of CO_2 comparing the performance of synthesized CNTs with commercial CNTs.

3.1 Material and chemicals

CNTs were synthesized via a co-pyrolysis of eucalyptus oil which the main component was eucalyptol ($C_{10}H_{18}O$) as carbon source and ferrocene ($C_{10}H_{10}Fe$) as catalyst. Elemental composition of eucalyptus oil was listed in **Table 3**, while ferrocene was 98% analytical grade obtained from Sigma-Aldrich. Nitrogen (99.6% ultra-high purity industrial grade, Linde) was used as a carrier gas. Commercial CNTs obtained from Bayer Material Science was used as benchmarking sample in the study. A simple impregnation method was used for catalyst preparation. Nickel nitrate hexahydrate ($Ni(NO_3)_2 \cdot 6H_2O$) (99%, AR grade, KEMAUS) and iron nitrate nonahydrate ($Fe(NO_3)_3 \cdot 9H_2O$) (98%, AR grade, LOBA CHEMIE) were used as metal precursors, while solvent was ethanol (99.9%, AR grade, QRec).

Table 3 Elemental content of eucalyptus oil

Element	Percentage composition (wt%)
Carbon	47.62
Hydrogen	6.72
Nitrogen	1.12
Oxygen	44.54

3.2 Synthesis and characterization of carbon nanotubes

CNTs were synthesized via CVD method by co-pyrolysis with ferrocene [41, 53]. The experimental set up of CNT synthesis was shown in **Figure 25**. The quartz tubular reactor (outer diameter 3 cm and length 100 cm) was heated by using an electrical furnace from room temperature to various pyrolysis temperature (T_{pyro}) (800, 850 and 900 °C) in 30 minutes under nitrogen flow of 20 cm^3/min at atmospheric pressure. When the furnace reached the desired temperature, 1 g ferrocene in the ceramic boat was shifted into the middle of the quartz tube. Then, eucalyptus oil with various molar ratio of oil to ferrocene ($m_{oil/fer}$) (1:1, 2:1, and 3:1) was sprayed into the reactor with a flow rate of 0.17 cm^3/min. After 30 minutes of reaction time, carbon products were collected from the surface of the quartz tube.
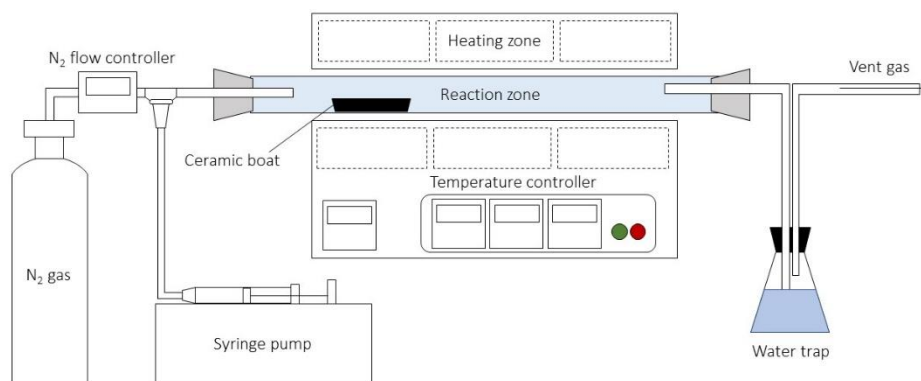
Figure 25 Experimental setup for synthesizing CNTs

The morphology of CNTs were characterized by Field Emission Scanning Electron Microscopy (FESEM), thermal stability was measured by thermogravimetric analysis (TGA), surface area was determined by N_2 adsorption/desorption analysis. The crystallinity of CNTs was characterized by Raman spectroscopy.

3.2.1   Field emission scanning electron microscope (FESEM)

Structure and morphology of CNTs was characterized by field emission scanning electron microscopy technique using field emission scanning electron microscope (FESEM, JSM-6400) equipped with energy dispersive X-ray spectroscope (EDX) at the Scientific and Technological Research Equipment Centre, Chulalongkorn University. FESEM images were performed with 50,000X magnification. The quality of synthesized CNTs could be interpreted by the proportion of CNT structure (tube-shaped carbon) to amorphous carbon (non-tube-shaped carbon) in each figure. Higher quality of synthesized CNTs were obtained when there were higher proportion of CNT structure to amorphous carbon.

3.2.2   Thermogravimetric analyzer (TGA)

Thermal stability of CNTs was characterized by thermogravimetric analyzer (TGA, Mettler-Toledo TGA/DSC1, STARe System) at Center of Excellence in Particle Technology and Material Processing Laboratory, Chulalongkorn University. A 0.4 g of CNTs was inserted into the equipment. TGA curves were taken from temperature 30 to 900 °C under a heating rate 10 °C/min in oxygen flow of 50 ml/min. Thermal stability of synthesized CNT were observed from the decomposition temperature of synthesized CNTs. Higher thermal stability of synthesized CNT was achieved if the decomposition temperature was shifted to higher temperature.

3.2.3 N_2 adsorption/desorption

Surface area of CNTs was characterized by N_2 adsorption/desorption (Micromeritics, 3flex) at Department of Chemical Engineering, Chulalongkorn University. CNT sample was degassed under Argon flow at 300 °C for 5 h. Lower surface area of synthesized CNTs was obtained when there were higher proportion of CNT structure to amorphous carbon.

3.2.4   Raman spectroscopy

Crystallinity of CNTs was measured by Raman spectroscopy (NT-MDT, model NTEGRASpectra) under red laser with a wavelength of 632.8 nanometers. Raman shift was studied in the range of 1000 cm^{-1} to 2000 cm^{-1}. For CNT characterization, a peak at Raman shift 1344 cm^{-1} could be assigned to the vibration of non-sp^2 bonded carbon atom which was called D-band. Generally, D-band was applied to identify amorphous carbon. A peak at 1576 cm^{-1} could be assigned to the vibration of sp^2 bonded carbon atom which was called G-band. Generally, G-band was applied to identify CNTs. The intensity of D-band to G-band (I_D/I_G) was used to identify the crystallinity of carbon product. The higher crystallinity of carbon product was obtained at lower I_D/I_G.

3.3 Preparation of bimetallic Ni-Fe on carbon nanotubes

The catalysts were prepared by the simple impregnation method with 30 wt% metal loading [32]. To prepare the Ni-Fe/CNT with various weight ratio of Ni to Fe (0:1, 1:3, 1:1, 3:1, and 1:0), CNTs were added in the solution of Ni(NO$_3$)$_2$·6H$_2$O or Fe(NO$_3$)$_3$·9H$_2$O with 4 mL of ethanol. After that, the sample was dried in an oven at 100 °C for 12 h. Then, an impregnated catalyst was calcined at 350 °C for 3 h in the air to convert dried metal nitrate into metal oxide.

The Ni-Fe/CNT was characterized by various techniques: X-ray diffraction (XRD) was used to identify catalyst crystal structure and temperature-programmed reduction in H$_2$ (H$_2$-TPR) was applied to observe the reducibility of the catalyst.

3.3.1   X-ray diffraction (XRD)

The crystallographic properties of catalyst were characterized by X-ray diffraction (XRD, D 76181, Bruker AXS). XRD pattern was recorded in the 2θ range from 5° to 80° (Cu Kα1, 40 kV, 300 mA) with scanning speed of 10°/min. The average crystalline size (d) of NiO was evaluated using the Scherer equation shown in **Eq. 2**.

$$d = \frac{K\lambda}{\beta cos\theta}$$

Equation 2

where K, the Scherrer constant, which was taken to be 0.94, λ was the wavelength of the X-ray, β is the line width at half maximum height of the peak in radians and θ is the position of the peak in radians.

3.3.2 Temperature-programmed reduction in H_2 (H_2-TPR)

Reducibility of catalyst was characterized by temperature-programmed reduction in H_2 (H_2-TPR, Chemstar TPx, TCD detector). Generally, catalyst was preheated at 150 °C for 1 h. After that, H_2-TPR was performed under a flow of 10 wt% H_2 in Ar at flowrate of 50 mL/min. U-tube quartz reactor was filled with 500 mg of calcined catalysts. Then, the temperature was heated from 100 °C to 900 °C with a heating rate 5 °C /min.

3.4 Performance test

The experimental setup of CO_2 methanation was shown in **Figure 26**. The reaction was conducted in a fixed bed reactor [54]. Prior to the reaction, 100 mg of Ni-Fe/CNT was packed at the middle of the horizontal quartz tube with 0.8 mm inner diameter and 600 mm long. The catalyst was reduced in H_2 with flow rate of 28 mL/min at 500 °C for 1 h to change metal oxide to the active metal. Then, the gas mixture of CO_2: H_2: He with the molar ratio of 1:4:5 was fed into the reactor. The total flow rate and reaction temperature was fixed at 77 mL/min and 325 °C, respectively. The reaction time was fixed at 20 minutes. At the end of reaction time, the reaction was in equilibrium.
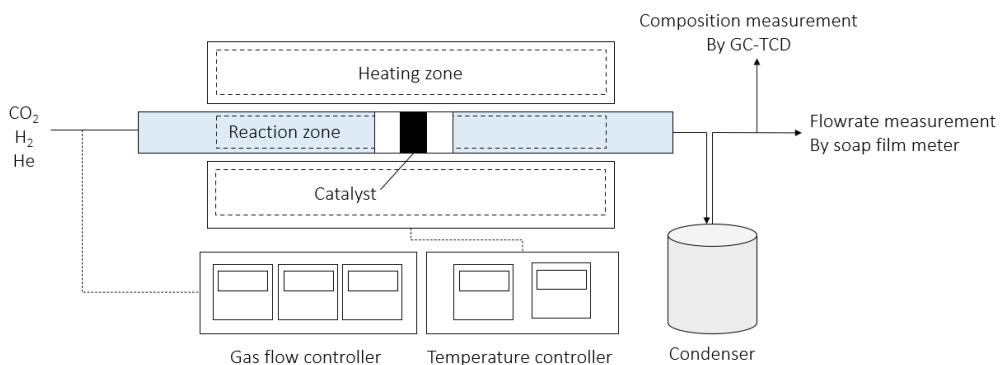
Figure 26 Experimental setup for CO$_2$ methanation

The product gas was analyzed by gas chromatography (GC-8A, Shimadzu) equipped with a TCD detector. Then, CO$_2$ conversion (X_{CO2}) and CH$_4$ selectivity (S_{CH4}) were calculated based on the gas composition and outlet flow rate by following **Eq. 3 and 4**. The details of these calculation was shown in **Appendix F**.

$$X_{CO2}(\%) = \frac{[CO_2]_{in} \times F_{in} - [CO_2]_{out} \times F_{out}}{[CO_2]_{in} \times F_{in}} \times 100 \qquad \text{Equation 3}$$

$$S_{CH4}(\%) = \frac{[CH_4]_{out}}{[CO]_{out} + [CH_4]_{out}} \times 100 \qquad \text{Equation 4}$$

CHAPTER 4
RESULTS AND DISCUSSION

This research focused on synthesis of CNTs at a pyrolysis temperature (T_{pyro}) range of 800 °C, 850 °C, and 900 °C and a eucalyptus oil to ferrocene molar ratio ($m_{oil/fer}$) range of 1:1, 2:1, and 3:1. CNT properties were characterized by various techniques including FESEM, TGA, Raman spectroscopy, and N_2 adsorption/desorption. An appropriate condition for synthesizing high-quality CNTs was determined. Then, CNTs synthesized at the optimal condition were used as a support material in Ni-Fe/CNT catalyst employed for methanation process. Effects of impregnation method with different calcination temperatures (250 °C, 300 °C, 350 °C, and 400 °C) and weight ratio of Ni to Fe (1:0, 3:1, 1:1, 1:3, and 0:1) were investigated. XRD and H_2-TPR analyses were conducted to identify the characteristics of Ni-Fe/CNT catalysts. CO_2 conversion, CH_4 selectivity, CH_4 yield of Ni-Fe/CNT catalysts were finally analyzed.

4.1 Synthesis of carbon nanotubes

For the synthesis of CNTs, eucalyptus oil and ferrocene were vaporized within a quartz tubular reactor heated by an electrical furnace equipped with a temperature controller. The temperature profile along the tubular reactor was shown in **Figure 27**. A ceramic boat containing a designated amount of ferrocene was shifted into the heating zone of the reactor at the position of 35 cm from the reactor inlet. Then, the designated amount of eucalyptus oil was sprayed. With this setting, it could be confirmed that T_{pyro} could be controlled at the designated value (800, 850, and 900 °C).
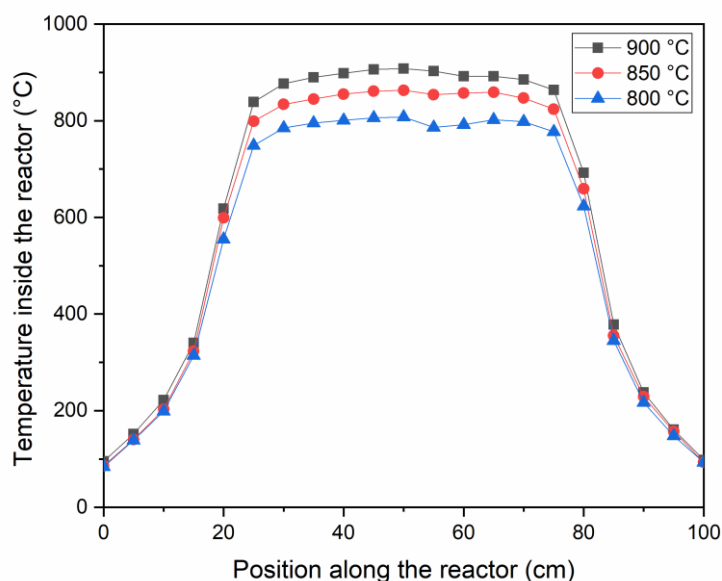
Figure 27 Temperature profile at different position along the tube

4.1.1 Yields of synthesized CNTs

Synthesis of CNTs was performed by the co-pyrolysis of eucalyptus oil and ferrocene under the nitrogen atmosphere at various T_{pyro} and $m_{oil/fer}$. As mentioned above, T_{pyro} was varied from 800 °C to 850 °C and 900 °C, while $m_{oil/fer}$ was varied from 1:1 to 2:1 and 3:1. Yields by weight of synthesized products could be calculated by **Eq. 5**, in which weight of eucalyptus oil at various $m_{oil/fer}$ was calculated from **Eq. A1** in Appendix A. Detailed calculations of product yield at various T_{pyro} and $m_{oil/fer}$ was shown in **Table A2-A5** in Appendix A.

$$\text{Product yield (\%)} = \frac{W_p}{W_{oil}+W_{fer}} \qquad \text{Equation 5}$$

Where W_p represented weight of carbon product

     W_{oil} represented weight of eucalyptus oil

     W_{fer} represented weight of ferrocene

Yields by weight of synthesized product at various $m_{oil/fer}$ (1:1, 2:1, 3:1) with different T_{pyro} were shown in **Figure 28**. When focusing on the effect of T_{pyro}, at T_{pyro} of 800 °C, product yields were 41.4±6.3%, 32.7±6.3%, and 21.4±6.5% for $m_{oil/fer}$ of 1:1, 2:1, and 3:1, respectively. At T_{pyro} of 850 °C, product yields were 46.8±9.0%, 40.9±3.1%, and 38.3±2.5% for $m_{oil/fer}$ of 1:1, 2:1, and 3:1, respectively. At T_{pyro} of 900 °C, product yields were 41.7±7.6%, 38.8±3.4%, and 36.2±4.2% for $m_{oil/fer}$ of 1:1, 2:1, and 3:1, respectively. A decrease in product yield when $m_{oil/fer}$ increased was due to the insufficient amount of Fe catalysts at the higher $m_{oil/fer}$ and the decomposition of amorphous carbon obtained from the higher oxygen content in eucalyptus oil because of the higher $m_{oil/fer}$.

When focusing on the effect of $m_{oil/fer}$, at $m_{oil/fer}$ of 1:1, product yields were 41.4±6.3%, 46.8±9.0%, and 41.7±7.6% for T_{pyro} of 800 °C, 850 °C, and 900 °C, respectively. At $m_{oil/fer}$ of 2:1, product yields were 32.7±6.3%, 40.9±3.1%, and 38.8±3.4% for T_{pyro} of 800 °C, 850 °C, and 900 °C, respectively. At $m_{oil/fer}$ of 3:1, product yields were 21.4±6.5%, 38.3±2.5%, and 36.2±4.2% for T_{pyro} of 800 °C, 850 °C, and 900 °C, respectively. From T_{pyro} 800 °C to 850 °C, the increase in product yield was derived from the acceleration in rate of decomposition of eucalyptus oil and ferrocene. From T_{pyro} 850 °C to 900 °C, the decrease in product yield was related to from the agglomeration of Fe catalyst. The details for each effect were discussed in section 4.1.1.1 and 4.1.1.2.
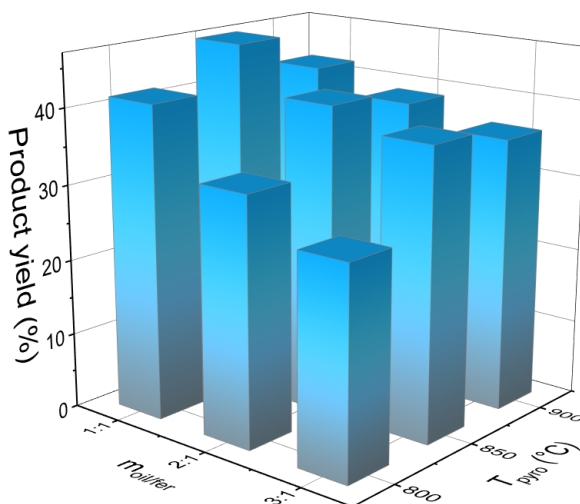
Figure 28 Yield of synthesized CNTs at various $m_{oil/fer}$ and T_{pyro}

4.1.1.1. Effect of molar ratio of eucalyptus oil to ferrocene

Figure 29(a) showed the plot between product yield by weight (%) and molar ratios of eucalyptus oil to ferrocene ($m_{oil/fer}$) which was varied from 1:1 to 2:1 and 3:1. At T_{pyro} of 800 °C product yields were 41.4±6.3%, 32.7±6.3%, and 21.4±6.5% for $m_{oil/fer}$ of 1:1, 2:1, and 3:1, respectively, as shown in **Figure 29(b)**. From **Figure 29(c),** at T_{pyro} of 850 °C product yields were 46.8±9.0%, 40.9±3.1%, and 38.3±2.5% for $m_{oil/fer}$ of 1:1, 2:1, and 3:1, respectively. From **Figure 29(c),** at T_{pyro} of 900 °C product yields were 41.7±7.6%, 38.8±3.4%, and 36.2±4.2% for $m_{oil/fer}$ of 1:1, 2:1, and 3:1, respectively. **Figure 29(b)-(c)** showed that product yields decreased when $m_{oil/fer}$ increased. A decrease in product yield would be attributed to two possible reasons, which were (i) the less amount of Fe catalysts were generated and (ii) decomposition of amorphous carbon was promoted by the higher oxygen content because of the higher $m_{oil/fer}$.
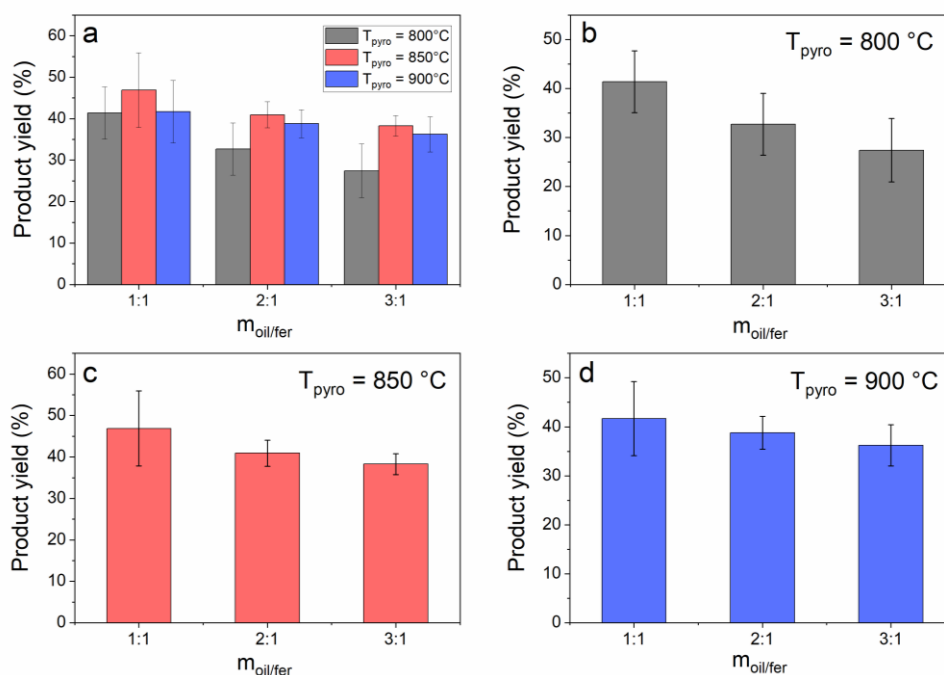
Figure 29 Product yield (%) at various $m_{oil/fer}$ (a) with different T_{pyro} and T_{pyro} of (b) 800 °C (c) 850 °C (d) 900 °C

The first possible reason used to explain a decrease in product yield when $m_{oil/fer}$ increased was attributed to the less amount of Fe catalysts. For the supporting information, it could be observed from the plot between product yield and weight of product at various $m_{oil/fer}$ with T_{pyro} of 900 °C as shown in **Figure 30** and the plot of gas flowrate going out from the reactor at various $m_{oil/fer}$ as shown in **Figure 31**. From **Figure 30,** an increment in $m_{oil/fer}$ from 1:1 to 2:1 and 3:1 could enhance product weight from 0.72 g to 0.97 g and 1.17 g, respectively. An increase in product weight could be referred to the growth of CNT rather than amorphous carbon (as confirmed by FESEM, Raman, and TGA). However, a slight decrease in product yield could be ascribed to the lower amount of Fe catalyst with the higher $m_{oil/fer}$. At $m_{oil/fer}$ of 1:1, CNTs could be formed on the sufficient surface of the Fe catalyst [55]. However, at $m_{oil/fer}$ of 2:1 and 3:1, the relative amount of Fe catalyst would obviously be decreased because of the lower content of ferrocene when compared to eucalyptus oil. In addition, the lower product yield at the higher $m_{oil/fer}$ would be attributed to the higher amount of carbon clusters that would cover surface of Fe catalysts resulting in the loss of active surface for CNT growth. Thus, the higher amount of carbon clusters would leave the reactor before depositing on the less available Fe catalyst. The higher amount of the unreacted carbon clusters in the gas flow at the higher $m_{oil/fer}$ could be detected as shown in **Figure 31**.
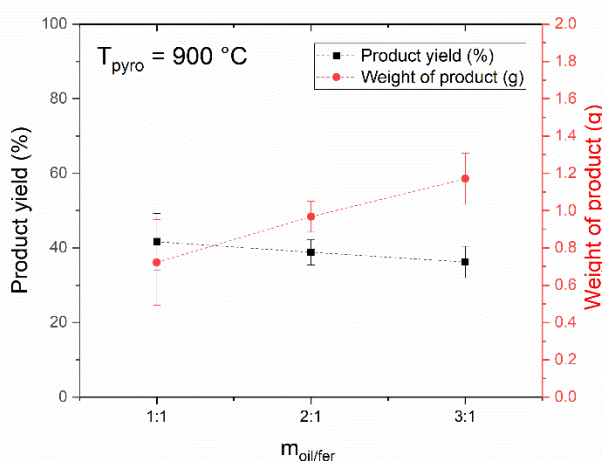
Figure 30 Product yield (%) and weight of product at various $m_{oil/fer}$ with T_{pyro} of 900 °C
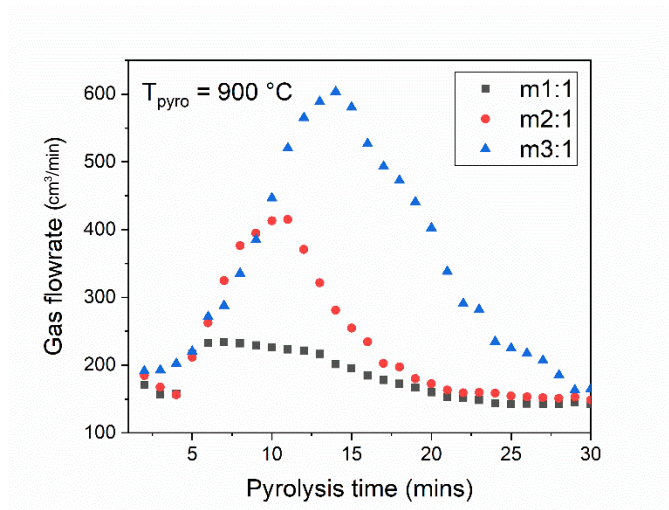
Figure 31 Gas flowrate going out from the reactor at various $m_{oil/fer}$
with T_{pyro} of 900 °C

A decrease in product yield when molar ratio of carbon precursor to ferrocene increased was also found in many studies as described previously in **section 2.4.2.1**. From Thonganantakul et al. [46], CNT yields decreased from 56.0% to 41.1% and 25.7% when molar ratio of kerosene to ferrocene increased from 1:1 to 2.2:1 and 3.3:1, respectively, at synthesis temperature of 900 °C. A decrease in product yield was obtained due to the less amount of Fe particles which was not sufficient for self-assembly of CNT at high molar ratio of kerosene to ferrocene. In addition, from Mongkolsamai et al. [41], CNT yields decreased from 9.21% to 6.68% and 4.12% when molar ratio of ethanol to ferrocene increased from 48:1 to 58:1 and 80:1, respectively, at synthesis temperature of 900 °C. At high molar ratio of ethanol to ferrocene, a high amount of carbon atoms covered surface of Fe particles resulting in the decrease in CNT growth.

The second possible reason used to explain a decrease in product yield when $m_{oil/fer}$ increased would be attributed to the presence of oxygen which would oxidize amorphous carbon [14]. A schematic diagram of the oxidizing process of carbon clusters was shown in **Figure 32**. Insufficient amount of iron particles for the growth of CNT would be resulted from the higher $m_{oil/fer}$ due to the excessive amount of carbon clusters. The amorphous carbon would react with oxygen to form CO or CO_2 [14]. As a result, the higher amount of outlet gas generated from the combination of the

oxidizing gases and gases from the decomposition of excessive carbon was confirmed as already shown in **Figure 31**. Consequently, a decrease in the amorphous carbon content in synthesized CNTs at the higher $m_{oil/fer}$ could be confirmed by FESEM, Raman, TGA, and N_2 adsorption/desorption techniques as described later. The role of oxygen which would help to oxidize amorphous carbon was reported by Ghosh et al. [14] as described in **section 2.4.1**. Use of eucalyptus oil as carbon source could improve the quality of CNTs by decreasing the amount of amorphous carbon. In the work of Ghosh et al [14]. CNTs with low amount of amorphous carbon was obtained.
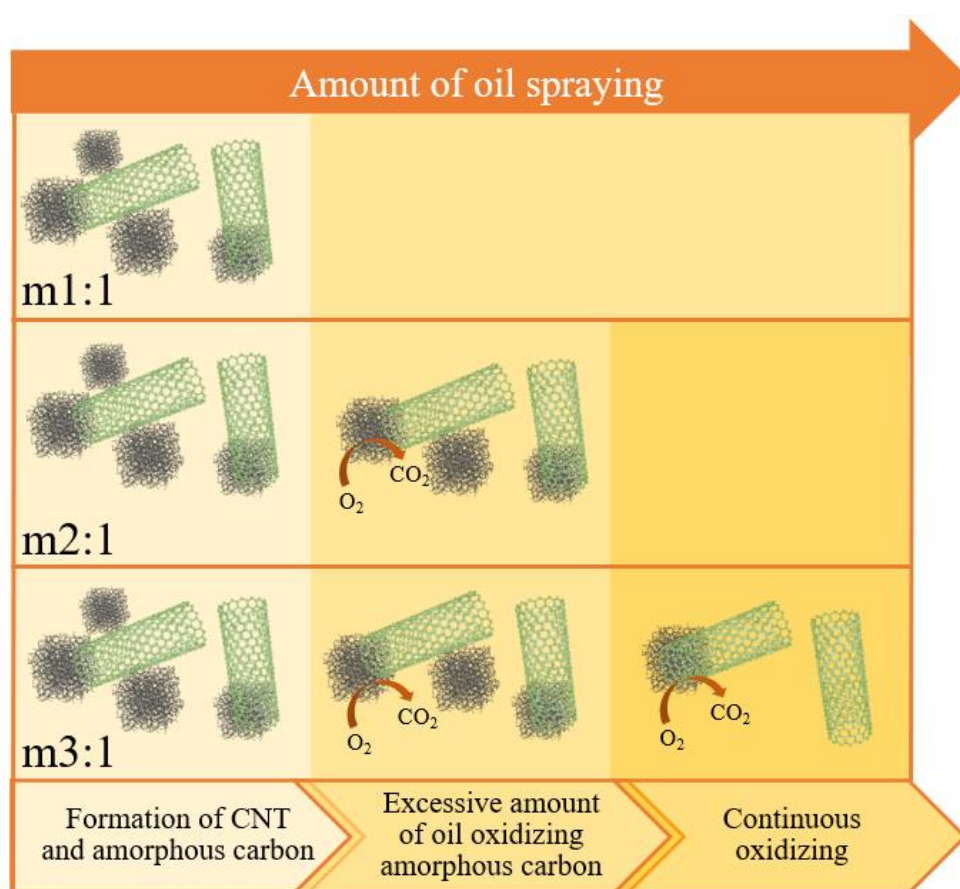
Figure 32 A schematic diagram of the oxidizing process of carbon clusters

4.1.1.1. Effect of pyrolysis temperature

The plot between product yields by weight (%) and pyrolysis temperatures (T_{pyro}) in the range of 800, 850, and 900 °C with different $m_{oil/fer}$ were shown in **Figure 33(a)**. From **Figure 33(b)**, at $m_{oil/fer}$ of 1:1, an average of the product yields raised from 41.4±6.3% to 46.8±9.0% when T_{pyro} was increased from 800 to 850 °C, respectively. From **Figure 33(c)**, at $m_{oil/fer}$ of 2:1, an average of the product yields raised from 32.7±6.3% to 40.9±3.1% when T_{pyro} was increased from 800 to 850 °C, respectively. From **Figure 33(d)**, at $m_{oil/fer}$ of 3:1, an average of the product yields raised from 21.4±6.5% to 38.3±2.5% when T_{pyro} was increased from 800 to 850 °C, respectively. The higher product yield obtained at the higher T_{pyro} would be ascribed to an increment in a decomposition rate of eucalyptus oil and ferrocene [56] which would be described later in **Figure 34**.

On the other hand, from **Figure 33(b)**, at $m_{oil/fer}$ of 1:1, an average of the product yields decreased from 46.8±9.0% to 41.7±7.6% when T_{pyro} was increased from 850 to 900 °C, respectively. From **Figure 33(c)**, at $m_{oil/fer}$ of 2:1, an average of the product yields decreased from 40.9±3.1% to 38.8±3.4% when T_{pyro} was increased from 850 to 900 °C, respectively. From **Figure 33(d)**, at $m_{oil/fer}$ of 3:1, an average of the product yields decreased from 38.3±2.5% to 36.2±4.2% when T_{pyro} was increased from 850 to 900 °C, respectively. A decrease in the product yield would be attributed to an coalescence of Fe catalysts at the higher T_{pyro} [50]. Thus, an increase in size of Fe catalysts reduced a surface area resulting in a decrease in amount of CNTs. The calculation for a decrease in surface area of Fe catalyst at the higher T_{pyro} was shown in Appendix B which can be concluded that surface area of small Fe clusters with n units combined (S_{rn}) is higher than surface area of big Fe cluster (S_R) if $n \geq 2$. In addition, an increase in diameter of synthesized CNT when T_{pyro} increased due to an increase in Fe particles was confirmed by FESEM images and size distribution of synthesized CNTs shown in **Figure 35** and **Figure 36**.
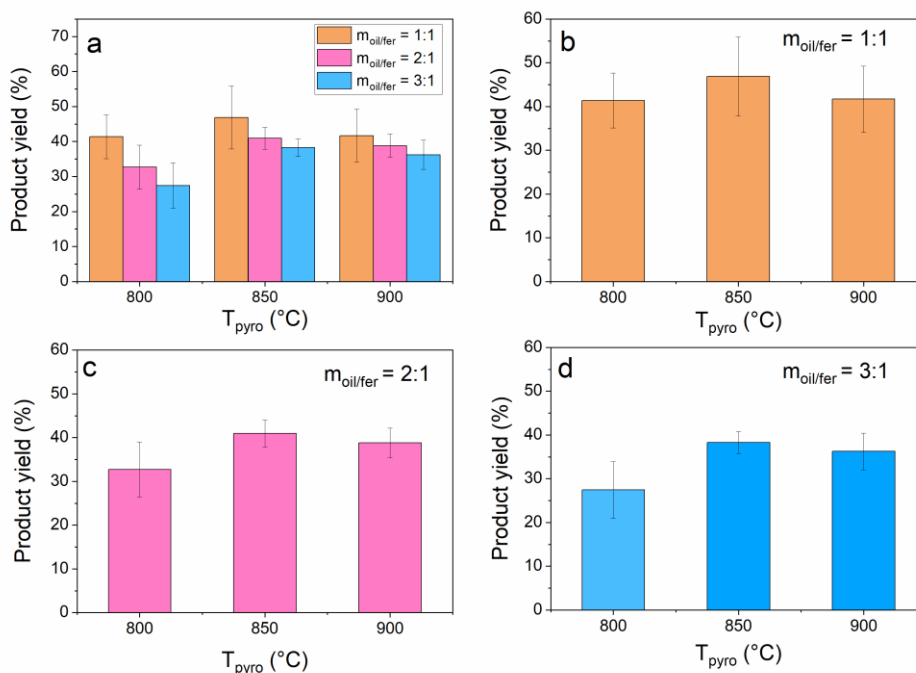
Figure 33 Product yield (%) at various T_{pyro} (a) with different $m_{oil/fer}$ and $m_{oil/fer}$ of (b) 1:1 (c) 2:1 (d) 3:1

Figure 34 showed effect of T_{pyro} with $m_{oil/fer}$ of 3:1 on product yield and gas flowrate going out from the reactor at feeding time endpoint. Gas flowrate going out from the reactor at various T_{pyro} was shown in **Table A7** in Appendix A. Feeding time endpoint at T_{pyro} was shown in **Table A1** in Appendix A. The plot indicated that the elevation of T_{pyro} from 800 °C to 850 °C could increase both product yield and gas flowrate going out from the reactor. An increase in gas flowrate going out from the reactor was evidence for the higher decomposition rate of eucalyptus oil and ferrocene. Therefore, the higher product yield was obtained. On the other hand, an increase in outlet gas at the higher decomposition rate did not elevate the product yield when T_{pyro} was increased from 850 °C to 900 °C. Thus, a decrease in the product yield could be attributed to a reduction in surface area from an agglomeration of Fe catalysts instead.
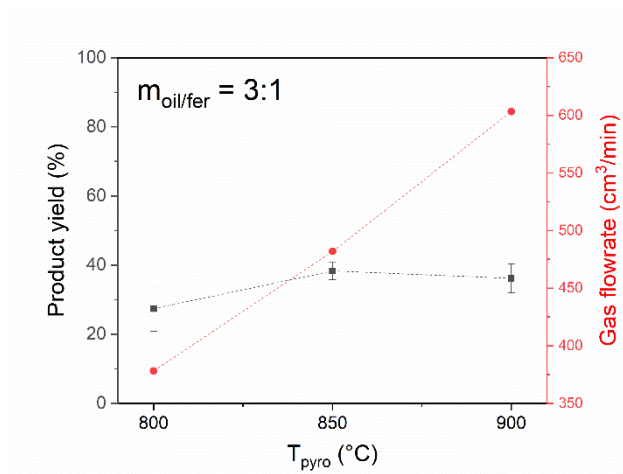
Figure 34 Effect of T_{pyro} on product yield and gas flowrate at feeding time endpoint at $m_{oil/fer}$ of 3:1

There were some studies reported about the yields of carbon products as described in **section 2.4.3.1**. From Rabbani et al. [48], yields of CNTs increased from 2.3% to 7.0% when synthesis temperature was increased from 800 °C to 850 °C due to an increase in decomposition rate of carbon precursor. However, CNT yields decreased from 7.0% to 5.8% when synthesis temperature increased from 850 °C to 950 °C due to the agglomeration of Fe particles. From Ming et al. [49], yields of CNTs increased from 210% to 278% when synthesis temperature was increased from 720 °C to 820 °C due to the higher decomposition of carbon precursor. However, CNT yields decreased from 278% to 240% when synthesis temperature increased from 820 °C to 870 °C due to the sintering of metal particles. From Li et al. [50], yields of CNTs increased from 10% to 700% when synthesis temperature from 600 °C to 900 °C due to the higher decomposition of carbon precursor and the higher dissolving rate of carbon atoms on surface of metal particles. However, CNT yields decreased from 700% to 250% when synthesis temperature increased from 900 °C to 1050 °C due to the sintering of metal particles and the presence of Fe carbide resulting in the loss of active surface of metal particles.

4.1.2   Morphology of synthesized CNTs

Figure 35 showed the morphology of synthesized CNTs at various T_{pyro} and $m_{oil/fer}$ observed from Field Emission Scanning Electron Microscope (FESEM). FESEM images revealed that when T_{pyro} and $m_{oil/fer}$ increased, the tube structure was formed in the larger amount than the disorder structure. The tube structure represented the existence of CNTs while the disorder structure represented the presence of amorphous carbon. In addition, the quality of synthesized CNTs could be interpreted from the proportion of CNT structure to amorphous carbon in each figure. From observation, higher proportion of CNT structure to amorphous carbon occurred when T_{pyro} and $m_{oil/fer}$ increased. Therefore, quality of synthesized CNTs increased when T_{pyro} and $m_{oil/fer}$ increased. The content of amorphous carbon decreased when $m_{oil/fer}$ increased due to the higher amount of oxygen content in eucalyptus oil which would help to oxidize amorphous carbon. An increase in T_{pyro} from 800 °C to 900 °C accelerated decomposition and formation rate of CNTs which showed the significant increase in CNT structure as mentioned in Ming et al. [49]. As described, the lowest T_{pyro} (800 °C) and lowest $m_{oil/fer}$ (1:1) provided the high content of amorphous carbon and low content of CNT structure or low-quality of synthesized CNTs was obtained. From **Figure 35**, the highest T_{pyro} (900 °C) and the highest $m_{oil/fer}$ (3:1) provided the low content of amorphous carbon and high content of CNT structure. Therefore, to synthesize high-quality CNTs via the co-pyrolysis of eucalyptus oil and ferrocene, T_{pyro} 900 °C and $m_{oil/fer}$ 3:1 would be the optimal conditions in this research.

Average diameter of synthesized CNT was calculated by employing ImageJ as shown in **Table 4**. The average diameter of synthesized CNT was in the range of 30-60 nm which is defined as MWCNT [57]. Size distributions of CNTs at various T_{pyro} were shown in **Figure 36(a)-(b)**. When T_{pyro} was increased from 850 °C to 900 °C, an average diameter increased from 51±6 nm and 56±6 nm, respectively. An increment of CNT diameter could confirm the agglomeration of Fe particles which were the catalysts obtained from the thermal decomposition of ferrocene at high temperature.

Table 4 Average diameters of synthesized CNTs at various $m_{oil/fer}$ and T_{pyro}

$m_{oil/fer}$	T_{pyro} (℃)	Average diameter (nm)
1:1	900	39±8
2:1	900	49±7
3:1	900	56±6
3:1	850	51±6
3:1	800	32±6

There were some studies on morphology of synthesized CNTs using FESEM as described in **section 2.4.2.2 and 2.4.3.2**. In this study, an increase in $m_{oil/fer}$ from 1:1 to 2:1 and 3:1 increased an average diameter of synthesized CNTs from 39 nm to 49 nm and 56 nm. An increase in diameter of synthesized CNTs with increasing molar ratio of carbon precursor to ferrocene had been reported by Thonganantakul et al. [46]. Their study found that CNTs which was synthesized at lowest molar ratio of kerosene to ferrocene of 1:1 exhibited the lowest average diameter of CNTs with less than 100 nm. An increase in molar ratio of kerosene to ferrocene increased an average diameter of CNTs as observed in FESEM images.

Moreover, it could be seen in **Table 4** found that, at $m_{oil/fer}$ = 3:1, an increase in T_{pyro} from 800 ℃ to 850 ℃ and 900 ℃ increased an average diameter of CNTs from 32 nm to 51 nm and 56 nm due to the agglomeration of Fe clusters. From Ming et al. [49], diameters of CNTs were 34 nm, 39 nm, 47 nm, and 52 nm when the synthesis temperature was 720 ℃, 770 ℃, 820 ℃, 870 ℃, respectively. From Li et al. [50], when the temperature increased from 650 ℃ to 800 ℃ and 1050 ℃, the diameter of CNTs increased from 13 to 23 and 65 nm. From Lee et al. [51], the diameters of CNTs were 30±5 nm, 60±10 nm, and 130±20 nm when the synthesis temperature was 750 ℃, 850 ℃, and 950 ℃, respectively. An increase in CNT diameters was obtained from an agglomeration of metal particles. In addition, Lee et al. [51] also observed the size of Fe particles. In their study, when the synthesis temperature increased from 750 ℃ to 850 ℃ and 950 ℃, the size of Fe particles increased from 40±10 nm to 90±20 nm and 150±40 nm, respectively.
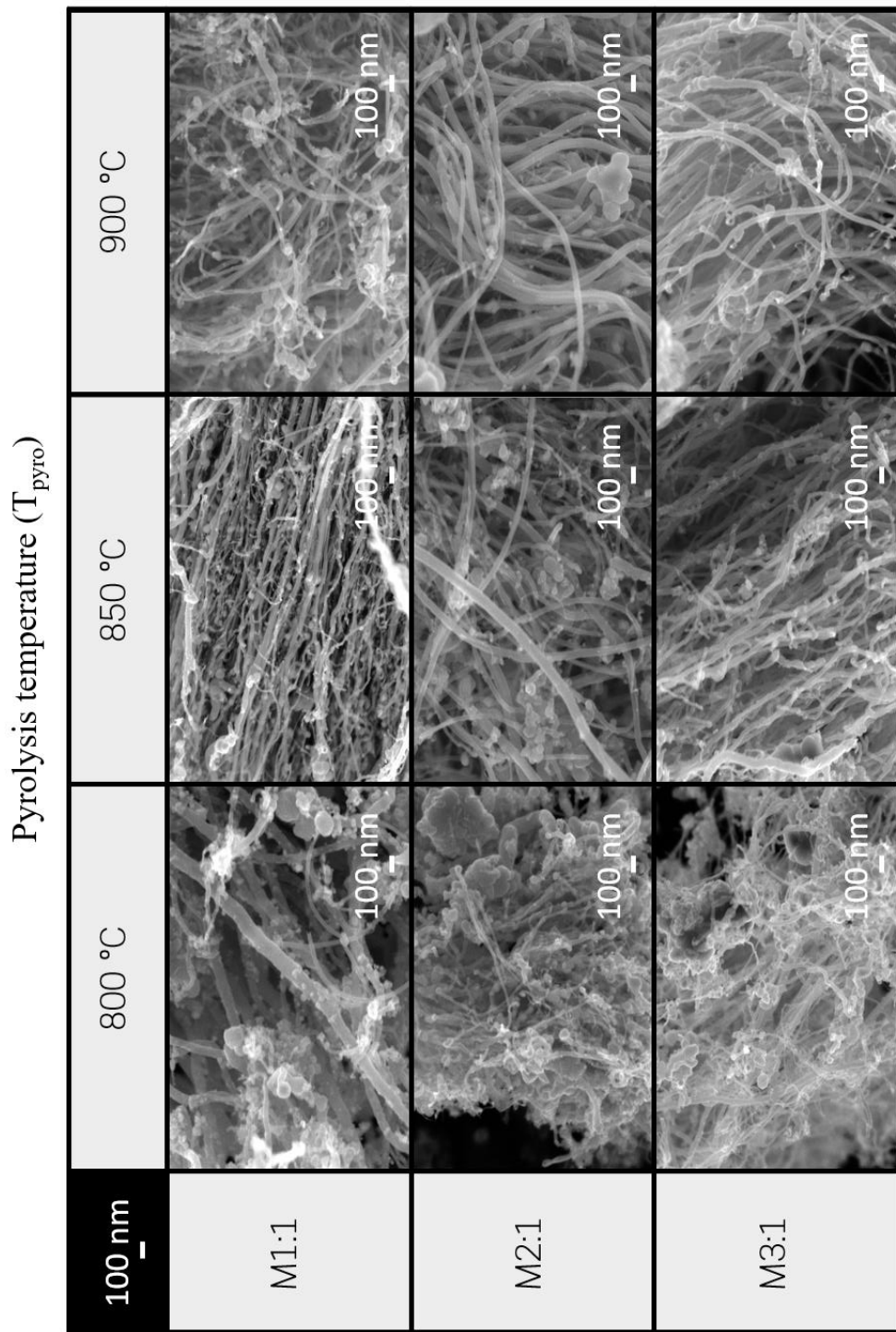
Figure 35 FESEM images of synthesized CNTs at various $m_{oil/fer}$ and T_{pyro}
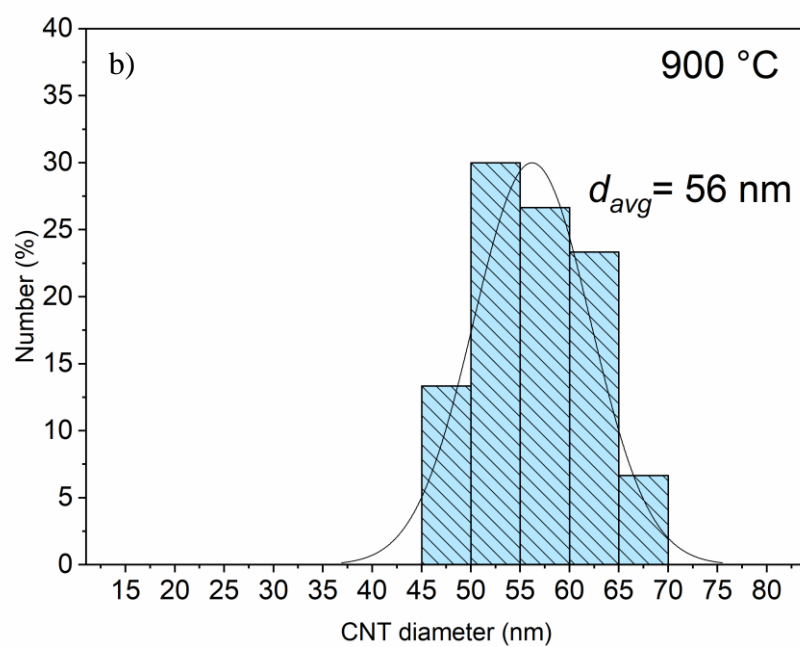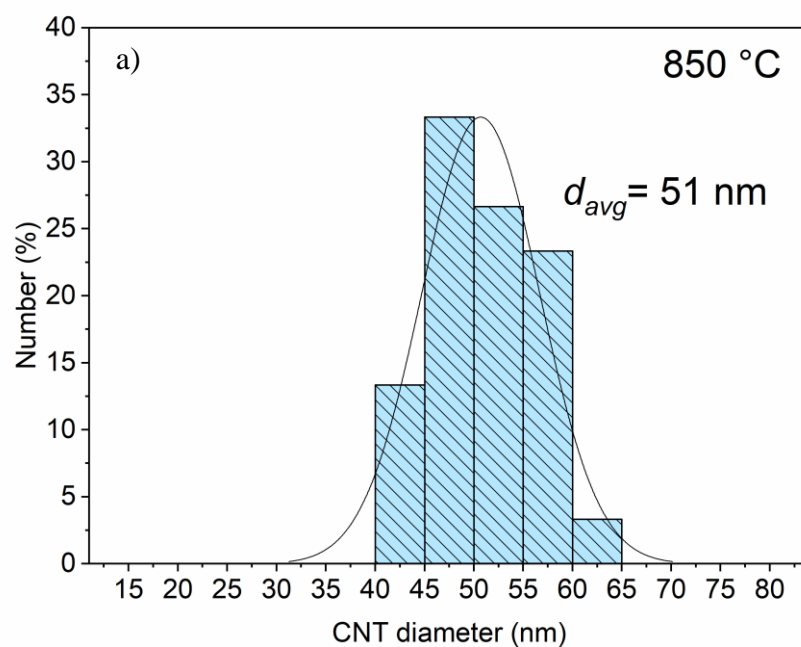
Figure 36 Size distribution of synthesized CNTs at various T_{pyro} with $m_{oil/fer}$ of 3:1 (a) 850 °C (b) 900 °C

4.1.3   Thermal stability of synthesized CNTs

The thermal stability of synthesized CNTs at various $m_{oil/fer}$ and T_{pyro} could be observed by Thermogravimetric analyzer (TGA) under O_2 atmosphere. **Figure 37(a)-(b)** exhibited TGA curves of synthesized CNTs at various $m_{oil/fer}$ and T_{pyro}. All curves were plotted between the percentage of sample weight vs. oxidation temperature. Significant weight loss at 400-600°C obtained from the decomposition of synthesized CNTs [14] and the remaining weight could be assigned to the presence of Fe oxide which was obtained from the decomposition of ferrocene in CNT synthesis [58]. **Figure 37(a)** revealed that synthesized CNTs started to decompose at temperature 432 °C to 455 °C and 460 °C when $m_{oil/fer}$ increased from 1:1 to 2:1 and 3:1 with T_{pyro} of 900 °C. Therefore, the thermal stability of synthesized CNT increased when $m_{oil/fer}$ increased because the decomposition temperature of synthesized CNTs was shifted to higher temperature. **Figure 37(b)** revealed that synthesized CNTs started to decompose at temperature 388 °C to 450 °C and 460 °C when T_{pyro} increased from 800 °C to 850 °C and 900 °C with $m_{oil/fer}$ of 3:1. Therefore, an increase in T_{pyro} also increased the thermal stability of synthesized CNTs. Thermal stability of CNTs had been reported by Lee et al. [51], when synthesis temperature increased from 750 °C to 850 °C and 950 °C weights of CNTs sample were lost at oxidation temperature 300-600 °C, 450-650 °C, and 500-670 °C, respectively. It can be concluded that CNTs had more thermal stability when the synthesis temperature increased.

From TGA curves, at the highest T_{pyro} (900 °C) and the highest $m_{oil/fer}$ (3:1) exhibited the highest thermal stability of synthesized CNTs due to the highest decomposition temperature. The highest thermal stability of CNTs which was synthesized at T_{pyro} of 900 °C and $m_{oil/fer}$ of 3:1 was obtained because synthesized CNTs at this condition had highest proportion of CNT structure and lowest amount of amorphous carbon which could be observed from FESEM image in **Figure 35**.
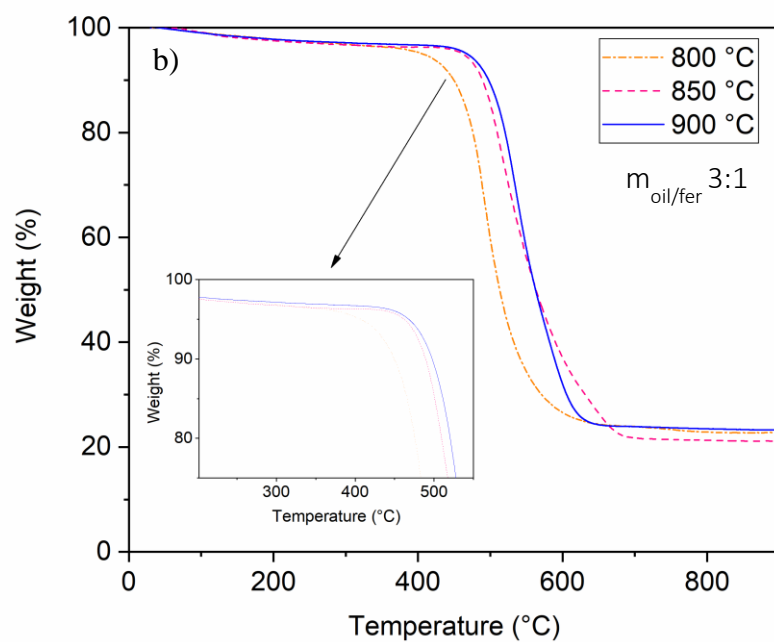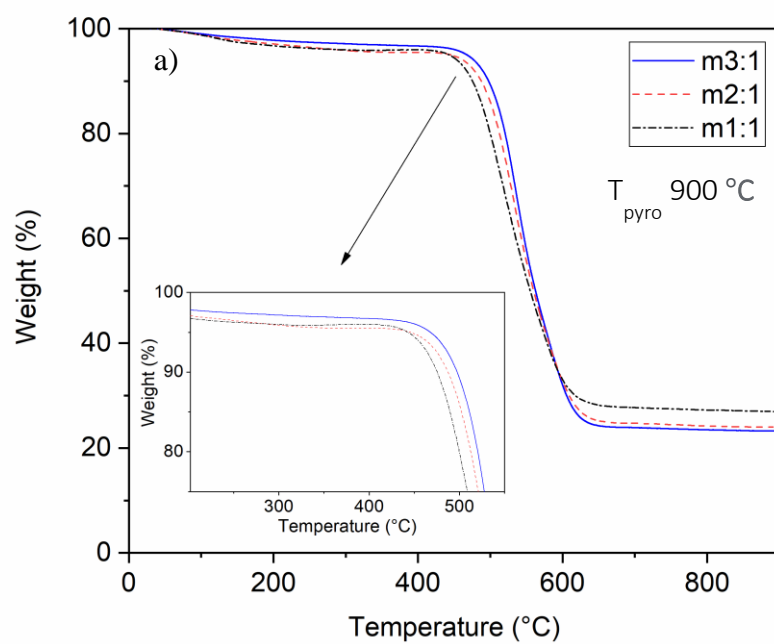
Figure 37 TGA curves of synthesized CNTs at (a) various $m_{oil/fer}$ with T_{pyro} 900 °C and (b) T_{pyro} with $m_{oil/fer}$ of 3:1

4.1.4 Crystallinity of synthesized CNTs

The graphitization/crystallinity of synthesized CNTs at various $m_{oil/fer}$ and T_{pyro} could be observed from Raman spectrum as shown in **Figure 38(a)-(b)**. A peak at Raman shift 1344 cm^{-1} could be assigned to the vibration of non-sp^2 bonded carbon atom which was called D-band. Generally, D-band was applied to identify amorphous carbon. A peak at 1576 cm^{-1} could be assigned to the vibration of sp^2 bonded carbon atom which was called G-band. Generally, G-band was applied to identify CNTs. [59]. The intensity of D-band to G-band (I_D/I_G) was used to identify the crystallinity of carbon product. The higher crystallinity of carbon product was obtained at lower I_D/I_G. From this experiment, **Figure 38(a)** indicated that I_D/I_G was decreased from 1.62 to 1.42 and 0.72 when $m_{oil/fer}$ was increased from 1:1 to 2:1 and 3:1, respectively. As revealed in **Figure 38(b)**, I_D/I_G was decreased from 1.83 to 1.60 and 0.72 when T_{pyro} was increased from 800 °C to 850 °C and 900 °C, respectively. Therefore, the crystallinity of synthesized CNTs was increased as $m_{oil/fer}$ and T_{pyro} was raised. An increase in crystallinity of CNTs obtained from an increase of CNT structure in synthesized CNTs which was also supported by the characterization results from FESEM and TGA. Therefore, high $m_{oil/fer}$ and T_{pyro} provided synthesized CNTs with high crystallinity while low $m_{oil/fer}$ and T_{pyro} provided synthesized CNTs with low crystallinity. The crystallinity of synthesized CNTs was reported by Ming et al. [49] and Lee et al. [51]. From Ming et al. [49], an increase in synthesis temperature decreased I_D/I_G. From Lee et al. [51], an increase in synthesis temperature from 750 to 950 °C decreased I_D/I_G from 1.2 to 0.8. A decrease in I_D/I_G was proportional to an increase in CNT structure in carbon product.
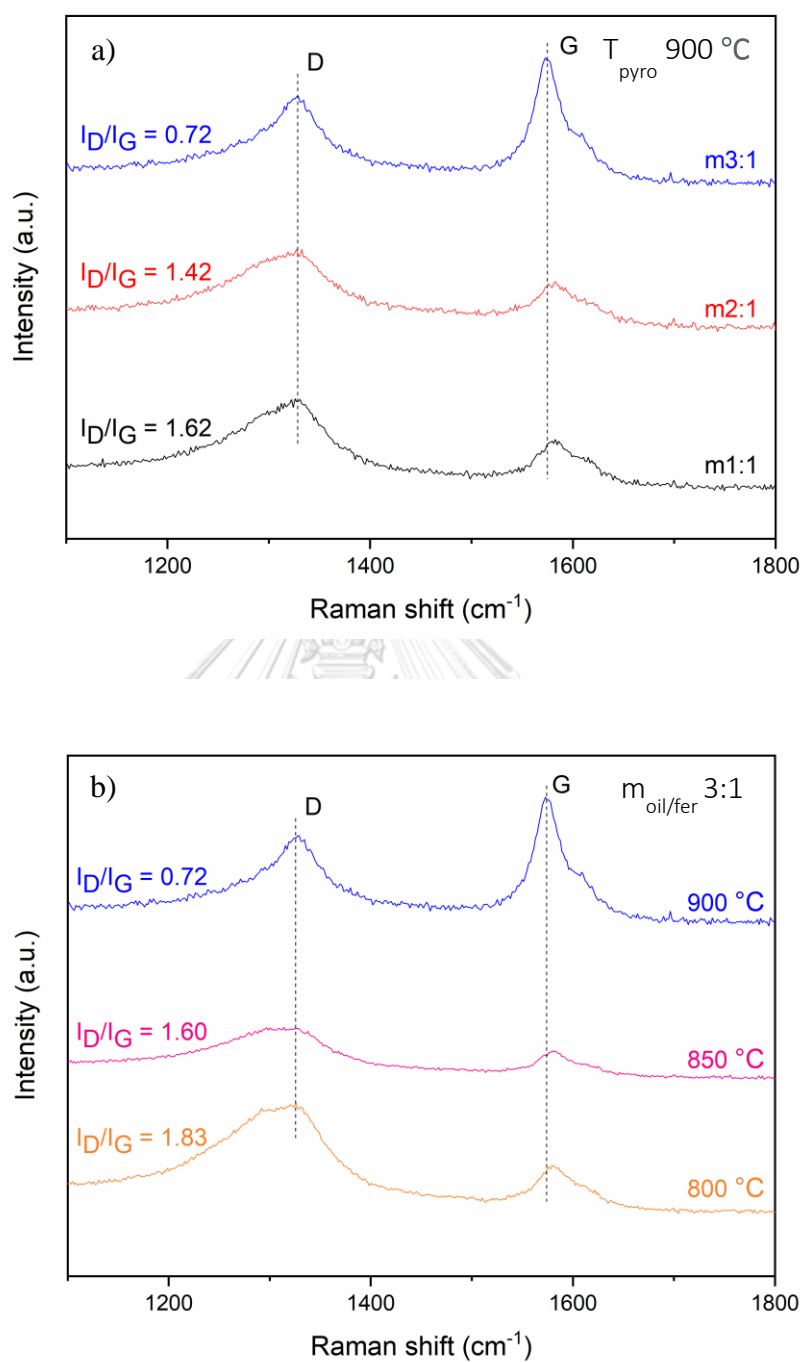
Figure 38 Comparison of I_D/I_G of synthesized CNTs at (a) various $m_{oil/fer}$ with T_{pyro} 900 °C and (b) various T_{pyro} with $m_{oil/fer}$ of 3:1

4.1.5 Surface area of synthesized CNTs

The surface area analysis of synthesized CNTs was conducted by N_2 adsorption/desorption (BET) as shown in **Table 5**. It could be observed that an increase in $m_{oil/fer}$ and T_{pyro} decreased the surface area of synthesized CNTs. The surface area of as synthesized CNTs at T_{pyro} of 800 °C decreased from 44.1±0.3 to 37.2±0.1 and 29.6±0.2 m^2/g, respectively, when $m_{oil/fer}$ increased from 1:1 to 2:1 and 3:1 due to the decrease in amorphous carbon which could be observed from FESEM images. Similarly, the surface area of synthesized CNTs at T_{pyro} of 850 °C decreased from 38.9±0.3 to 29.7±0.3 and 22.5±0.2 m^2/g when $m_{oil/fer}$ increased from 1:1 to 2:1 and 3:1, respectively, while the surface area of synthesized CNTs at T_{pyro} of 900 °C decreased from 28.1±0.1 to 25.8±0.1 and 21.6±0.2 m^2/g when $m_{oil/fer}$ increased from 1:1 to 2:1 and 3:1, respectively. A decrease in the surface area when $m_{oil/fer}$ and T_{pyro} increased could be attributed to an increase in the proportion of CNTs to amorphous carbon in carbon products which CNTs had low porosity than amorphous carbon [60, 61]. Therefore, it can be concluded that low $m_{oil/fer}$ (1:1) and low T_{pyro} (800 °C) provided the high surface area of CNTs while high $m_{oil/fer}$ (3:1) and high T_{pyro} (900 °C) provided the low surface area of CNTs. As confirmed by FESEM, TGA, and Raman spectroscopy, a decrease in surface area could be assigned to the lower amount of amorphous carbon. Hence, TGA revealed that high $m_{oil/fer}$ and T_{pyro} provided synthesized CNTs with high thermal stability owing to its highest content of CNT structure. In addition, Raman spectroscopy showed the lower I_D/I_G indicating that CNTs synthesized at high $m_{oil/fer}$ and T_{pyro} had high crystallinity.

Table 5 Surface area (m^2/g) of synthesized CNTs at various $m_{oil/fer}$ and T_{pyro}

BET surface area (m^2/g)				
Variable parameters		T_{pyro}		
		800 °C	850 °C	900 °C
$m_{oil/fer}$	m1:1	44.1±0.3	38.9±0.3	28.1±0.1
	m2:1	37.2±0.1	29.7±0.3	25.8±0.1
	m3:1	29.6±0.2	22.5±0.2	21.6±0.2

4.1.6 Summary of all characterizations of synthesized CNTs

Eucalyptus oil is one of the promising alternative natural carbon sources to produce CNTs via co-pyrolysis with ferrocene. This research focused on the study of the effects of $m_{oil/fer}$ and T_{pyro} on CNT properties using various techniques to characterize the characteristic of synthesized CNTs. The results revealed that high $m_{oil/fer}$ and high T_{pyro} provided good-quality CNTs with high thermal stability and high crystallinity. Therefore, in order to employ CNTs in CO_2 methanation, which was an exothermic reaction, synthesized CNT at $m_{oil/fer}$ of 3:1 and T_{pyro} of 900 °C was the optimal conditions for the preparation of catalyst support material.

4.2 Performance test in methanation

Synthesized CNTs at $m_{oil/fer}$ of 3:1 and T_{pyro} of 900 °C was used as a catalyst support material in CO_2 methanation. Ni-Fe was impregnated onto the support at 30 wt% metal loading with different Ni-Fe weight ratio (1:0, 3:1, 1:1, 1:3, and 0:1). The calculation of weight percentage of metal loading was shown in **Appendix D**. Then, Ni-Fe/CNT catalysts were calcined at different calcination temperatures (250 °C, 300 °C, 350 °C, 400 °C) for 3 h. After that, 0.1 g of calcined Ni-Fe/CNT catalysts were reduced with H_2 at 500 °C and were employed in the reaction at 325 °C for 20 min. The performance of Ni-Fe/CNT catalysts were evaluated and discussed based on CO_2 conversion, CH_4 selectivity and CH_4 yield.

4.2.1   Effect of calcination temperature on performance of catalyst

CO_2 conversion (%X_{CO2}), CH_4 selectivity (%S_{CH4}) and CH_4 yield (%Y_{CH4}) of 30 wt% Ni/CNT were shown in **Table 6**. It was worth noting that that an increase in calcination temperature within the range from 250 °C to 350 °C could enhance CO_2 conversion, CH_4 selectivity and CH_4 yield. As observed from the results, the highest CO_2 conversion with 38% was obtained from 30 wt% Ni/CNT at calcination temperature of 350 °C. When calcination temperature was increased from 250 °C to 350 °C, CO_2 conversion increased from 20% to 38 %, CH_4 selectivity increased from 85% to 96%, and CH_4 yield increased from 17% to 36%, respectively. An increase in catalyst performance was obtained from the completion of calcination to change metal nitrate to metal oxide at calcined temperature higher than 300 °C [62]. However, further increase in calcination temperature from 350°C to 400°C reduced the catalyst activity, resulting in the decrease of CO_2 conversion from 38% to 15%, CH_4 selectivity from 96% to 85%, and CH_4 yield from 36% to 13%, which could be due to the decomposition of carbon support and the agglomeration of metal particles at high calcination temperature [63].

Table 6 Effect of calcination temperature of 30 wt% Ni/CNT on %X_{CO2}, %S_{CH4}, and %Y_{CH4} at reaction temperature 325 °C

Sample	Calcination temperature (°C)	%X_{CO2} (%)	%S_{CH4} (%)	%Y_{CH4} (%)
30%Ni/CNT-T250	250	20	85	17
30%Ni/CNT-T300	300	34	94	32
30%Ni/CNT-T350	350	38	96	36
30%Ni/CNT-T400	400	15	85	13

The reducibility of 30 wt% Ni/CNT was characterized by H_2-TPR as shown in **Figure 39**. There were 2 main peaks (α and β) exhibiting the reduction of Ni^{2+} to Ni^0 [64]. The first reduction peak could be assigned to the weak nickel-carbon interaction. The second reduction peak could be assigned to the strong nickel-carbon interaction. This result indicated that when calcination temperatures were varied from 250 °C to 400 °C, the first peaks correspondingly shifted from 257.3 °C to 302.5°C and the second peak also shifted from 544.9 to 567.3°C. Therefore, an increase in calcination temperature shifted these two peaks to higher temperature, indicating that the interaction between metal and support became stronger. In addition, the peak area shown in **Table 7** could be used to interpret the H_2-consumption for the reduction of Ni^{2+} to Ni^0. Higher H_2-consumption referred to the higher reducibility of catalyst. When calcination temperature was raised from 250 °C to 300 °C and 350 °C, the peak area increased from 823.5, 825.4, and 859.8 a.u., respectively. However, when calcination temperature was further raised from 350 °C to 400 °C, the peak area started to decrease from 859.8 to 791.3 a.u. The results indicated that the catalyst calcined at 350 °C could be reduced easier than catalyst from other calcination temperature. Hence, based on H_2-consumption result, 350 °C would be the optimal calcination temperature.
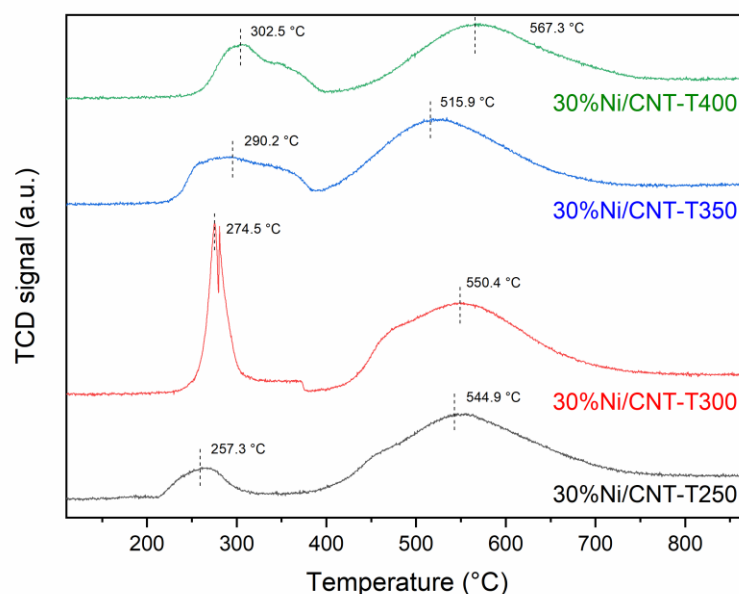
Figure 39 H$_2$-TPR results of 30 wt% Ni/CNT at various calcination temperatures

Table 7 H$_2$ consumption of 30 wt% Ni/CNT at various calcination temperatures

Catalysts	H$_2$ consumption area (a.u.)		Total H$_2$ consumption (a.u.)
	α	β	
30%Ni/CNT-T250	101.2	733.3	823.5
30%Ni/CNT-T300	213.9	611.5	825.4
30%Ni/CNT-T350	246.8	613.1	859.8
30%Ni/CNT-T400	229.0	562.3	791.3

Figure 40 showed the diffraction peaks of calcined catalysts at various calcination temperatures. Crystallinity peaks at 37.1°, 43.0°, 62.7°, 75.4° were attributed to NiO phase corresponded to (111), (200), (220), and (311) planes [65]. The diffraction peaks at 33.0°, 35.6°, and 54.12° reflected from Fe$_2$O$_3$ phase (104), (110), and (116) [66]. In addition, the peaks of α-Fe and graphite were obtained from CNT synthesis. The diffraction peaks at 44.5° corresponded to α-Fe (110) plane [67]. The

diffraction peaks at 26.3° corresponded to graphite (002) plane [68]. The diffraction peaks at 43.5° represented to Fe_3Ni_2 (225) plane [69]. The enhancement of calcination temperature from 250 °C to 400 °C decreased the crystallinity of CNTs in catalysts due to the oxidation of CNTs [63]. The Scheler equation was then applied to calculate the crystallite size of metal. When calcination temperature raised from 250 to 400 °C, NiO crystallite size increased from 0.3 nm to 0.6 nm, 0.6 nm, and 3.8 nm, respectively. An increase in NiO particle size obtained from the sintering of metal at high temperature. In addition, NiO particle size was significantly increased from 0.6 nm to 3.8 nm when calcination temperature was raised from 350 °C to 400 °C. At 400 °C, higher oxidation degree of CNTs was observed from the decrease in weight of samples after calcination with 50 wt% loss compared with 36 wt% loss of weight of catalyst when calcined at 350 °C.
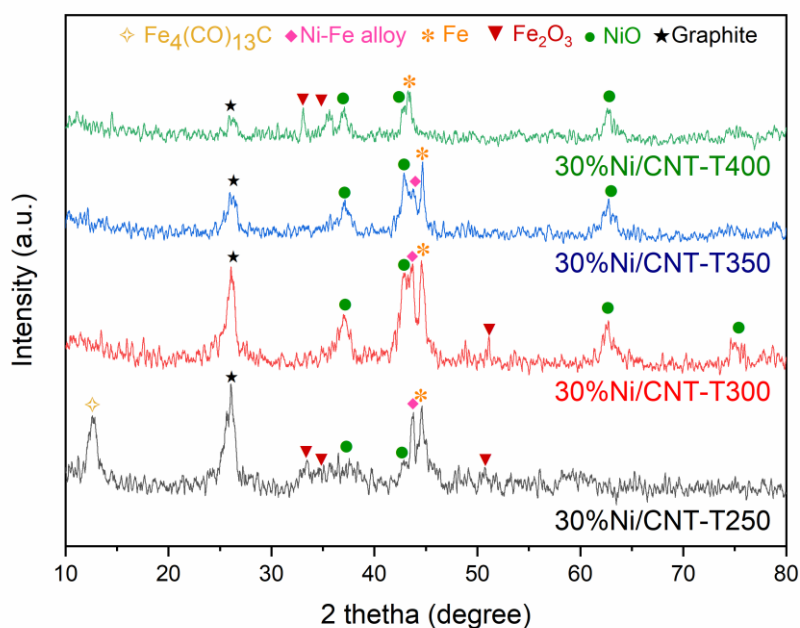
Figure 40 XRD pattern of 30 wt% Ni/CNT at various calcination temperatures

4.2.2   Effect of Ni to Fe weight ratio on performance of catalyst

CO_2 conversion ($\%X_{CO2}$), CH_4 selectivity ($\%S_{CH4}$) and CH_4 yield ($\%Y_{CH4}$) of 30 wt% Ni-Fe/CNT were shown in **Table 8**. As observed from these results, an increment in weight ratio of Ni to Fe enhanced CO_2 conversion, CH_4 selectivity and CH_4 yield. When weight ratio of Ni to Fe was increased from 0:1 to 1:0, CO_2 conversion increased from 4% to 38%, CH_4 selectivity increased from 6% to 95%, and CH_4 yield was increased from 0.2% to 36%, respectively. In addition, catalyst performance in CO_2 methanation could be indicated by observing the change in catalyst temperature.

An increase in Fe content led to an increment in water-gas shift reaction (WGS) which converted CO as an intermediate in this reaction to CO_2 [70]. Thus, CO_2 conversion reduced when weight of Fe was increased due to the higher production of CO_2. In addition, an increase in Fe content could limit CO adsorption onto the surface of catalyst which was the intermediate in CO_2 methanation [71]. Therefore, CO was desorbed from the catalyst surface before reducing to CH_4 leading to a decrease on CH_4 selectivity.

Table 8 Effect of Ni to Fe weight ratio of 30 wt% Ni-Fe/CNT on $\%X_{CO2}$, $\%S_{CH4}$, $\%Y_{CH4}$ at reaction temperature 325 °C

Catalysts	Ni to Fe weight ratio	$\%X_{CO2}$ (%)	$\%S_{CH4}$ (%)	$\%Y_{CH4}$ (%)
30%Ni/CNT	1:0	38	95	36
30%Ni$_{75}$Fe$_{25}$/CNT	3:1	24	93	22
30%Ni$_{50}$Fe$_{50}$/CNT	1:1	6	25	2
30%Ni$_{25}$Fe$_{75}$/CNT	1:3	4	23	1
30% Fe/CNT	0:1	4	6	0.2

Figure 41 indicated H_2-TPR results of 30 wt% Ni-Fe/CNT at various weight ratio of Ni-Fe. The sample of 30 wt% Fe without Ni addition exhibited 3 main peaks. The first reduction peak (α) at 321.9 °C could be assigned to the weak iron-carbon

interaction. The second reduction peaks (β) at 437.8 °C could be assigned to the medium iron-carbon interaction. The reduction peak (γ) at 637.7 °C referred to the strong iron-carbon interaction [72]. The 30 wt% Ni/CNT sample consisted of 2 main peaks (α and β) which were the reduction of Ni^{2+} to Ni^0 at weak and strong interaction of Ni onto the supporting material, respectively. The sample of 30 wt% Ni-Fe/CNT exhibited similar H_2-TPR profile to 30 wt% Ni/CNT which consisted of 2 peaks. The first reduction peak (α) at 284.2 to 316.4 °C could be assigned to the low metal-carbon interaction while the second reduction peaks (β) at 539.5 to 566.2 °C could be assigned to high metal-carbon interaction [64]. An increase in Fe content also shifted the reduction peaks to higher temperature. This result indicated that an addition of Fe could made the interaction of metal-carbon support become stronger [73]. Consequently, catalyst could be more difficult to be reduced with this stronger interaction. In addition, **Table 9** revealed the decrease of H_2 consumption when the iron content was raised. Therefore, the sample of 30 wt% Ni/CNT without Fe addition could be reduced easier than other catalysts.
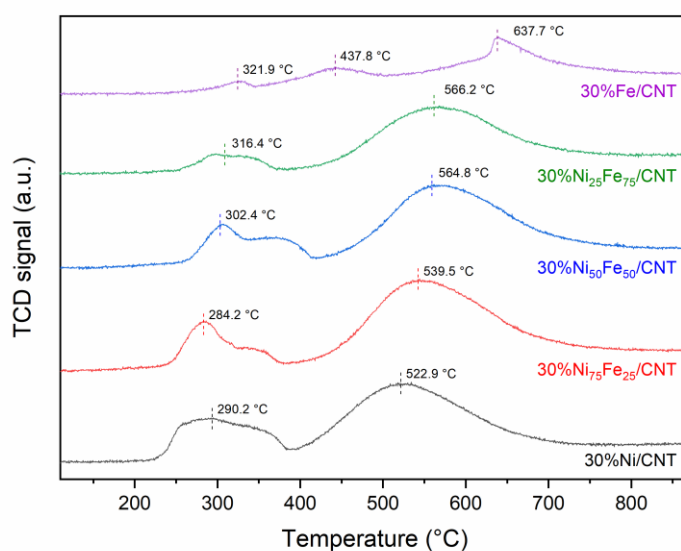
Figure 41 H_2-TPR results of 30 wt% Ni-Fe/CNT at various weight ratio of Ni to Fe

Table 9 H_2 consumption of 30 wt% Ni-Fe/CNT at various weight ratio of Ni to Fe

Catalysts	H_2 consumption area (a.u.)			Total H_2 consumption (a.u.)
	α	β	γ	
30%Ni/CNT	246.8	613.1	-	859.8
30%Ni$_{75}$Fe$_{25}$/CNT	198.0	655.2	-	853.2
30%Ni$_{50}$Fe$_{50}$/CNT	193.3	653.3	-	846.6
30%Ni$_{25}$Fe$_{75}$/CNT	69.3	539.0	-	608.3
30%Fe/CNT	20.4	64.7	208.5	293.6

Figure 42 presented XRD pattern of the calcined 30 wt% Ni-Fe/CNT catalysts after calcination in air at 350 °C for 3 h. The catalysts showed oxide forms of NiO and Fe_2O_3 which were obtained from the calcination under air flow. The diffraction peaks at 37.1°, 43.0°, 62.7° were attributed to NiO phase corresponding to (111), (200), and (220) planes [65]. The diffraction peaks at 33.0°, 35.6°, 49.7°, 54.12°, 62.3°, and 64.1° corresponded to (104), (110), (024), (116), (214) and (030) planes [66]. In addition, the peaks of α-Fe, graphite, and Ni-Fe alloy were obtained from CNT synthesis. The diffraction peak at 44.5° corresponded to α-Fe (110) plane [67]. The diffraction peak at 26.3° corresponded to graphite (002) plane [68]. The diffraction peak at 43.5° corresponded to Ni-Fe alloy or Fe_3Ni_2 (225) plane [69]. **Figure 42** revealed that an increment in Fe content decreased the intensity of NiO peaks and exhibited Fe_2O_3 peaks instead [74]. Therefore, XRD results could confirm a decrease in NiO when the weight percentage of Fe was increased leading to the decrease in CO_2 conversion, while an increase of Fe_2O_3 leading to the decrease in CH_4 selectivity.

Moreover, Scheler equation was applied to calculate the crystallite size of NiO at position with the highest intensity. The result showed that an addition of Fe content from 0 to 1 weight ratio of Fe to Ni decreased the crystallite size of NiO in the order 0.7, 0.5, 0.5, and 0.2 nm. A decrease in crystallite size of Ni enhanced the metal-support interaction due to the increase in surface area of Ni. This result also confirmed the reducibility which was shown in H_2-TPR results above. Thus, 30 wt% Ni-Fe/CNT

catalyst with high content of Fe could be more difficult to be reduced than low content of Fe, resulting in a decrease in catalyst performance.
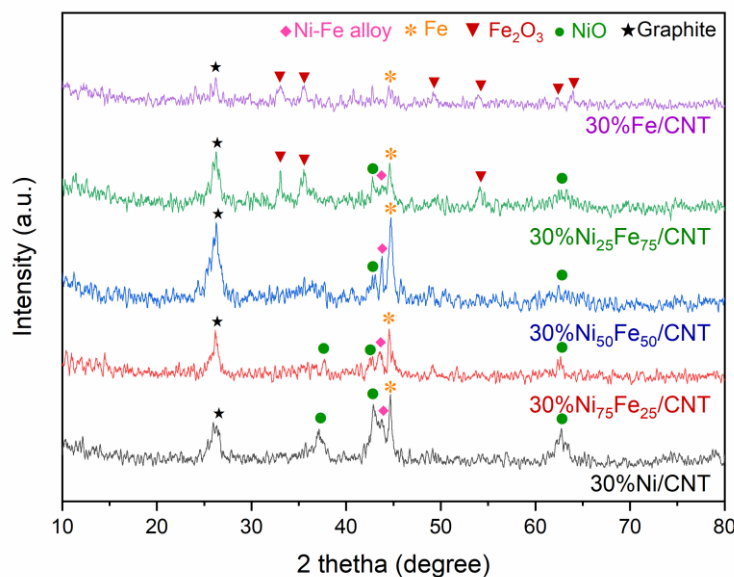
Figure 42 XRD pattern of 30 wt% Ni-Fe/CNT at various weight ratio of Ni to Fe

Table 10 showed the comparison of CO_2 conversion of 30 wt% Ni loading on various support. 30%Ni/CNT represented the 30 wt% Ni loading onto synthesized CNTs which was synthesized from co-pyrolysis of eucalyptus oil and ferrocene at $m_{oil/fer}$ 3:1 and T_{pyro} 900 °C. Actual weight ratio of Ni to Fe impregnated on synthesized CNTs was also shown in **Appendix E** which was analyzed by EDX. From EDX results, an actual weight ratio of Ni to Fe was determined to be 70:30. The presence of Fe could be attributed to the inherited Fe from CNT synthesis. In order to get more understanding about the effect of Ni-Fe on CO_2 methanation, 30%Ni/CNT-A could be prepared from impregnation of 30 wt% Ni onto CNTs after treated with acid. Acid treatment of synthesized CNTs was conducted following Hu et al. [75] to reduce Fe content in CNT structure. EDX results indicated that Fe could be removed from CNT structure after treatment which left only 3.8 wt% Fe remaining. A decrease of Fe in 30%Ni/CNT-A reduced CO_2 conversion to 34% although surface area of CNT-A became a little bit higher than synthesized CNTs.

Table 10 Effect of various CNT support materials of 30 wt% Ni/CNT on CO_2 conversion at reaction temperature 325 °C

Catalysts	S_{BET} (m^2/g)	%X_{CO2} (%)
30%Ni/CNT	21.6	38
30%Ni/CNT-A	25.2	34
30%Ni/CNT-C	217.3	43

Figure 43 showed XRD pattern of 30 wt% Ni impregnated on CNTs before (CNT) and after (CNT-A) acid treatment. It could be observed that the NiO peak at 37.1° of 30 wt% Ni/CNT was broader than NiO peak of 30 wt% Ni/CNT-A indicating smaller crystalline size of NiO. The exact value of crystallite size of NiO was calculated by Scheler equation. It could be confirmed that NiO size of 30 wt% Ni/CNT of about 0.64 nm was smaller than 30 wt% Ni/CNT-A which was 0.94 nm. Hence, the smaller crystallite size of NiO could result in higher reducibility of catalyst due to the enhancement in metal dispersion. The reducibility of catalysts could be analyzed by H_2-TPR results shown in **Figure 44**.
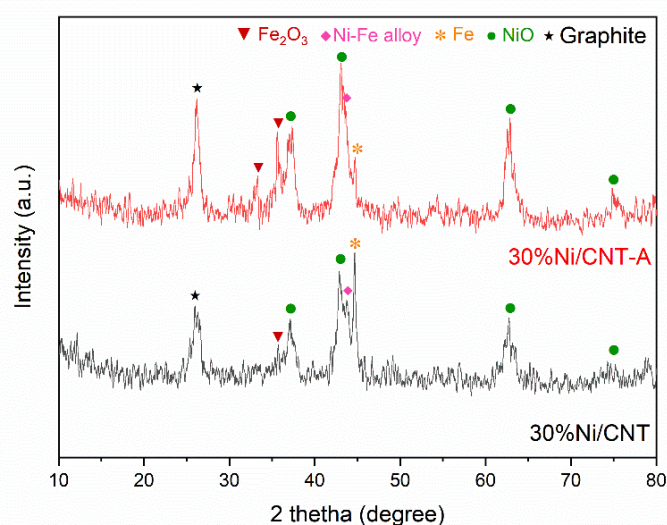
Figure 43 XRD pattern of 30 wt% Ni/CNT at various CNT support materials

Figure 44 showed the reducibility of catalyst which was obtained from H_2-TPR results. The reduction peak of 30 wt% Ni/CNT-A at 842.7 a.u. was shifted to higher temperature. In addition, H_2 consumption of 30%Ni/CNT-A was lower than 859.8 a.u. of 30%Ni/CNT as shown in **Table 11**. Thus, 30%Ni/CNT-A was more difficult to reduce than 30%Ni/CNT.
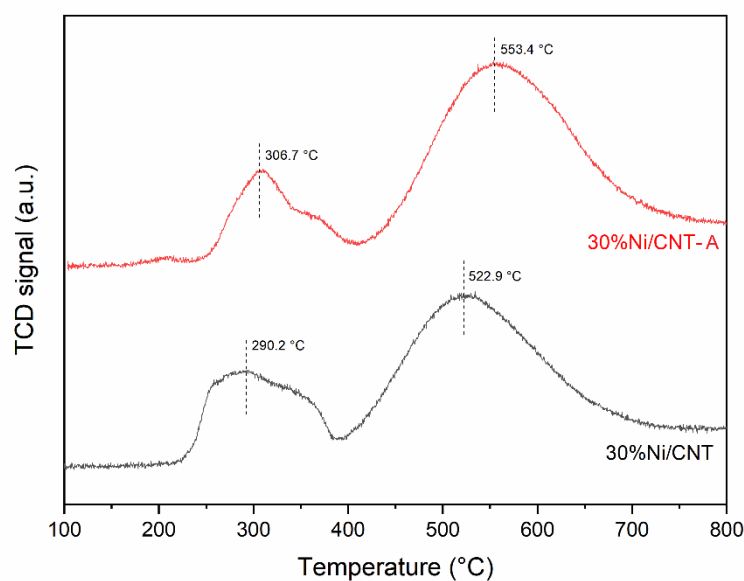
Figure 44 H_2-TPR results of 30 wt% Ni/CNT at various CNT support materials

Table 11 H_2 consumption of 30 wt% Ni/CNT at various CNT support materials

Catalysts	H_2 consumption area (a.u.)			Total H_2 consumption (a.u.)
	α	β	γ	
30%Ni/CNT	246.8	613.1	-	859.8
30%Ni/CNT-A	169.7	673.0	-	842.7

The higher catalyst activity when Fe was applied in Ni based catalyst was reported by Meshkini et al. [76]. They suggested that at Ni to Fe weight ratio in the range of 70 to 90 wt% onto γ-Al_2O_3 enhanced the CO_2 conversion and CH_4 selectivity due to the increment in CH_4 formation pathway in CO_2 methanation. On the other hand, Pendey et al. [77] and Meshkini et al. [76] reported that an increase in weight ratio of

Fe higher than 50 wt% significantly decreased catalyst activity due to an enhancement in CO formation and a presence of WGS reaction [76, 77].

In addition, **Table 10** defined 30 wt% Ni/CNT-C as the 30 wt% Ni loading onto commercial CNTs. The 30%Ni/CNT-C provided the higher CO_2 conversion of about 43%. However, an increment in CO_2 conversion could be obtained from the higher surface area of CNTs. Under CO_2 conversion by considering surface area of CNTs, it could be interpreted that it is unnecessary to purify synthesized CNTs.

Figure 45 showed FESEM image of 30 wt% Ni/CNT which was prepared by impregnation method. As observed in this figure, metal particles distributed and covered CNT surface. In addition, the dispersion of Ni could be observed from mapping that there is uniform dispersion of Ni particles while the existence of inherited Fe which was obtained from CNT synthesis could be also confirmed by EDX mapping.
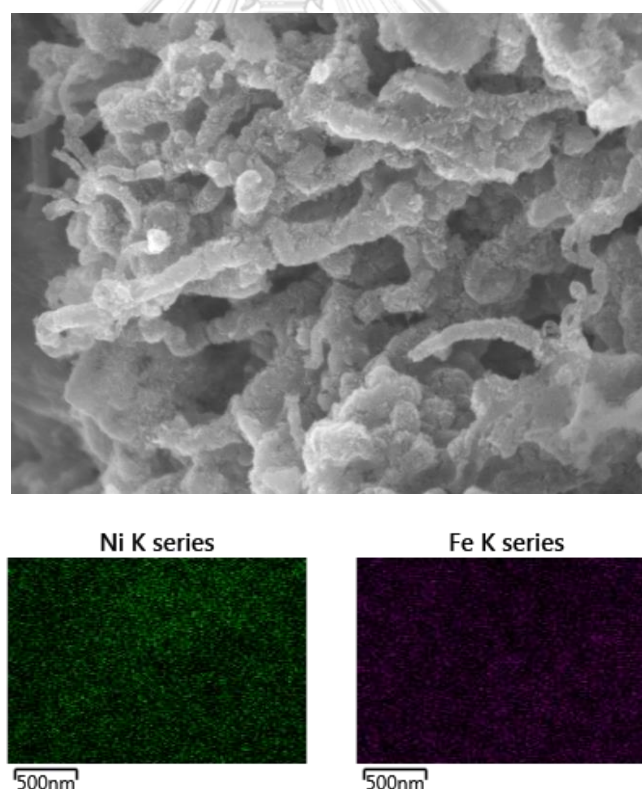
Figure 45 FESEM image and EDX mapping of 30 wt% Ni/CNT

CHAPTER 5
CONCLUSION AND RECOMMENDATION

This chapter provided a summary of key findings in this study. This research work comprised two main investigations: (i) the study of synthesis of carbon nanotubes by co-pyrolysis of eucalyptus oil and ferrocene, and (ii) the utilization of carbon nanotubes as catalyst support for CO_2 conversion into CH_4, focusing on an investigation of bimetallic catalyst, consisting of nickel and iron. Lastly, some useful suggestions obtained during the study were provided for guiding a further investigation.

5.1   Conclusion

5.1.1   CNT synthesis

Carbon nanotubes have been of great interest due to their promising properties for a wide range of industrial applications. For example, CNTs possess a high specific surface area and remain chemically inert which are favored for utilizing as a catalyst support, dispersing active metal but not-involving in a reaction. Additionally, the high thermal conductivity of CNTs due to can potentially provide an excellent heat transfer, especially for highly exothermic reaction such as CO_2 methanation. This can help alleviate a suffering from a catalyst deactivation in a mode of metal sintering. Fortunately, a production method of CNTs is considered to be simple, and many synthesis methods are available, such as arc discharge, electrochemical, and pyrolysis. However, a proper control of synthesis parameter is required to produce a high homogeneity of CNTs with high quality such as uniform tube and high graphitic carbon with respect to amorphous carbon. In this study, a pyrolysis was selected due to a potential for large scale production, while renewable carbon source like eucalyptus oil was employed together with ferrocene as a widely-used catalyst for CNT formation. Then the essential synthesis parameters including (i) molar ratio of eucalyptus oil and ferrocene ($m_{oil/fer}$), and (ii) pyrolysis temperature (T_{pyro}) were investigated. The influence of T_{pyro} was examined at three points of temperature including 800 °C, 850 °C, and 900 °C. The temperature range and interval were carefully selected according to general knowledge from the prior arts. Meanwhile, the $m_{oil/fer}$ was simply varied at

three ratios which are 1:1, 2:1, and 3:1 in order to directly observe the influence of increased carbon source. In the synthesis, the ferrocene was vaporized and carried into the reaction zone by N_2 carrier gas. Subsequently, the oil was fed into the reactor. CNTs were formed and deposited at wall of reactor. The oil is fed at a constant rate. Therefore, the $m_{oil/fer}$ was a ratio of the total oil fed with respect to the initial amount of ferrocene. In other words, the $m_{oil/fer}$ was varied by changing the total feed time at constant feed rate. The deposit carbon was carefully collected and weighted in order to determine the product yield of the process. In addition, the flow rate of gas outlet was recorded to understand the behavior during the pyrolysis.

It was found that product yield was distinctly affected by pyrolysis parameter such as $m_{oil/fer}$ and T_{pyro}. An increase in $m_{oil/fer}$ decreased product yield of CNTs due to the less amount of Fe particles were available and the decomposition of amorphous carbon was raised by the higher oxygen content because of the higher $m_{oil/fer}$. The effect of T_{pyro} could be explained in two synthesis temperature ranges: an increase in T_{pyro} from 800 to 850 °C raised the product yield due to an enhancement in the decomposition of carbon precursor which was observed from an increase in flow rate of gas outlet. On the other hand, an increase in T_{pyro} from 850 to 900 °C decreased the product yield due to an agglomeration of Fe clusters which reduced surface area of Fe catalysts for CNT growth.

In order to elucidate a relationship between the properties of CNTs and the synthesis parameters, various characterization techniques including FESEM, Raman, TGA, and N_2 adsorption/desorption were used to examine the properties of CNTs such as morphology, crystallinity, thermal stability, and surface area. It was found that the proportion of CNTs to amorphous carbon in carbon products increased when $m_{oil/fer}$ and T_{pyro} increased which was observed from FE-SEM, Raman spectroscopy, TGA, and N_2 adsorption/desorption. Consequently, samples with more CNT structure also showed the high crystallinity, high thermal stability, and low surface area which demonstrated their potential to be a catalyst support for CO_2 methanation. In conclusion, the synthesized CNTs at $m_{oil/fer}$ 3:1 and T_{pyro} 900 °C was selected as a support material in CO_2 methanation owing to its high thermal stability and good quality CNTs.

5.1.2 CO_2 methanation

CO_2 methanation was performed in order to the aim for reducing the concentration of CO_2 in the atmosphere. Heterogeneous catalyst has been developed to convert CO_2 into CH_4 where CH_4 could be used as a fuel in many industries. Ni-based catalyst was one of the popular catalysts used in CO_2 methanation because it had high selectivity and low-cost. However, Ni-based catalyst had low activity and easily deactivated. Therefore, bimetallic Ni-Fe system has been developed to improve the activity and catalyst performance. In this study, the two important parameters including (i) calcination temperature and (ii) weight ratio of Ni-Fe on CNTs were investigated. Calcination temperature was examined at 4 points including 250 °C, 300 °C, 350 °C, and 400 °C. Meanwhile, weight ratio of Ni-Fe was varied at 5 points including 1:0, 3:1, 1:1, 1:3, and 0:1. In the catalyst preparation, CNTs were impregnated by Ni and Fe salt by wet impregnation method. Then, impregnated catalysts were dried in an oven at 80 °C for 12 h. After that, dried catalysts were calcined under air atmosphere with different calcination temperature for 3 h. Then, catalysts were reduced at reduction temperature 500 °C for 1 h under hydrogen atmosphere. Reduced catalysts were used to perform the CO_2 methanation reaction under the molar ratio of CO_2:H_2:He of 1:4:5 at reaction temperature 325 °C for 20 min. GC was applied to obtain the peak area which was used to calculate CO_2 conversion and CH_4 yield. In addition, soap film meter was equipped to measure flowrate of product gas during the reaction.

At various calcination temperature, an increase in calcination temperature from 250 to 350 °C increased CO_2 conversion and CH_4 selectivity due to the complete change of metal nitrate to metal oxide. However, continuous increase in calcination temperature from 350 °C to 400 °C decreased CO_2 conversion and CH_4 selectivity due to an oxidizing of support material and an agglomeration of metal compound. Therefore, calcination temperature 350 °C was the optimal condition in this experiment. In addition, in this experiment, total metal loading was kept at 30 wt% while weight ratio of Ni to Fe was also varied to study the catalyst performance. The results revealed that the existence of Fe could enhance CO_2 conversion and CH_4 selectivity due to the increase in reducibility of catalyst. However, a high amount of Fe led to a decrease in catalyst performance due to the desorption of CO which was the intermediate in CO_2

methanation. The desorption of CO led to a decrease in CO_2 conversion and CH_4 selectivity.

In order to understand a relationship between the calcination temperature and weight ratio of Ni-Fe, various characterization techniques including XRD and H_2-TPR were used to characterize the properties of catalysts such as crystallite size of Ni and reducibility of catalyst. It was found that the crystallite size of Ni increased when the calcination increased especially when calcination temperature increased from 350 °C to 400 °C due to the decomposition of carbon support at high temperature. In addition, it was found that catalyst at calcination temperature of 350 °C provided the highest H_2 consumption which was observed from peak area of H_2-TPR result resulting in highest reducibility. The addition of Fe could reduce the crystallite size of Ni which would enhance the interaction force between metal and support resulting in a decrease in H_2 consumption causing the difficulty reduction of catalyst. Thus, the 30 wt% Ni/CNTs catalyst provided the highest catalyst performance when observed from the reducibility. In addition, EDX technique was applied to identify the actual weight ratio of Ni to Fe which was found that weight ratio of Ni to Fe at this condition was 70:30.

It could be concluded that 30 wt% $Ni_{70}Fe_{30}$/CNT provided higher catalyst performance due to its highest reducibility under controlled condition. In this experiment, highest CO_2 conversion of 30 wt% $Ni_{70}Fe_{30}$/CNT catalyst was obtained at 20 min and reaction temperature 325 °C. The gas mixture of CO_2: H_2: He had the molar ratio of 1:4:5. The total flow rate and reaction temperature was fixed at 77 mL/min.

5.2   Recommendation for future work

The amount of CNTs synthesized from co-pyrolysis of eucalyptus oil and ferrocene in this study was limited to only 1-2 g due to the safety concern in the process. Therefore, if CNT production could be scaled up safely, more synthesized CNTs would be obtained which would reduce the time for synthesis.

APPENDICES

APPENDIX A

Yield of synthesized CNTs

Yield of synthesized CNTs at various $m_{oil/fer}$ and T_{pyro} was calculated by **Eq.5**. Due to the various $m_{oil/fer}$, the volume of eucalyptus oil used in the synthesis of CNTs at various $m_{oil/fer}$ was calculated by **Eq. A1** and was shown in **Table A1.**

$$m_{oil/fer} = \frac{m_{oil,pure}}{m_{fer,pure}} = \frac{\dfrac{W_{oil,pure}}{MW_{oil,pure}}}{\dfrac{W_{fer,pure}}{MW_{fer,pure}}} = \frac{\dfrac{X_{oil} \times \rho_{oil} \times V_{oil}}{MW_{oil,pure}}}{\dfrac{X_{fer} \times W_{fer}}{MW_{fer,pure}}}$$

In this experiment, it was assumed that purity by weight of eucalyptus oil (X_{oil}) and ferrocene (X_{fer}) equal to 1. Thus, the equation could be defined as followed.

$$m_{oil/fer} = \frac{\dfrac{\rho_{oil} \times V_{oil}}{MW_{oil}}}{\dfrac{W_{fer}}{MW_{fer}}}$$

Then, rearrange the equation to obtain volume of eucalyptus oil

$$V_{oil} = \frac{m_{oil/fer} \times W_{fer} \times MW_{oil}}{\rho_{oil} \times MW_{fer}} \qquad \textbf{Equation A1}$$

Where

V_{oil}	= Volume of eucalyptus oil used in CNT synthesis (mL)
X_{fer}	= purity of ferrocene by weight = 1
X_{oil}	= purity of eucalyptus oil by weight = 1
W_{fer}	= weight of ferrocene (fixed at 1 g)
W_{oil}	= weight of eucalyptus oil
$MW_{fer,pure}$	= molecular weight of pure ferrocene (186.03 g/mol)

$MW_{oil,pure}$ = molecular weight of pure eucalyptol (154.25 g/mol)

$m_{oil/fer}$ = mole of pure eucalyptus oil to pure ferrocene

m_{oil} = mole of pure eucalyptus oil

m_{fer} = molar ratio of pure ferrocene

ρ_{oil} = density of eucalyptus oil (0.922 g/mL)

In **Table A1**, weight of eucalyptus oil (W_{oil}) came from the multiplication of volume and density of eucalyptus oil. In addition, to calculate the feeding time of eucalyptus oil, volume of eucalyptus oil used in CNT synthesis was divided by flow rate of eucalyptus oil which was constant at 10 mL/h. The results indicated that eucalyptus oil was fed into reactor for 5.29, 10.58, and 15.86 min, when the $m_{oil/fer}$ was varied from 1:1 to 2:1 and 3:1, respectively.

Table A1 Volume of eucalyptus oil used in the synthesis of CNTs at various $m_{oil/fer}$

$m_{oil/fer}$	V_{oil} (mL)	W_{oil} (g)	Feeding time (min)
1:1	0.88	0.81	5.3
2:1	1.76	1.63	10.6
3:1	2.64	2.44	15.9

The weight of eucalyptus oil, weight of ferrocene, and weight of product was shown in **Table A2**. Then, yields of synthesized CNTs were shown in **Table A3-A5.**

During CNT synthesis, flowrates of outlet gas were measured by soap-film meter which were shown in **Table A6-A7**. A soap-film meter had an inner diameter of 0.019 m and the time that soap-film moved for 0.1 m (Lapse time) was measured.

Thus, the volume (V) which gas moved

$$V = \pi R^2 h = \pi \left(\frac{0.019}{2}\right)^2 (0.1) = 2.83 \times 10^{-5} \, m^3$$

Then, flowrate of outlet gases (F) was calculated by dividing the volume with lapse time. For examples, at $m_{oil/fer}$ of 1:1 and T_{pyro} of 900 ℃, lapse time was equal to 9.96 s

$$F = \frac{V(m^3)}{Lapse\ time(s)} = \frac{2.83 \times 10^{-5}}{9.96} = 2.85 \times 10^{-6} \, \frac{m^3}{s}$$

Converting to cm³/min unit,

$$F = 2.85 \times 10^{-6} \frac{m^3}{s} \times 10^6 \frac{cm^3}{m^3} \times 60 \frac{s}{min} = 170.8 \frac{cm^3}{min}$$

จุฬาลงกรณ์มหาวิทยาลัย
CHULALONGKORN UNIVERSITY

Table A2 Weight of eucalyptus oil, ferrocene, and product at various $m_{oil/fer}$ and T_{pyro}

T_{pyro} (°C)	$m_{oil/fer}$	Weight of eucalyptus oil (g)	Weight of ferrocene (g)	Weight of product (g)
800	1:1	0.81	1.0021	0.8091
			1.0057	0.5973
			1.0043	0.7448
	2:1	1.63	1.0154	0.9799
			1.0082	0.7956
			1.0024	0.6636
	3:1	2.44	1.0173	1.1276
			1.0094	0.7281
			1.0046	0.8082
850	1:1	0.81	1.0083	0.6907
			1.0053	0.7601
			1.0094	0.9914
	2:1	1.63	1.0071	0.9398
			1.0060	1.0951
			1.0039	1.0146
	3:1	2.44	1.0053	1.3092
			1.0066	1.1497
			1.0060	1.2541
900	1:1	0.81	1.0029	0.7196
			1.0045	0.8549
			1.0079	0.5938
	2:1	1.63	1.0068	1.0541
			1.0055	0.8884
			1.0093	0.9496
	3:1	2.44	1.0085	1.3119
			1.0024	1.0379
			1.0033	1.1637

MW of pure ferrocene   =   186.03 g/mol

MW of pure eucalyptus oil   =   154.25 g/mol

Table A3 Product yield (%) of synthesized CNTs at T_{pyro} 800 ℃ and various $m_{oil/fer}$

Repeatability	$m_{oil/fer}$ at T_{pyro} 800 ℃		
	1:1	2:1	3:1
Run 1	46.73	39.30	34.75
Run 2	34.43	32.00	22.49
Run 3	42.97	26.75	25.01
Average yield	41.38	32.68	27.42
Standard Deviation	6.30	6.30	6.48

Table A4 Product yield (%) of synthesized CNTs at T_{pyro} 850 ℃ and various $m_{oil/fer}$

Repeatability	$m_{oil/fer}$ at T_{pyro} 850 ℃		
	1:1	2:1	3:1
Run 1	39.76	37.81	40.50
Run 2	43.83	44.08	35.55
Run 3	57.03	40.87	38.78
Average yield	46.87	40.92	38.28
Standard Deviation	9.03	3.13	2.51

Table A5 Product yield (%) of synthesized CNTs at T_{pyro} 900 ℃ and various $m_{oil/fer}$

Repeatability	$m_{oil/fer}$ at T_{pyro} 900 ℃		
	1:1	2:1	3:1
Run 1	41.55	42.42	40.54
Run 2	49.31	35.77	32.13
Run 3	34.19	38.17	35.99
Average yield	41.68	38.79	36.22
Standard Deviation	7.56	3.37	4.21

Table A6 Flowrate of outlet gases in CNT synthesis at various $m_{oil/fer}$ and T_{pyro} 900 ℃

Pyrolysis time (min)	$m_{oil/fer}$ 1:1		$m_{oil/fer}$ 2:1		$m_{oil/fer}$ 3:1	
	Lapse times (s)	Flowrate (cm^3/min)	Lapse times (s)	Flowrate (cm^3/min)	Lapse times (s)	Flowrate (cm^3/min)
1	Clock time < 2 s					
2	9.96	170.8	9.21	184.7	8.89	191.4
3	10.85	156.8	10.15	167.6	8.84	192.4
4	10.80	157.5	10.89	156.2	8.42	202.0
5	7.86	216.4	8.04	211.6	7.73	220.1
6	7.32	232.4	6.48	262.5	6.27	271.3
7	7.26	234.3	5.24	324.7	5.91	287.8
8	7.33	232.1	4.52	376.4	5.07	335.5
9	7.42	229.3	4.31	394.7	4.42	384.9
10	7.51	226.5	4.12	412.9	3.81	446.5
11	7.63	223.0	4.10	414.9	3.27	520.2
12	7.68	221.5	4.59	370.6	3.01	565.2
13	7.86	216.4	5.29	321.6	2.89	588.6
14	8.45	201.3	6.05	281.2	2.82	603.3
15	8.70	195.5	6.68	254.7	2.93	580.6
16	9.23	184.3	7.26	234.3	3.23	526.7
17	9.57	177.8	8.40	202.5	3.45	493.1
18	9.86	172.5	8.62	197.4	3.60	472.5
19	10.21	166.6	9.45	180.0	3.86	440.7
20	10.64	159.9	9.86	172.5	4.23	402.2
21	11.11	153.1	10.43	163.1	5.03	338.2
22	11.26	151.1	10.69	159.1	5.85	290.8
23	11.46	148.4	10.66	159.6	6.03	282.1
24	11.83	143.8	10.72	158.7	7.25	234.6
25	11.92	142.7	11.01	154.5	7.56	225.0
26	11.90	143.0	11.10	153.3	7.82	217.5
27	11.93	142.6	11.21	151.8	8.22	207.0
28	11.94	142.5	11.26	151.1	9.20	184.9
29	11.68	145.6	11.14	152.7	10.41	163.4
30	11.96	142.2	11.45	148.6	10.32	164.8

Table A7 Flowrate of outlet gases in CNT synthesis at various T_{pyro} and $m_{oil/fer}$ 3:1

Pyrolysis time (min)	T_{pyro} 800 ℃		T_{pyro} 850 ℃		T_{pyro} 900 ℃	
	Lapse times (s)	Flowrate (cm^3/min)	Lapse times (s)	Flowrate (cm^3/min)	Lapse times (s)	Flowrate (cm^3/min)
1	Clock time < 2 s					
2	2.70	161.9	3.21	192.9	3.19	191.4
3	2.80	167.9	3.01	180.6	3.21	192.4
4	2.94	176.3	2.91	174.8	3.37	202.0
5	3.32	199.4	2.88	173.1	3.67	220.1
6	3.87	232.4	3.65	219.2	4.52	271.3
7	4.10	245.8	4.10	246.2	4.80	287.8
8	4.67	280.3	4.70	282.1	5.59	335.5
9	5.44	326.5	5.48	329.0	6.41	384.9
10	5.85	350.8	6.30	378.0	7.44	446.5
11	6.02	361.2	6.78	407.0	8.67	520.2
12	6.19	371.4	7.29	437.3	9.42	565.2
13	6.30	378.0	8.03	481.9	9.81	588.6
14	5.53	331.6	7.68	461.0	10.05	603.3
15	5.18	311.0	7.21	432.9	9.68	580.6
16	4.72	283.1	6.88	412.9	8.78	526.7
17	3.97	237.9	6.08	365.1	8.22	493.1
18	3.45	207.0	5.46	327.8	7.88	472.5
19	3.22	193.1	4.98	299.0	7.35	440.7
20	3.09	185.3	4.71	282.6	6.70	402.2
21	2.98	178.7	4.38	262.5	5.64	338.2
22	2.90	174.1	3.88	232.7	4.85	290.8
23	2.83	169.8	3.38	202.5	4.70	282.1
24	2.75	165.0	3.06	183.3	3.91	234.6
25	2.74	164.5	2.98	178.5	3.75	225.0
26	2.68	161.1	2.95	176.8	3.63	217.5
27	2.66	159.7	2.92	175.0	3.45	207.0
28	2.63	158.0	2.87	172.0	3.08	184.9
29	2.58	154.5	2.80	168.1	2.72	163.4
30	2.57	154.4	2.72	162.9	2.75	164.8

Surface area of Fe catalysts

An increase in size of Fe particles resulting in a decrease of surface area was shown as followed.

Fe cluster

V_r

Fe cluster

V_r

Fe cluster

V_R
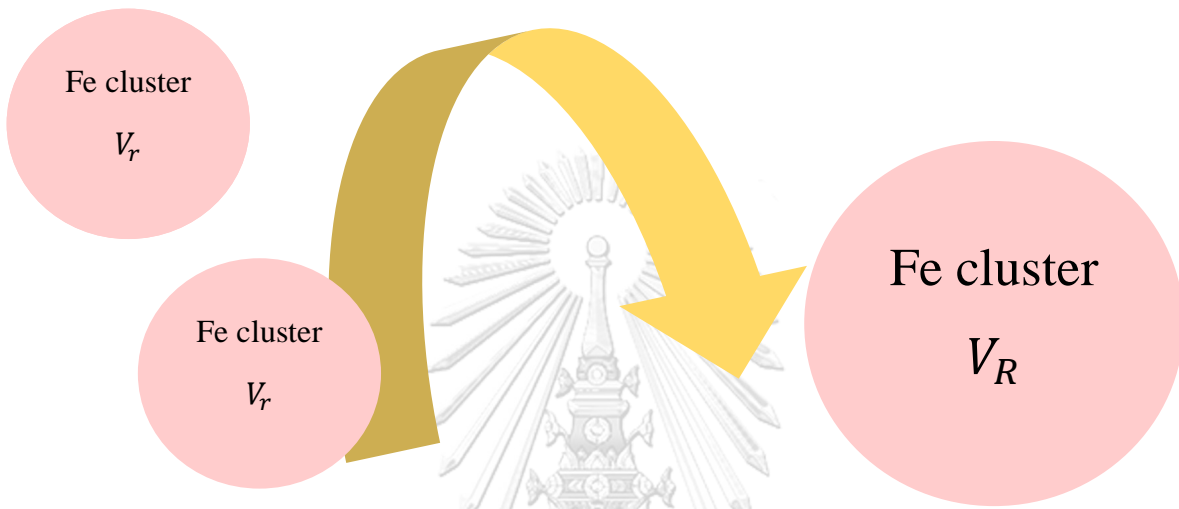
Declaration all parameters

V_R = Volume of big Fe cluster (m^3)

V_r = Volume of small Fe cluster (m^3)

R   = Radius of big Fe cluster (m)

r   = Radius of small Fe cluster (m)

S_R = Surface area of big Fe cluster (m^2)

S_r = Surface area of small Fe cluster (m^2)

S_{rn} = Surface area of small Fe cluster (m^2) of n units combined

Assumption

1. $V_R = nV_r$; n = number of small Fe clusters
2. $r_1 = r_2 = r_3 = r_n$; small clusters have same radius
3. Fe cluster has a spherical shape

Solution

Big Fe cluster

Volume of big Fe cluster 1 unit $V_R = \frac{4}{3}\pi R^3$ so, $R = \sqrt[3]{\dfrac{3}{4}\dfrac{V_R}{\pi}}$ m

Surface area of big Fe cluster 1 unit $S_R = 4\pi R^2 = 4\pi(\sqrt[3]{\dfrac{3}{4}\dfrac{V_R}{\pi}})^2$ m^2

Small Fe clusters

Volume of small Fe cluster 1 unit $V_r = \frac{4}{3}\pi r^3$ so, $r = \sqrt[3]{\dfrac{3}{4}\dfrac{V_r}{\pi}}$ m

Surface area of small Fe cluster 1 unit $S_r = 4\pi r^2 = 4\pi(\sqrt[3]{\dfrac{3}{4}\dfrac{V_r}{\pi}})^2$ m^2

So, $S_{rn} = nS_r$

$$S_{rn} = n(4\pi r^2) = n4\pi(\sqrt[3]{\dfrac{3}{4}\dfrac{V_r}{\pi}})^2$$

Ratio of S_{rn}/S_R

$$\frac{S_{rn}}{S_R} = \frac{n4\pi(\sqrt[3]{\dfrac{3V_r}{4\,\pi}})^2}{4\pi(\sqrt[3]{\dfrac{3V_R}{4\,\pi}})^2} = \frac{n(V_r)^{2/3}}{(V_R)^{2/3}} = \frac{n(\frac{V_R}{n})^{2/3}}{(V_R)^{2/3}} = n^{1/3} \geq 1 \qquad ; n \geq 1$$

Thus, it can be concluded that surface area of small Fe clusters with n units combined (S_{rn}) is higher than surface area of big Fe cluster (S_R) if $n \geq 2$.

APPENDIX C

Curve fitting of Raman spectra
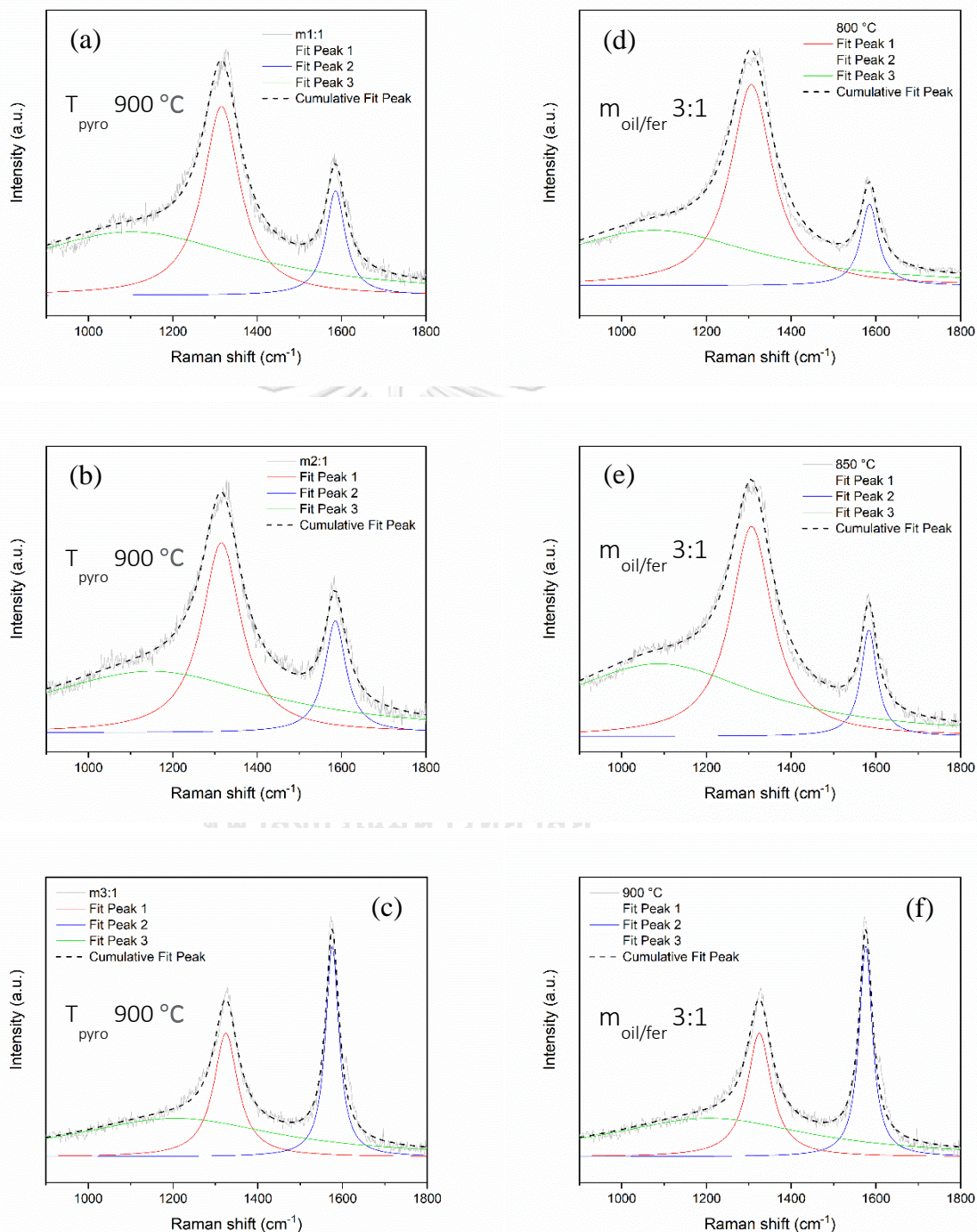
Fig. C1 Raman spectram of synthesized CNTs at various $m_{oil/fer}$ (a) 1:1 (b) 2:1 and (c) 3:1 and various T_{pyro} (d) 800 °C (e) 850 °C (f) 900 °C

APPENDIX D

An impregnation of Ni-Fe bimetallic on CNTs

Thirty weight percentage of metal loading with various weight ratio of Ni to Fe could be calculated based on weight of CNTs (CNTs 100 g with total metal 30 g). $Ni(NO_3)_2 \cdot 6H_2O$ and $Fe(NO_3)_3 \cdot 9H_2O$ were used as metal precursors, while solvent would be ethanol. The calculation of metal nitrate requirement was shown in **Eq.D1**.

$$\text{Metal nitrate required} = \frac{g\ CNT \times \%loading \times \%metal \times MW_{metal\ salt}}{MW_{metal\ atom}} \qquad \text{Equation D1}$$

Where

$g\ CNT$ = weight of CNT using as support material (0.2 g)

$\%loading$ = weight percentage of total metal loading on CNT (30 wt%)

$\%metal$ = weight percentage of Ni or Fe in total metal loading (0 to 100%)

$MW_{metal\ salt}$ = molecular weight of $Ni(NO_3)_2 \cdot 6H_2O$ or $Fe(NO_3)_3 \cdot 9H_2O$

                   (290.79 g/mol and 403.10 g/mol, respectively)

$MW_{metal\ atom}$ = molecular weight of Ni or Fe

                   (58.7 g/mol and 55.8 g/mol, respectively)

Example calculation of Ni(NO₃)₂·6H₂O required in 30 wt% Ni₇₅Fe₂₅/CNTs

catalyst (CNTs 0.2 g, $\%loading = 30\%, \%Ni = 75\%, \%Fe = 25\%,$)

- Ni(NO₃)₂·6H₂O required was calculated from **Eq. D1**

  Ni(NO₃)₂·6H₂O required = $\dfrac{0.2 \times 0.3 \times 0.75 \times 290.79}{58.7} = 0.2229$ g

- Fe(NO₃)₃·9H₂O required was calculated from **Eq. D1**

  Fe(NO₃)₃·9H₂O required = $\dfrac{0.2 \times 0.3 \times 0.25 \times 403.10}{55.8} = 0.1084$ g

Table D1 Weight of Ni(NO₃)₂·6H₂O and Fe(NO₃)₃·9H₂O requirement for each

various Ni to Fe weight ratio

Ni:Fe wt. ratio	%Ni	%Fe	Ni(NO₃)₂·6H₂O (g)	Fe(NO₃)₃·9H₂O (g)
1:0	100	0	0.2972	
3:1	75	25	0.2229	0.1084
1:1	50	50	0.1486	0.2167
1:3	25	75	0.0743	0.3251
0:1	0	100		0.4334

APPENDIX E

Actual Ni to Fe weight ratio on synthesized CNTs

Table E1 Actual weight (g) of metal nitrate used in impregnation method

Ni:Fe wt. ratio	$Ni(NO_3)_2.6H_2O$	Ni	$(FeNO_3)_3.9H_2O$	Fe
1:0	0.305	0.062	0	0.000
3:1	0.228	0.046	0.116	0.016
1:1	0.148	0.030	0.226	0.031
1:3	0.079	0.016	0.329	0.046
0:1	0	0.000	0.438	0.061

Table E2 Average percentage of Ni-Fe which was analyzed from EDX of Ni-Fe/CNT catalyst compared with average calculated percentage of Ni-Fe for impregnation

Ni:Fe wt. ratio	Impregnation method			EDX		
	Ni(g)	Fe(g)	Ni:Fe wt. ratio	Ni (wt%)	Fe (wt%)	Ni:Fe wt. ratio
1:0	0.062	0.000	100:0	33	14	70:30
3:1	0.046	0.016	74:26	23	18	55:45
1:1	0.030	0.031	49:51	12	23	33:67
1:3	0.016	0.046	26:74	6	24	20:80
1:1	0.000	0.061	0:100	0	23	0:100

APPENDIX F
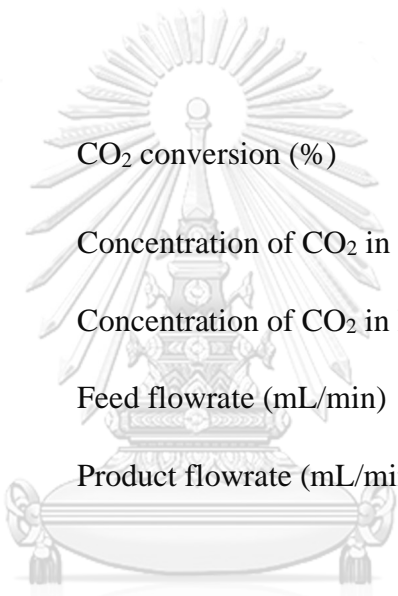
Calculation of CO₂ conversion and CH₄ selectivity

CO₂ conversion

CO₂ conversion could be calculated from **Eq.3** in section 3.4.

$$X_{CO2}(\%) = \frac{[CO_2]_{in} \times F_{in} - [CO_2]_{out} \times F_{out}}{[CO_2]_{in} \times F_{in}} \times 100 \qquad \text{Equation 3}$$

Where

X_{CO2}	=	CO₂ conversion (%)
$[CO_2]_{in}$	=	Concentration of CO₂ in Feed (mol/mL)
$[CO_2]_{out}$	=	Concentration of CO₂ in Product (mol/mL)
F_{in}	=	Feed flowrate (mL/min)
F_{out}	=	Product flowrate (mL/min)

<u>Example</u> 30 wt% Ni/CNT catalyst

- Feed flowrate (F_{in}) could be measured from gas flowmeter before reaction. (76.9 mL/min)
- Product flowrate (F_{out}) could be calculated from **Eq. F1** as shown in **Table F1**. Average time was measured from soap-film meter at the end of reaction time of 20 min in which the volume of soap-film meter was 8.32 mL.

$$Product\ flowrate\ \left(\frac{mL}{min}\right) = \frac{8.32\ mL}{Average\ time\ (s)} \times \left(\frac{60\ s}{1\ min}\right) \qquad \text{Equation F1}$$

Table F1 Product flowrate (F_{out}) using 30 wt% Ni/CNT catalyst

Time (s) / 8.32 mL			Average time (s)	F_{out} (mL/min)
8.06	8.10	8.05	8.07	61.9

- Concentration of CO_2 in feed was calculated from peak area of GC-MS before reaction and slope from calibration curve. The sample volume was 0.25 mL.

$$[CO_2]_{in} = \frac{\frac{Average\ peak\ area\ of\ CO2\ in}{sample\ volume}}{Slope\ of\ calibration\ curve\ (mol^{-1})} \quad \text{Equation F2}$$

Slope of the calibration curves were obtained from the plot of peak area of gases (CO_2, CH_4, CO) and mol of CO_2, CH_4, CO as shown in **Table F2**. Calibration curves were shown in **Figure G1-G3**.

Table F2 slope of calibration curves

Gases	mol^{-1}
CO_2	6.54×10^{10}
CH_4	4.86×10^{10}
CO	8.87×10^{10}

So, for 30 wt% Ni/CNT catalyst,

$$[CO_2]_{in} = \frac{\frac{87836 + 86901}{2} \times \frac{1}{0.25}}{6.54 \times 10^{10}} = 5.34 \times 10^{-6} \text{ mol/mL}$$

- Concentration of CO_2 in product was calculated from peak area of GC-MS during reaction and slope from calibration curve. The sample volume was 0.25 mL. Average peak area was obtained at the end of reaction time of 20 min where the reaction was in steady state.

$$[CO_2]_{out} = \frac{\frac{Average\ peak\ area\ of\ CO2\ out}{sample\ volume}}{Slope\ of\ calibration\ curve\ (mol^{-1})} \qquad \text{Equation F3}$$

So, for 30 wt% Ni/CNT catalyst,

$$[CO_2]_{out} = \frac{\frac{67196 + 67136}{2} \times \frac{1}{0.25}}{6.54 \times 10^{10}} = 4.11 \times 10^{-6}\ \text{mol/mL}$$

Thus, CO_2 conversion of 30 wt% Ni/CNT catalyst

$$X_{CO2}(\%) = \frac{5.34 \times 10^{-6} \times 76.9 - 4.11 \times 10^{-6} \times 61.9}{5.34 \times 10^{-6} \times 76.9} \times 100 = 38\%$$

CH₄ selectivity

CH₄ selectivity could be calculated from Eq.4 in section 3.4.

$$S_{CH4}(\%) = \frac{[CH_4]_{out}}{[CO]_{out} + [CH_4]_{out}} \times 100 \qquad \text{Equation 4}$$

$[CH_4]_{out}$ =   Concentration of CH₄ in Product (mol/mL)

$[CO]_{out}$ =   Concentration of CO in Product (mol/mL)

Concentration of CH₄ and CO in product were calculated from peak area of GC-MS before reaction and slope of calibration curve shown in **Table F2**. The sample volume was 0.25 mL. Equations were shown in **Eq. F4** and **Eq. F5**.

$$[CH_4]_{out} = \frac{\frac{Average\ peak\ area\ of\ CH4\ out}{sample\ volume}}{Slope\ of\ calibration\ curve\ (mol^{-1})} \qquad \text{Equation F4}$$

$$[CO]_{out} = \frac{\frac{Average\ peak\ area\ of\ CO\ out}{sample\ volume}}{Slope\ of\ calibration\ curve\ (mol^{-1})} \qquad \text{Equation F5}$$

So, for 30 wt% Ni/CNT catalyst,

$$[CH_4]_{out} = \frac{\frac{25541 + 24927}{2} \times \frac{1}{0.25}}{4.86 \times 10^{10}} = 2.08 \times 10^{-6} \ \text{mol/mL}$$

$$[CO]_{out} = \frac{\frac{4130 + 4102}{2} \times \frac{1}{0.25}}{8.87 \times 10^{10}} = 1.86 \times 10^{-7} \ \text{mol/mL}$$

Thus,

$$S_{CH4}(\%) = \frac{2.08 \times 10^{-6}(61.9)}{1.86 \times 10^{-7}(61.9) + 2.08 \times 10^{-6}(61.9)} \times 100 = 95 \ \%$$

Table F3 F_{in} and F_{out} of all catalysts

Catalysts	F_{in} (mL/min)	Time (s) / 8.32 mL			Average time (s)	F_{out} (mL/min)
30%Ni/CNT	76.9	8.06	8.10	8.05	8.07	61.9
30%Ni$_{75}$Fe$_{25}$/CNT	76.9	6.97	7.07	6.93	6.99	71.4
30%Ni$_{50}$Fe$_{50}$/CNT	76.4	6.32	6.36	6.30	6.33	78.9
30%Ni$_{25}$Fe$_{75}$/CNT	76.4	6.18	6.17	6.14	6.16	80.9
30%Fe/CNT	77.1	6.43	6.47	6.36	6.42	77.8
30%Ni/CNT-T250	77.5	6.89	7.06	7.08	7.01	71.2
30%Ni/CNT-T300	77.5	7.501	7.400	7.553	7.48	66.7
30%Ni/CNT-T350	76.9	8.06	8.10	8.05	8.05	61.9
30%Ni/CNT-T400	77.1	7.233	7.195	7.155	7.19	69.4

Table F4 Peak area of $CO_{2,in}$ and $CO_{2,out}$ for all catalysts

Catalysts	$CO_{2,in}$		$CO_{2,out}$	
30%Ni/CNT	87836	86901	67196	67136
30%Ni$_{75}$Fe$_{25}$/CNT	87604	87033	71192	71189
30%Ni$_{50}$Fe$_{50}$/CNT	87701	87016	81372	76890
30%Ni$_{25}$Fe$_{75}$/CNT	87591	87146	80534	77627
30%Fe/CNT	86702	88078	83154	83126
30%Ni/CNT-T250	83738	88466	73072	75270
30%Ni/CNT-T300	83628	88127	65981	65981
30%Ni/CNT-T350	87836	86901	67196	67136
30%Ni/CNT-T400	85825	87684	80071	83516

Table F5 Peak area of $CH_{4,out}$ and CO_{out} for all catalysts

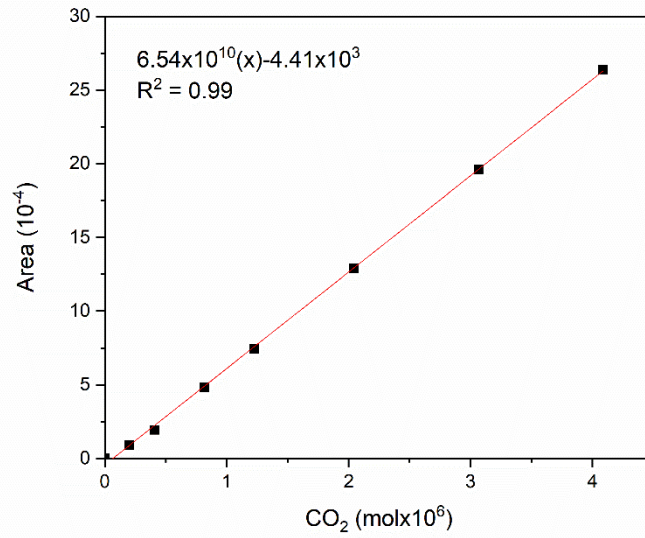| Catalysts	$CH_{4,out}$		CO_{out}	
30%Ni/CNT	25541	24927	4130	4102
30%Ni$_{75}$Fe$_{25}$/CNT	15440	15596	4503	4595
30%Ni$_{50}$Fe$_{50}$/CNT	595	488	5764	7483
30%Ni$_{25}$Fe$_{75}$/CNT	464	267	6602	4207
30%Fe/CNT	0	0	6043	6021
30%Ni/CNT-T250	10177	9832	6453	6705
30%Ni/CNT-T300	20413	20413	4974	4974
30%Ni/CNT-T350	25541	24927	4130	4102
30%Ni/CNT-T400	6238	5849	3769	3927

APPENDIX G

Calibration curves

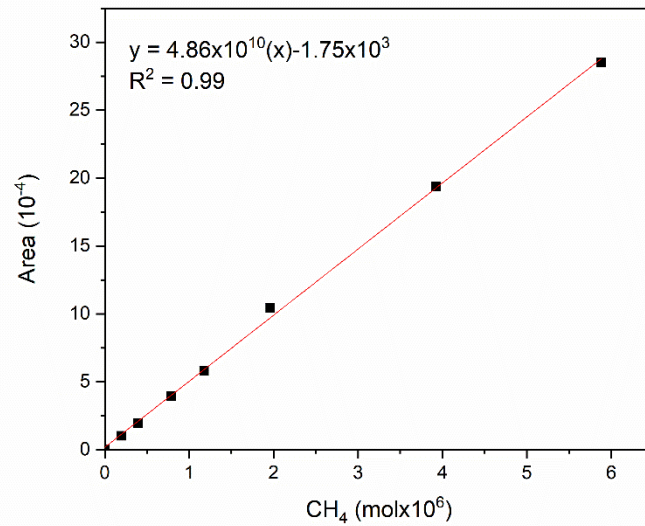

Figure F1 calibration curve of CO_2

Figure F2 calibration curve of CH_4
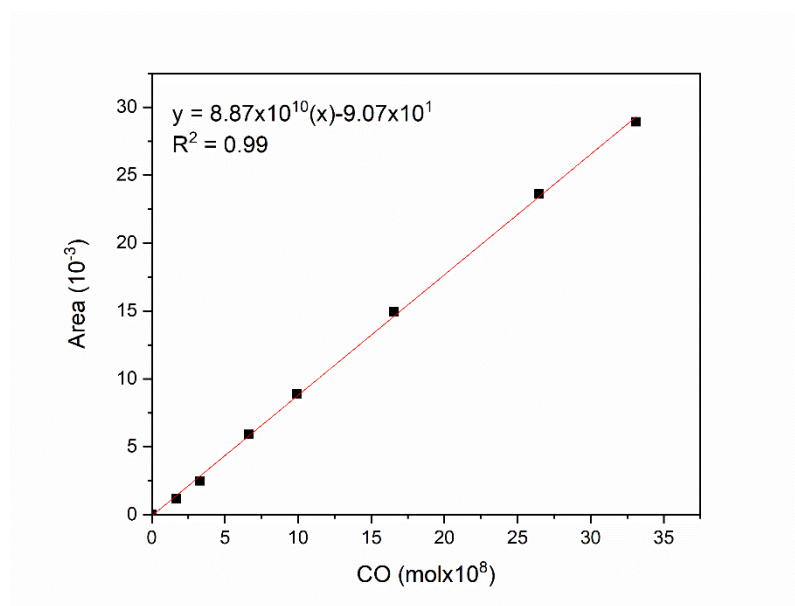
Figure F3 calibration curve of CO

REFERENCES

1.   Wuebbles, D., Jain, A. Concerns About Climate Change and the Role of Fossil Fuel Use. Fuel Processing Technology. 2001;71:99-119.

2.   Sreedhar, I., Y, V., Singh, S., Venugopal, A., Reddy, B. Developmental Trends in CO_2 Methanation using various catalysts. Catalysis Science & Technology. 2019.

3.   Rönsch, S., Schneider, J., Matthischke, S., Schlüter, M., Götz, M., Lefebvre, J., Prabhakaran, P., Bajohr, S. Review on methanation – From fundamentals to current projects. Fuel. 2016;166:276-96.

4.   Fukuhara, C., Hayakawa, K., Suzuki, Y., Kawasaki, W., Watanabe, R. A novel nickel-based structured catalyst for CO_2 methanation: A honeycomb-type Ni/CeO_2 catalyst to transform greenhouse gas into useful resources. Applied Catalysis A: General. 2017;532:12-8.

5.   Wang, Y., Xu, Y., Liu, Q., Sun, J., Ji, S., Wang, Z.-j. Enhanced low-temperature activity for CO_2methanation over NiMgAl/SiC composite catalysts. Journal of Chemical Technology & Biotechnology. 2019;94.

6.   Aziz, M.A.A., Jalil, A.A., Triwahyono, S., Ahmad, A. CO_2 methanation over heterogeneous catalysts: recent progress and future prospects. Green Chemistry. 2015;17(5):2647-63.

7.   Delmelle, R., Duarte, R.B., Franken, T., Burnat, D., Holzer, L., Borgschulte, A., Heel, A. Development of improved nickel catalysts for sorption enhanced CO_2 methanation. International Journal of Hydrogen Energy. 2016;41(44):20185-91.

8.   Mills, G.A., Steffgen, F.W. Catalytic Methanation. Catalysis Reviews. 1974;8(1):159-210.

9.   Meshkini-Far, R., Dyachenko, A., Gaidai, S., Bieda, O., Filonenko, M., Ischenko, O. Catalytic Properties of Ni-Fe Systems in the Reaction of CO_2 Methanation at Atmospheric Pressure. Acta Physica Polonica A. 2018;133(4):1088-90.

10.   Ong, Y.T., Ahmad, A.L., Zein, S.H.S., Tan, S.H. A review on carbon nanotubes in an environmental protection and green engineering perspective. Brazilian Journal of Chemical Engineering. 2010;27:227-42.

11.   Salomé, O., Soares, G., Frías, R., editors. Development of carbon materials as metal catalyst supports and metal-free catalysts for catalytic reduction of ions and advanced oxidation processes2016.

12.   Hou, B., Xiang, R., Inoue, T., Einarsson, E., Chiashi, S., Shiomi, J., Miyoshi, A., Maruyama, S. Decomposition of Ethanol and Dimethyl Ether during Chemical Vapor Deposition Synthesis of Single-Walled Carbon Nanotubes. Japanese Journal of Applied Physics. 2011;50(6).

13.   Kumar, R., Singh, R.K., Singh, D.P. Natural and waste hydrocarbon precursors for the synthesis of carbon based nanomaterials: Graphene and CNTs. Renewable and Sustainable Energy Reviews. 2016;58:976-1006.

14.   Ghosh, P., Afre, R.A., Soga, T., Jimbo, T. A simple method of producing single-walled carbon nanotubes from a natural precursor: Eucalyptus oil. Materials Letters. 2007;61(17):3768-70.

15.   Shah, K.A., Tali, B.A. Synthesis of carbon nanotubes by catalytic chemical vapour deposition: A review on carbon sources, catalysts and substrates. Materials Science in Semiconductor Processing. 2016;41:67-82.

16.   Götz, M., Lefebvre, J., Mörs, F., McDaniel Koch, A., Graf, F., Bajohr, S., Reimert, R., Kolb, T. Renewable Power-to-Gas: A technological and economic review. Renewable Energy. 2016;85:1371-90.

17.   Fitzharris, W.D., Katzer, J.R., Manogue, W.H. Sulfur deactivation of nickel methanation catalysts. Journal of Catalysis. 1982;76(2):369-84.

18.   Sang, J.C., Hae, J.K., Kim, S.J., Park, S.B., Dong, H.P., Huh, D. Adsorbed Carbon Formation and Carbon Hydrogenation for CO_2 Methanation on the Ni(111) Surface: ASED-MO Study. Bulletin of the Korean Chemical Society. 2005;26:1682-8.

19.   Medsforth, S. CLXIX.—Promotion of catalytic reactions. Part I. Journal of the Chemical Society, Transactions. 1923;123(0):1452-69.

20.   Ren, J., Guo, H., Yang, J., Qin, Z., Lin, J., Li, Z. Insights into the mechanisms of CO2 methanation on Ni(111) surfaces by density functional theory. Applied Surface Science. 2015;351:504-16.

21.   Li, W., Nie, X., Jiang, X., Zhang, A., Ding, F., Liu, M., Liu, Z., Guo, X., Song, C. ZrO_2Support Imparts Superior Activity and Stability of Co Catalysts for CO_2 Methanation. Applied Catalysis B: Environmental. 2017;220.

22.   Chang, F.-W., Kuo, M.-S., Tsay, M.-T., Hsieh, M.-C. Hydrogenation of CO_2 over nickel catalysts on rice husk ash-alumina prepared by incipient wetness impregnation. Applied Catalysis A: General. 2003;247(2):309-20.

23.   Tada, S., Shimizu, T., Kameyama, H., Haneda, T., Kikuchi, R. Ni/CeO_2 catalysts with high CO_2 methanation activity and high CH_4 selectivity at low temperatures. International Journal of Hydrogen Energy. 2012;37(7):5527-31.

24.   Everson, R.C., Mulay, L.N., Mahajan, O.P., Walker Jr, P.L. Magnetic and catalytic properties of sintered nickel catalysts for the methanation reaction. Journal of Chemical Technology and Biotechnology. 1979;29(1):1-7.

25.   Sehested, J., Larsen, K.E., Kustov, A.L., Frey, A.M., Johannessen, T., Bligaard, T., Andersson, M.P., Nørskov, J.K., Christensen, C.H. Discovery of technical methanation catalysts based on computational screening. Topics in Catalysis. 2007;45(1):9-13.

26.   Garbarino, G., Riani, P., Magistri, L., Busca, G. A study of the methanation of carbon dioxide on Ni/Al_2O_3 catalysts at atmospheric pressure. International Journal of Hydrogen Energy. 2014;39:11557–65.

27.   Gac, W., Zawadzki, W., Słowik, G., Sienkiewicz, A., Kierys, A. Nickel catalysts supported on silica microspheres for CO_2 methanation. Microporous and Mesoporous Materials. 2018;272:79-91.

28.   Zhou, G., Liu, H., Cui, K., Xie, H., Jiao, Z., Zhang, G., Xiong, K., Zheng, X. Methanation of carbon dioxide over Ni/CeO_2 catalysts: Effects of support CeO_2 structure. International Journal of Hydrogen Energy. 2017;42(25):16108-17.

29.   Zhou, R., Rui, N., Fan, Z., Liu, C.-j. Effect of the structure of Ni/TiO_2 catalyst on CO_2 methanation. International Journal of Hydrogen Energy. 2016;41(47):22017-25.

30.   Feng, Y., Yang, W., Chu, W. Effect of Ca modification on the catalytic performance of Ni/AC for CO_2 methanation. Integrated Ferroelectrics. 2016;172(1):40-8.
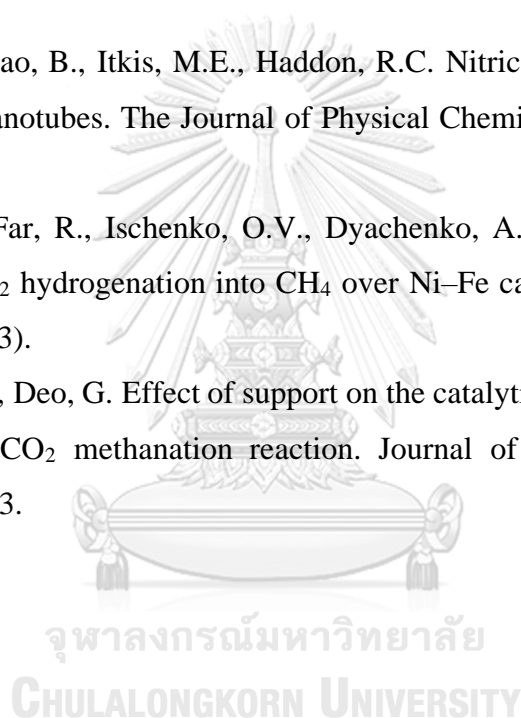
31.   Wang, W., Chu, W., Wang, N., Yang, W., Jiang, C. Mesoporous nickel catalyst supported on multi-walled carbon nanotubes for carbon dioxide methanation *. International Journal of Hydrogen Energy. 2015;41.

32.   Feng, Y., Yang, W., Chu, W. A Study of CO_2 Methanation over Ni-Based Catalysts Supported by CNTs with Various Textural Characteristics. International Journal of Chemical Engineering. 2015;2015:1-7.

33.   Holban, A.M., Grumezescu, A.M., Andronescu, E. Chapter 10 - Inorganic nanoarchitectonics designed for drug delivery and anti-infective surfaces. In: Grumezescu, A.M., editor. Surface Chemistry of Nanobiomaterials: William Andrew Publishing; 2016. p. 301-27.

34.   Camponeschi, E. Dispersion and alignment of carbon nanotube polymer based composites. 2007.

35.   Bethune, D.S., Kiang, C.H., de Vries, M.S., Gorman, G., Savoy, R., Vazquez, J., Beyers, R. Cobalt-catalysed growth of carbon nanotubes with single-atomic-layer walls. Nature. 1993;363(6430):605-7.

36.   Iijima, S., Ichihashi, T. Single-shell carbon nanotubes of 1-nm diameter. Nature. 1993;363(6430):603-5.

37.   Vidu, R., Rahman, M., Mahmoudi, M., Enachescu, M., Poteca, T., Opris, I. Nanostructures: A Platform for Brain Repair and Augmentation. Frontiers in systems neuroscience. 2014;8:91.

38.   Khare, R., Bose, S. Carbon Nanotube Based Composites A Review. Journal of Minerals and Materials Characterization and Engineering. 2005;04.

39.   Charinpanitkul, T., Tanthapanichakoon, W., Sano, N. Carbon nanostructures synthesized by arc discharge between carbon and iron electrodes in liquid nitrogen. Current Applied Physics. 2009;9(3):629-32.

40.   Arepalli, S. Laser Ablation Process for Single-Walled Carbon Nanotube Production. Journal of nanoscience and nanotechnology. 2004;4:317-25.

41.   Mongkolsamai, P. Treatment of wastewater contaminated with antibiotics using magnetic carbon nanoparticles [Thesis]: Chulalongkorn University; 2013.

42.   Mohan, M., Sharma, V.K., Kumar, E.A., Gayathri, V. Hydrogen storage in carbon materials—A review. Energy Storage. 2019;1(2).

43.   Persson, A.I., Larsson, M.W., Stenström, S., Ohlsson, B.J., Samuelson, L., Wallenberg, L.R. Solid-phase diffusion mechanism for GaAs nanowire growth. Nature Materials. 2004;3(10):677-81.

44.   Wagner, R.S., Ellis, W.C. VAPOR-LIQUID-SOLID MECHANISM OF SINGLE CRYSTAL GROWTH. Applied Physics Letters. 1964;4(5):89-90.

45.   Sugime, H., Sato, T., Nakagawa, R., Hayashi, T., Inoue, Y., Noda, S. Ultra-long carbon nanotube forest via in situ supplements of iron and aluminum vapor sources. Carbon. 2021;172:772-80.

46.   Thonganantakul, O., Chaiwat, W., Srinives, S., Suttiponparnit, K., Charinpanitul, T. Effect of Preloaded Ferrocene in Co-pyrolysis of Kerosene/Ferrocene on CNT Synthesis. Journal of the Japan Institute of Energy. 2018;97(7):180-5.

47.   NIOSH pocket guide to chemical hazards: [Cincinnati, Ohio] : U.S. Dept. of Health and Human Services, Public Health Service, Centers for Disease Control and Prevention, National Institute for Occupational Safety and Health ; Washington, DC : For sale by the U.S. G.P.O., Supt. of Docs., [1994]; 1994.

48.   Rabbani, F., Malaibari, Z., A, A., Jamie, A. Catalytic Synthesis of Substrate-Free, Aligned and Tailored High Aspect Ratio Multiwall Carbon Nanotubes in an Ultrasonic Atomization Head CVD Reactor. Journal of Nanomaterials. 2016;2016:1-10.

49.   Ming, H., Peiling, D., Yunlong, Z., Jing, G., Xiaoxue, R. Effect of Reaction Temperature on Carbon Yield and Morphology of CNTs on Copper Loaded Nickel Nanoparticles. Journal of Nanomaterials. 2016;2016:8106845.

50.   Li, W.Z., Wen, J., Ren, Z.F. Effect of temperature on growth and structure of carbon nanotubes by chemical vapor deposition. Applied Physics A: Materials Science & Processing. 2002;74:397-402.

51.   Lee, C.J., Park, J., Huh, Y., Yong Lee, J. Temperature effect on the growth of carbon nanotubes using thermal chemical vapor deposition. Chemical Physics Letters. 2001;343(1):33-8.

52.   Wierzbicki, D., Moreno, M.V., Ognier, S., Motak, M., Grzybek, T., Da Costa, P., Gálvez, M.E. Ni-Fe layered double hydroxide derived catalysts for non-plasma and DBD plasma-assisted CO_2 methanation. International Journal of Hydrogen Energy. 2020;45(17):10423-32.

53.   Thonganantakul, O., Srinives, S., Chaiwat, W., Kerdnawee, K., Suttiponparnit, K., Charinpanitkul, T. Temperature dependence of iron oxide-graphene oxide properties for synthesis of carbon nanotube/graphene hybrid material. Catalysis Today. 2020.

54.   Ratchahat, S., Sudoh, M., Suzuki, Y., Kawasaki, W., Watanabe, R., Fukuhara, C. Development of a powerful CO_2 methanation process using a structured Ni/CeO_2 catalyst. Journal of CO_2 Utilization. 2018;24:210-9.

55.   Wulan, P., Setiawati, N. The Effect of Mass Ratio of Ferrocene to Camphor as Carbon Source and Reaction Time on the Growth of Carbon Nanotubes. E3S Web of Conferences. 2018;67:03037.

56.   Charinpanitkul, T., Sano, N., Puengjinda, P., Klanwan, J., Akrapattangkul, N., Tanthapanichakoon, W. Naphthalene as an alternative carbon source for pyrolytic synthesis of carbon nanostructures. Journal of Analytical and Applied Pyrolysis. 2009;86(2):386-90.

57.   Tan, J., Arulselvan, P., Fakurazi, S., Ithnin, H., Hussein, M. A Review on Characterizations and Biocompatibility of Functionalized Carbon Nanotubes in Drug Delivery Design. Journal of Nanomaterials. 2014;2014:20.

58.   Shamsudin, M.S., Asli, N.A., Abdullah, S., Yahya, S.Y.S., Rusop, M. Effect of Synthesis Temperature on the Growth Iron-Filled Carbon Nanotubes as Evidenced by Structural, Micro-Raman, and Thermogravimetric Analyses. Advances in Condensed Matter Physics. 2012;2012:1-7.

59.   Costa, S., Borowiak-Palen, E., Kruszynska, M., Bachmatiuk, A., Kalenczuk, R. Characterization of carbon nanotubes by Raman spectroscopy. Materials Science- Poland. 2008;26.

60.   Banerjee, D., Bhowmick, P., Pahari, D., Santra, S., Sarkar, S., Das, B., Chattopadhyay, K.K. Pseudo first ordered adsorption of noxious textile dyes by low-temperature synthesized amorphous carbon nanotubes. Physica E: Low-dimensional Systems and Nanostructures. 2017;87:68-76.

61.   Zieliński, W., Kamedulski, P., Smolarkiewicz-Wyczachowski, A., Skorupska, M., Lukaszewicz, J., Ilnicka, A. Synthesis of Hybrid Carbon Materials Consisting of N-Doped Microporous Carbon and Amorphous Carbon Nanotubes. Materials. 2020;13:2997.

62.	Tenent, R., Gillaspie, D., Miedaner, A., Parilla, P., Curtis, C., Dillon, A. Fast-Switching Electrochromic Li-Doped NiO Films by Ultrasonic Spray Deposition. Journal of The Electrochemical Society. 2010;157.

63.	Resende, V., Peigney, A., De Grave, E., Laurent, C. In situ high-temperature Mössbauer spectroscopic study of carbon nanotube–Fe–Al$_2$O$_3$ nanocomposite powder. Thermochimica Acta - THERMOCHIM ACTA. 2009;494:86-93.

64.	Wang, R., Liu, S., Liu, S., Li, X., Zhang, Y., Xie, C., Zhou, S., Qiu, Y., Luo, S., Jing, F., Chu, W. Glycerol steam reforming for hydrogen production over bimetallic MNi/CNTs (M Co, Cu and Fe) catalysts. Catalysis Today. 2019.

65.	Hongxia, Q., Zhiqiang, W., Hua, Y., Lin, Z., Xiaoyan, Y. Preparation and Characterization of NiO Nanoparticles by Anodic Arc Plasma Method. Journal of Nanomaterials. 2009;479.

66.	Zainuri, M. Hematite from Natural Iron Stones as Microwave Absorbing Material on X-Band Frequency Ranges. IOP Conference Series: Materials Science and Engineering. 2017;196:012008.

67.	Huang, G., Wang, M., Hu, Y., Lv, S., Li, C. Synthesis, characterization, and debromination reactivity of cellulose-stabilized Pd/Fe nanoparticles for 2,2',4,4'-tretrabromodiphenyl ether. PLoS One. 2017;12(3):e0174589.

68.	Soleimani, H. Synthesis of Carbon Nanotubes for Oil-water Interfacial Tension Reduction. Oil & Gas Research. 2015;1.

69.	Chen, Y., Zhang, X.-F., Wang, A.-J., Zhang, Q., Huang, H., Feng, J.-J. Ultrafine Fe$_3$C nanoparticles embedded in N-doped graphitic carbon sheets for simultaneous determination of ascorbic acid, dopamine, uric acid and xanthine. Microchimica Acta. 2019;186.

70.	Meng, F., Zhong, P., Li, Z., Cui, X., Zheng, H. Surface Structure and Catalytic Performance of Ni-Fe Catalyst for Low-Temperature CO Hydrogenation. Journal of Chemistry. 2014;2014:1-7.

71.	Winter, L.R., Gomez, E., Yan, B., Yao, S., Chen, J.G. Tuning Ni-catalyzed CO$_2$ hydrogenation selectivity via Ni-ceria support interactions and Ni-Fe bimetallic formation. Applied Catalysis B: Environmental. 2018;224:442-50.

72.   Xiong, H., Moyo, M., Motchelaho, M.A.M., Jewell, L.L., Coville, N.J. Fischer–Tropsch synthesis over model iron catalysts supported on carbon spheres: The effect of iron precursor, support pretreatment, catalyst preparation method and promoters. Applied Catalysis A: General. 2010;388(1):168-78.

73.   Shi, D., Wojcieszak, R., Paul, S., Marceau, E. Ni Promotion by Fe: What Benefits for Catalytic Hydrogenation Catalysts. 2019;9(5).

74.   Unmuth, E.E., Schwartz, L.H., Butt, J.B. Iron alloy Fischer-Tropsch catalysts: I. Oxidation-reduction studies of the Fe-Ni system. Journal of Catalysis. 1980;61(1):242-55.

75.   Hu, H., Zhao, B., Itkis, M.E., Haddon, R.C. Nitric Acid Purification of Single-Walled Carbon Nanotubes. The Journal of Physical Chemistry B. 2003;107(50):13838-42.

76.   Meshkini Far, R., Ischenko, O.V., Dyachenko, A.G., Bieda, O., Gaidai, S.V., Lisnyak, V.V. CO_2 hydrogenation into CH_4 over Ni–Fe catalysts. Functional Materials Letters. 2018;11(03).

77.   Pandey, D., Deo, G. Effect of support on the catalytic activity of supported Ni-Fe catalysts for the CO_2 methanation reaction. Journal of Industrial and Engineering Chemistry. 2015;33.

จุฬาลงกรณ์มหาวิทยาลัย

CHULALONGKORN UNIVERSITY

VITA

NAME	Phanatchakorn Mala
DATE OF BIRTH	3 June 1996
PLACE OF BIRTH	Bangkok, Thailand
INSTITUTIONS ATTENDED	M.Eng. August 2019 – Present Major: Chemical Engineering Chulalongkorn University, Bangkok, Thailand B.Sc. (2nd-class honor) June 2015 – April 2019 Major: Chemical Technology Chulalongkorn University, Bangkok, Thailand
HOME ADDRESS	10/102 Moo.3, Sukhumvit Road, Samrong Nuea Sub-district, Mueang District, Samut Prakan 10270, Thailand
PUBLICATION	Phanatchakorn Mala, Chosel Lawagon, Sakhon Ratchahat, and Tawatchai Charinpanitkul, "Effect of temperature to electroless nickel plating on multiwalled carbon nanotubes" Proceeding of the 8th Joint Conference on Renewable Energy and Nanotechnology (JCREN 2019), Makassar, Indonesia, November 5-6, 2019. Phanatchakorn Mala, Sakhon Ratchahat, and Tawatchai Charinpanitkul, "Synthesis of Carbon Nanotubes via Co-pyrolysis of Eucalyptus Oil and Ferrocene" Proceeding of the 9th Joint Conference on Renewable Energy and Nanotechnology (JCREN 2020), Khon Kaen, Thailand, October 29, 2020.